Kristine Meling Underhaug

Evolution in Mechanical Behaviour in a Rolled 3xxx Aluminium Alloy during Lacquering

An experimental investigation and literature review on low temperature annealing and strain path changes

Master's thesis

NTNU
Norwegian University of
Science and Technology

Kristine Meling Underhaug

Evolution in Mechanical Behaviour in a Rolled 3xxx Aluminium Alloy during Lacquering

An experimental investigation and literature review on low temperature annealing and strain path changes

Master's thesis in Materials Science and Engineering
Supervisor: Bjørn Holmedal
June 2020

Norwegian University of Science and Technology
Faculty of Natural Sciences
Department of Materials Science and Engineering

NTNU
Norwegian University of
Science and Technology

Preface

This master's thesis has been carried out at the Department of Materials Science and Engineering at the Norwegian University of Science and Technology (NTNU), during the spring semester of 2020.

The present work is the continuation of the specialization project written by the same author, on the evolution in mechanical behaviour during lacquering. Due to the extraordinary circumstances concerning COVID-19 this semester, the obtained results from the project became of great importance in this thesis.

Trondheim, June 2020
Kristine Meling Underhaug

Abstract

The work in this master's thesis was conducted to investigate a possible hardening effect in 3xxx aluminium alloy sheets from a lacquering process. The objective was to investigate the change in mechanical behaviour and the influence of the exposure to elevated temperatures related to the drying of the lacquer and strain path changes. The evolution in mechanical behaviour was studied by conducting tensile testing of the material before and after lacquering while the investigation on possible mechanisms that may lead to changes in mechanical properties were carried out through a literature review. Conductivity measurements were conducted to estimate the amount of Mn in solid solution. The results from a characterization and heat experiments performed by the author prior to this thesis were used to determine the state of the material prior to lacquering and to determine the influence of short heat exposures.

The alloy investigated is a 3005 aluminium alloy with a chemical composition of 1.13 wt%Mn, 0.57 wt%Fe, 0.45 wt% Si, 0.17 wt% Cu, 0.31 wt% Mg and 0.10 wt% Zn. Prior treatment of the delivered material was casting and preheating to 570°C followed by hot and cold rolling down to a thickness of 0.3mm with a rolling reduction of 92%. The material was subsequently annealed at 224°C to H27, followed by lacquering. During the lacquering process, the lacquer is dried in two ovens, oven 1 has a temperature of 232°C and oven 2 has a temperature 253°C. The duration of the heat exposure in both ovens are at 19 seconds followed by quenching down to room temperature after each oven.

The results from the tensile testing confirmed that the lacquering process had altered the mechanical behaviour, however, the increase in strength was not possible to determine due to variations in measurements. The most persistent change was a reduction in uniform elongation after lacquering. From these results, there is no indication that the lacquering process can lead to recrystallization and the softening contribution from recovery activities are negligible. The possibility for concurrent precipitation of Mn bearing dispersoids and precipitation of Mg_2Si was determined as unlikely based on the microchemistry of the alloy, the time and temperature of the heat exposure and relevant observations from literature. Due to similarities with a reported hardening phenomenon at the onset of annealing of 3xxx alloy at low temperature, it is possible that the observed changes in mechanical behaviour is related to clusters of Mn and other alloying elements or precipitation of very small Si precipitates. However, it is difficult to determine the possibility for this to occur during lacquering, as the literature has not been able to conclude on the mechanism for the hardening phenomenon. The possibility for hardening from a strain path change is discussed with background in relevant observations from literature on the influence of dislocation structure and anisotropy, on the mechanical behaviour during a strain path change.

Sammendrag

Arbeidet i denne masteroppgaven ble utført for å undersøke en mulig herdene effekt i plater av en 3xxx aluminium legering etter en lakkeringsprosess. Hensikten var å undersøke endringen i mekanisk adferd og hvordan materialet blir påvirket av temperatureksponering relatert til tørking av lakken og tøyningsvei-endringer. Endringer i mekaniske egenskaper ble studert ved å gjennomføre strekktester av materialet før og etter lakkering, mens undersøkelsen av mulig mekanismer som kan gi endringer i egenskaper ble utført gjennom en litteraturstudie. Målinger av elektrisk ledningsevne ble utført for å estimere mengden Mn i fast løsning. I tillegg ble resultater fra karakteriseringen og fra varmeeksperimenter utført av forfatteren i et tidligere arbeid brukt for å kunne bestemme tilstanden til materialet før lakkering og se på effekten av korte varmeeksponeringer.

Materialet som ble undersøkt i denne oppgaven er en 3005 legering med kjemisk sammensetning 1.13 vt% Mn, 0.57 vt% Fe, 0.45 vt% Si, 0.17 vt% Cu, 0.31 vt% Mg og 0.10 vt% Zn. På forhånd var materialet blitt støpt og forvarmet ved 570°C, etterfulgt av varm og kaldvalsing ned til en tykkelse på 0.3 mm og en deformasjonsgrad på 92%. Materielt ble videre glødet ved 224°C til H27 etterfulgt av lakkering. Under lakkeringsprosessen blir lakken tørket i to ovner, ovn 1 har en temperatur på 232°C og ovn 2 har en temperatur på 253°C. Varigheten på begge varmeeksponeringene er på 19 sekunder og blir etterfulgt av bråkjøling etter hver ovn.

Resultatene fra strekktestingen viste at lakkeringsprosessen har endret de mekaniske egenskapene i legeringen, men endringen i styrke var vanskelig å tallfeste grunnet variasjoner i målingene. Reduksjon i uniform tøyning var den mest vedvarende endringen etter lakkering. Basert på disse resultatene, er det ikke noe som tilsier at lakkeringsprosessen kan føre til rekrystallisasjon og mengden gjenvinning som kan skje er neglisjerbar. Muligheten for «concurrent precipitation» av Mn-dispersoider og presipitering av Mg_2Si ble vurdert som usannsynlig med bakgrunn i mikrokjemien til legeringen, tiden og temperaturen på varmeeksponeringen og relevante observasjoner fra litteratur. Likheter med et rapportert herdefenomen i starten av gløding av 3xxx legeringer ved lave temperaturer, tilsier at de observerte endringer i mekaniske egenskaper muligens kan være relatert til clustere av Mn og andre legeringselementer eller veldig små presipitater av Si. Det er vanskelig å fastslå om dette kan skje under lakkering, siden litteraturen ikke har klart å konkludere rundt mekanismen bak herdefenomenet. Et grunnlag for herding fra en tøyningsvei-endring er diskutert med bakgrunn i relevante observasjoner fra litteratur på påvirkningen av dislokasjonsstruktur og anisotropi på mekaniske egenskaper ved en tøyningsvei-endring.

Contents

Abbreviations

APT	Atom Probe Tomography
BSE	Backscatter Electron
DC	Direct Chill
DDW	Dense Dislocation Wall
DSC	Differential Scanning Calorimetry
EBSD	Electron Backscatter Diffraction
ECD	Equivalent Circle Diameter
GNB	Geometrically Necessary Boundary
HAGB	High Angle Grain Boundary
HOA	Hardening on Annealing
IDB	Incidental Dislocation Boundary
IQ	Image Quality
LAGB	Low Angle Grain Boundary
LB	Lamellar Boundary
MAGB	Medium Angle Grain Boundary
MB	Microband
ND	Normal Direction
ODF	Orientation Distribution Function
PFZ	Precipitate Free Zone
PSN	Particle Stimulated Nucleation
RD	Rolling Direction
SEM	Scanning Electron Microscope
SIBM	Strain Induced Boundary Migration
SPC	Strain Path Change
TD	Transverse Direction
XRD	X-ray Diffraction

1   Introduction

Aluminium alloys are the second most used alloy after steels, due to their combination of strength, corrosion resistance and light weight. They are widely used in the packing, transport and building industry. In addition, aluminium alloys have good recycling abilities as it is possible to reduce the energy consumption by 95% through recycling compared to primary aluminium production [1].

The 3xxx aluminium alloys are non-heat treatable, where strengthening is achieved by additions of alloying elements and thermomechanical processing. Rolled aluminium alloy sheets are typically produced by homogenization or pre-heating, rolling and annealing to achieve a desired combination of ductility and strength. These sheets are further processed to accommodate customers preferences, such as lacquering. Subsequent to the lacquering process, a change in mechanical behaviour has been observed. For a 3xxx aluminium alloy, the strength has been seen to increase combined with a reduction in total elongation. The work in the present thesis is motivated by the importance to understand the mechanisms that can contribute to the observed changes in mechanical behaviour.

The scope of this work is to quantify the evolution in mechanical properties in a AA3005 after lacquering and to investigate the possible phenomena that can influence the mechanical behaviour in alloy from the lacquering process. The objective is to investigate the influence of the exposure to elevated temperatures during the drying of the lacquer and strain path changes. The drying of the lacquer consists of heating the alloy in two ovens, the temperature in the first and and second oven are 232°C and 253°C, respectively. Both heat exposures last for 19 seconds and are followed by quenching down to room temperature after each oven. Prior treatment of the as received material alloy is pre-heating, hot and cold rolling to a rolling reduction of 92% and annealing at 224°C, achieving a temper of H27.

Initially, a characterization of the material combined with further heat experiments were planned. However, due to the breakout of COVID-19, the thesis had to be altered and modified into a literature review, as the access to laboratories was restricted. Previous research on low temperature annealing and the mechanisms causing hardening from strain path changes in 3xxx alloys have been reviewed in order to find explanations for the observed changes in strength and elongation. As the present investigation is the continuation of the work conducted by the author during the specialization project [2], the results from this investigation has been utilized as well.

2   Theory

The theoretical aspects for this project are presented in the following section. An introduction of wrought aluminum alloys and the 3xxx series is given in the first part, followed by a brief description of the thermomechanical process for production of aluminium sheets and the homogenization process of 3xxx aluminum alloys. An overview of the evolution microstructure during cold rolling is given in the next part followed by a description of the different phenomena occurring during annealing, including recovery, recrystallization and precipitation. This is followed by a description on deformation and recrystallization texture components. Strengthening mechanisms in aluminium alloys, anisotropy and strain path changes are presented in the last part.

2.1   Non-Heat Treatable Aluminium Alloys

Wrought aluminium alloys are divided into two main groups: heat treatable and non-heat treatable alloys. Non-heat treatable alloys are initially strengthened by additions of alloying elements and a further increase in strength is obtained by cold deformation. Typically, both higher additions of alloying elements and higher degrees of cold deformation increases strength as seen in Figure 2.1. In general, heat treatments of these alloys will not cause an increase in strength as no strengthening dispersoids forms in the alloy (except for dispersoids in 3xxx alloys). In contrast, heat treatable alloys achieves higher strength upon heating due to precipitation of strengthening precipitates. Alloying series that are non heat treatable are high purity and commercially purity aluminium alloys (1xxx), manganese containing alloys (3xxx), silicon containing alloys (4xxx) and magnesium containing alloys (5xxx) [1, 3].
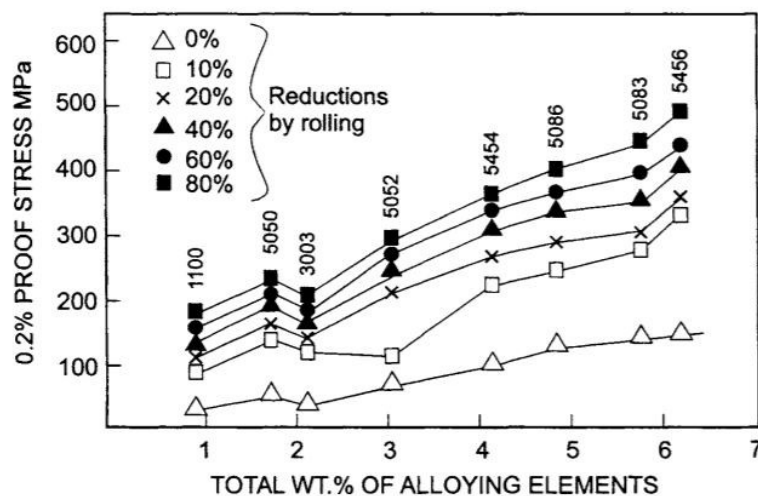

Figure 2.1: Attainable yield strength of non-heat treatable alloys with different levels of cold work and alloying elements [1].

2.1.1   3xxx-Alloys

The 3xxx series are widely used in the packing and building industry because of their combination of medium strength, high ductility and corrosion performance [1]. Due to the high formability, 3xxx alloys are mainly used for beverage can bodies. Other typical products include building facades, ceiling panels and various food packaging products. The alloy has a high thermal conductivity and is therefore often used for heating products and heat exchangers. In the 3xxx series, manganese is the main alloying element which increases strength through solid solution strengthening. To further improve solid solution strengthening, elements such as copper and magnesium are added as well. Higher additions of magnesium are also known to improve corrosion properties and 3xxx alloys can therefore be used in corrosive environments [1, 4, 5]. Elements such as iron and silicon are added as well to enhance the formation of large constituent particles which act as nucleation sites for crystallization after deformation. Mn-bearing dispersoids are known to precipitate during thermomechanical processing and can influence the softening behaviour as well.

2.2   Processing of Aluminium Sheets

A typical process route for the production of non-heat treatable aluminium sheets is in Figure 2.2. It starts with DC-casting of molten aluminium into rectangular ingots followed by sawing and milling to ensure a smooth surface and to remove the segregation zone. Pre-heating or homogenization is conducted to ensure a optimal microstructure before cold deformation and to remove residual stresses [6].
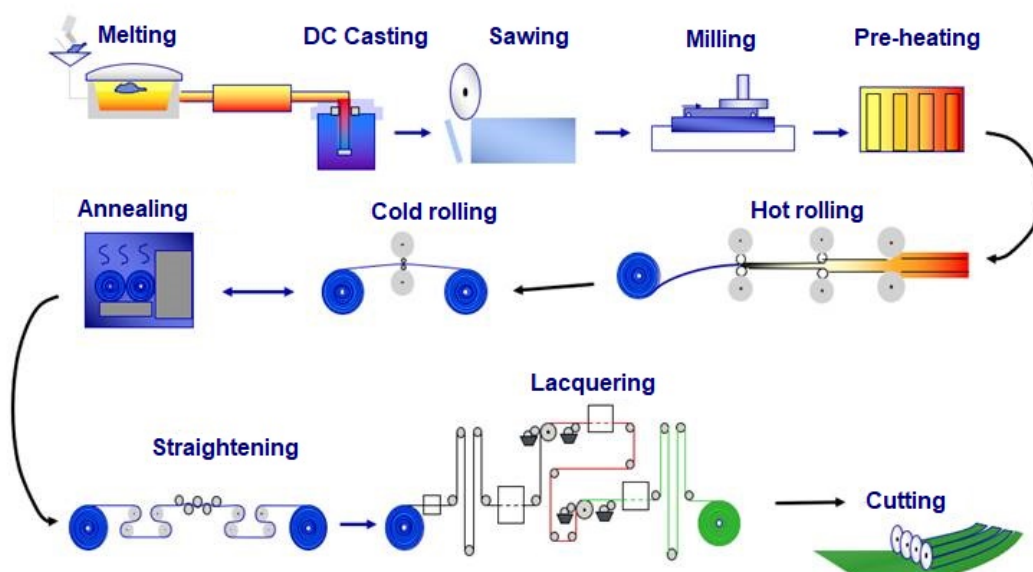

Figure 2.2: Schematic drawing of the production process of aluminium sheet as provided by Hydro.

3

The ingots are then plastically deformed by passing the ingot back and forth between rollers down to a desired thickness. During rolling, large constituent particles are broken up, and the coarse structure is transformed into finer elongated grains. Hot rolling is normally conducted at approximately 300°C, while cold rolling is defined as plastic deformation below 150°C [7–9]. After hot and cold rolling, the sheets are coiled and annealed. Annealing is performed to obtain a desired combination of ductility and strength. The last step of the production process is lacquering or anodizing. In the present thesis, lacquer is applied on the alloy as, illustrated in Figure 2.2. The lacquering process consists of a mechanical application of the lacquer by moving the material forward by the end of the coil, and is further dried in two ovens.

2.3   Homogenization

Homogenization or pre-heating is typically preformed on aluminium alloys after casting to enhance formability prior to thermomechanical processing. The primary objectives of homogenization of 3xxx aluminium alloys are to eliminate micro segregation, reduce the amount of manganese in solid solution and to obtain a desirable size and distribution of fine dispersoids and coarser constituent particles [6, 10]. Both dispersoids and constituent particles will strongly influence the processing of the material, especially recrystallization kinetics, texture development, grain size and mechanical properties. The size and distribution of second phase particles becomes important in regard to control the evolution of microstructure [10].

As a result of high solidification rate of the ingots during casting, most of the Mn content in the as cast state exists in supersaturated solid solution. As described by Haan et al. [11], up to 1 wt% Mn can retain in solid solution due to low diffusivity, even at 600°C. During subsequent heating during homogenization, the supersaturated solid solution will decompose by forming dispersoids. The precipitation behaviour will be influenced by both the heat treatment and the composition of the alloy. Especially, additions of Fe and Si have been shown to influence precipitation [11, 12]. Li and Arnberg [13] observed that both addition of Fe and Si reduced the solubility of Mn and therefore accelerated the rate of precipitation. Fe freely substitutes Mn and precipitates as $\alpha-\text{Al}_{12}(\text{Mn,Fe})_3\text{Si}$ or $\text{Al}_6(\text{Fe,Mn})$ while additions of Si results in $\alpha-\text{Al}_{12}(\text{Mn})_3\text{Si}$ precipitates, when Fe is present in the alloy. Higher additions of Fe favor $\text{Al}_6(\text{Fe,Mn})$ while Si favors the cubic α-phase [13, 14]. The formation of Mn-bearing dispersoids will therefore lead to a reduction of both Si and Fe in solid solution [15]. The α-dispersoids are considered as partially coherent with the Al matrix, and it has been shown that these particles have a high degree of thermal stability [13, 16].

The precipitation behaviour in a DC-cast AA3003 upon continuous heating was investigated by Li and Arnberg [13]. It was found that the supersaturated solid solution starts to decompose by precipitation at 300°C. The dispersoid density increases with temperature and

reaches a maximum at 400°C. The density further decreases while the size of the dispersoids grows continuously with increasing heating temperature. At 530°C, some of the dispersoids may dissolve into the matrix due to an increase of the solubility of Mn, while coarsening remains as the dominant mechanism for the size of dispersoids to grow. When heating to 600°C, coarsening is the predominant process, as long distance diffusion becomes possible due to an increase in the diffusion rate of Mn. At longer holding time, the number density and size of dispersoids decrease, indicating quick dissolution of dispersoids.

In addition to dispersoids, primary particles of $Al_6(Fe,Mn)$ and the α-phase will coarsen during homogenization as Mn and Si diffuses into the particles. A partial transformation of $Al_6(Fe,Mn)$ into α-phase may occur as the composition of the of the particle changes [17]. As the ratio of Mn to Fe and the Si content change in the particle, the α-particle can have different compositions. The transformation causes a depletion of Mn in the Al-matrix around the particles of several μm [8, 10]. Precipitate Free zones (PFZ) are also commonly observed around constituent particles in 3xxx aluminium alloys which is possibly the result of diffusion or reaction of solutes (Mn and Fe) during heating after solidification. The evolution of PFZs are controlled by the dissolution of dispersoids [17, 18].

2.4   Cold Deformation

The final microstructure and texture of the material after thermomechanical processing is heavily influenced by the microstructure developed during plastic deformation. It is therefore important to the characterize the structure in the deformed state, to be able to predict the evolution in microstructure with further annealing or processing.

Cold deformation is a process used to achieve higher strength in metals. A typical cold work process for aluminium is cold rolling, where plastic deformation is introduced by reducing the thickness of the material with rollers as illustrated in Figure 2.3. During cold rolling, significant changes are observed in the microstructure. The grains become elongated along the rolling direction and the total grain boundary area increases [7]. In addition, dislocation structures develop within the grains from the accumulation and generation of dislocations during cold rolling. This acts as a driving pressure for softening and precipitation during annealing [9].
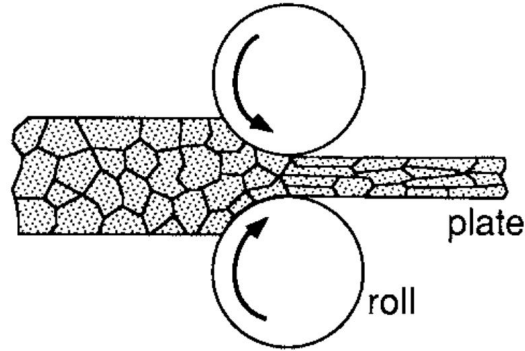
Figure 2.3: Schematic drawing of a material during rolling [19].

Cold rolled materials are typically characterized by their reduction in thickness, measured by either percentage reduction, the logarithmic or von Mises strain. The relations between change in thickness and percentage reduction, logarithmic strain and von Mises strain are given in the equations below:

$$\%\text{red} = \frac{t_0 - t}{t_0} \tag{2.1}$$

$$\epsilon = \ln \frac{t_0}{t} \tag{2.2}$$

$$\epsilon_{vM} = \frac{2}{\sqrt{3}}\epsilon \tag{2.3}$$

where t_0 is the initial thickness, t is the final thickness, %red is the percentage rolling reduction, ϵ is the logarithmic strain and ϵ_{vM} is the von Mises strain [20].

2.4.1   Substructure Characteristics

There are two main mechanisms for deformation in cubic metals: slip and twinning. These mechanisms are mainly dependent on the stacking fault energy of the material. Aluminium alloys have a fcc structure and a high stacking fault energy and deformation is therefore formed by slip. Materials deformed by slip can obtain a well-developed microstructure of subgrains after deformation, as illustrated in Figure 2.4. With small strains, the stored dislocations are arranged into a cell structure of complex tangles and are characterized by a cell wall thickness h, cell size δ, wall dislocation density ρ_w and dislocation density within the cell ρ_i. As the strain increases, the walls collapse into sharp boundaries with a well-defined misorientation φ as seen in Figure 2.4b.

(a)   **(b)**
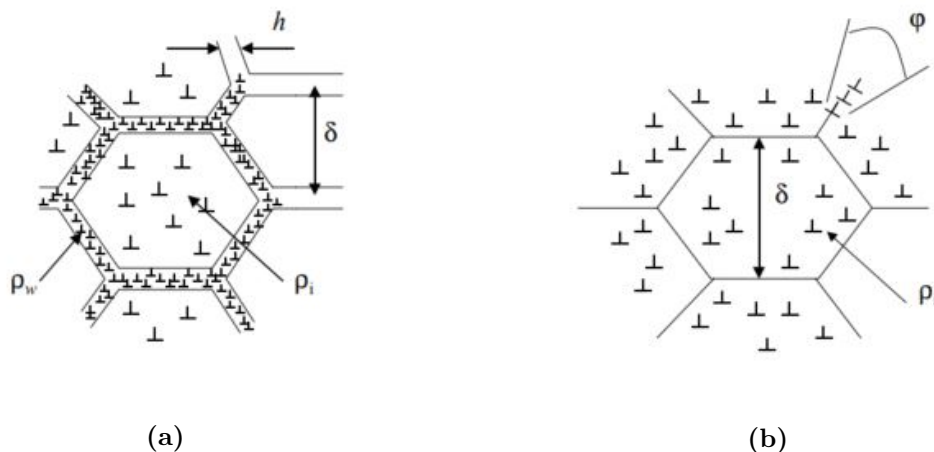
Figure 2.4: Schematic illustration of the microstructural during (a) small deformations and (b) large strains [20].

The typical subgrain characteristics (cell size, dislocation density and misorientation) will evolve with strain. In aluminium alloys, the cell boundaries are well defined even at small strains (below 0.2) and the subgrains are uniform and equiaxed. With increasing strain, a rapid decrease in cell size is typically observed as seen in Figure 2.5 At large strains, the subgrain structure consist of pancake shaped grains parallel with the rolling plane [21]. Gil Sevillano et al. [22, 23] found that a wide range of metals exhibited a similar behaviour, independent of the deformation mode. During the initial deformation period, the evolution of the microstructure is dominated by cell multiplication. At larger strain, the slope of reduction decreases due to a reduced storage rate of dislocations and dislocation wall annihilation.
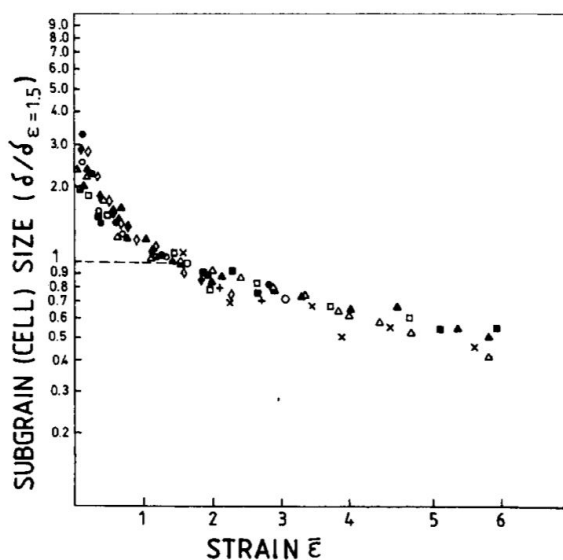
Figure 2.5: Subgrain size as a function of strain [21].

The misorientation, φ, is the difference in crystallographic orientation between two grains. Typically, the grain boundaries are separated into low or high angle grain boundaries

depending on its misorientation. A low angle boundary (LAGB) have a misorientation less than 15° and are also known as subgrain boundaries. A high angle boundary (HAGB) have a misorientation higher than 15°. Various reports have observed a rapid increase in misorientation with increasing strain before it saturates at 2-3° at a strain of 1, as seen in Figure 2.6 [21, 24].
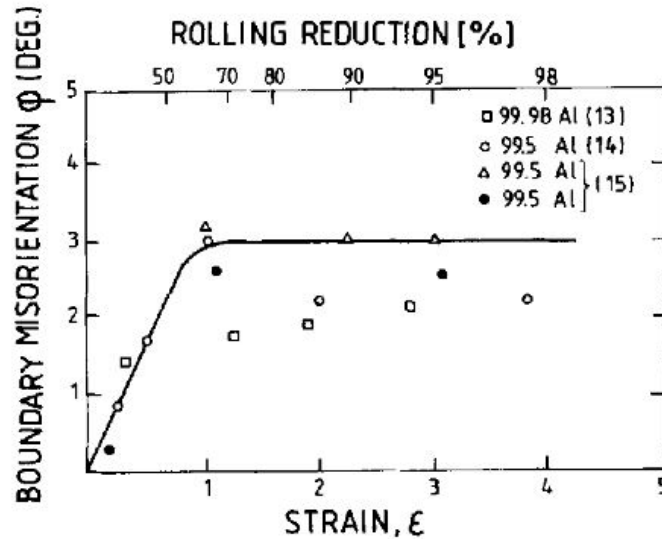
Figure 2.6: Average sub-boundary misorientation as a function of rolling strain in high purity and commercial purity aluminium [21].

The interior dislocation density and subgrain size in AA1050 and AA3207 was investigated by Nord-Varhaug et al. [25] at different strains. It was observed that the dislocation density saturated after cold rolling to strain larger than 0.2. The subgrain size decreased with increasing strain, however the saturated level had not been reached at a strain of 2, as seen in Figure 2.7.
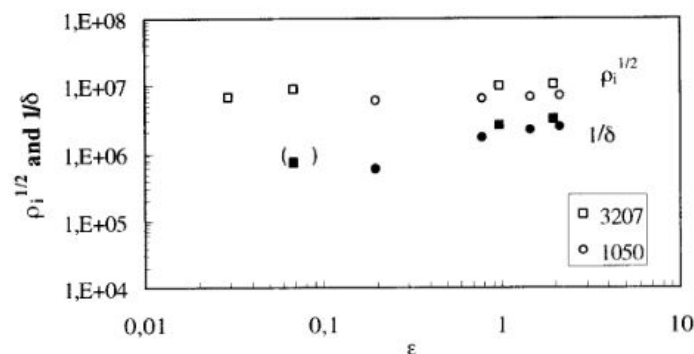
Figure 2.7: The square root of dislocation density (white) and the inverse cell size (black) versus strain [25].

Stored energy

While most of the energy introduced by cold work is released as heat, ~1% remains as stored energy in the material as a result of the generated dislocations [7]. The stored energy is the

driving pressure for recrystallization, recovery and precipitation. A higher strain level leads to an increased driving pressure. The stored energy can be described as a function of the interior dislocation density ρ_i and subgrain size δ, as seen in Equation 2.4.

$$P_D = \alpha \frac{\gamma_{SB}}{\delta} + \rho_i \Gamma \tag{2.4}$$

where G is the shear modulus, b is the Burgers vector,δ is the subgrain size , γ_{SB} is the boundary energy, α is the geometric constant with a expected value of the order 3 and Γ is the dislocation line tension, given by

$$\Gamma = \frac{1}{2} G b^2 \tag{2.5}$$

The last term in Equation 2.4 is often ignored as the interior dislocation density is usually only 1-2% of the total stored energy [26]. The boundary energy γ_{SB} is given by the Read-Shockley relationship:

$$\gamma_{SB} = \frac{Gb\varphi}{4\pi(1-v)} \ln\left(\frac{e\varphi_c}{\varphi}\right) \tag{2.6}$$

where φ is the boundary misorientation, φ_c is the critical misorientation separating between high and low angle boundary (at 15°) and v is the Poisson's ratio.

2.4.2   Deformation Heterogeneities

The equiaxed dislocation cells that form at the initial stage of small strain is the smallest volume element in a grain. The cells are separated by incidental dislocation boundaries (IDBs). Surrounding the cell blocks is long flat dislocation boundaries, termed dense dislocation walls (DDWs) and double walled microbands (MBs) in Figure 2.8a. These boundaries are the result of crystallites that are deformed by different slip systems and are known as geometrically necessary boundaries (GNBs) [27]. Microbands are crystallographic in nature and form on {111}-slip plane in fcc-metals [8]. They dominate the sub-structure evolution at low to intermediate strains. Microbanding is the typically slip mode in aluminium alloys with a high content of element in solid solution due to an increased capability to store dislocations. In general, they have a small misorientation (1°) with respect to the surrounding matrix and do not act as nucleation site for recrystallization. With larger strain, the cell blocks becomes elongated in the rolling direction and are separated by lamellar dislocation boundaries (LBs), as illustrated in Figure 2.8b [28, 29].
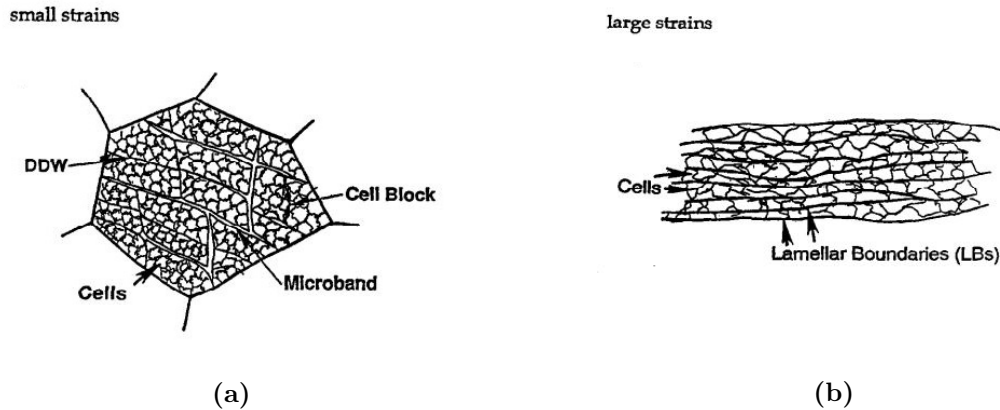
Figure 2.8: Schematic drawing of the deformation microstructures and grain subdivision at (a) small strain and (b) large strains [27].

It is often seen during deformation that grains subdivide into regions with different orientation. These regions are referred to as deformation bands and are the result of inhomogeneous stresses applied from neighbouring grains or instability of the grain itself during deformation. The narrow band between deformation bands are termed transition bands. They have a sharp orientation gradient which make them ideal for nucleation [7].

Shear banding occurs when the dislocation density saturates from intense shearing strain. The material becomes unstable with respect to shear and shear banding becomes an alternative slip mode. These bands are not crystallographic and can therefore pass through several grains, usually with a 35° to the rolling plane and parallel to the transverse direction in rolled material. Inside the band, fine subgrains are elongated in the band direction with a sharp misorientation (10°- 40°) to the surroundings [7, 30].

Aluminium alloys containing hard second phase particles, form deformation zones during deformation. The size and microstructure of the deformation zones are dependent on applied strain, particle size and temperature. In rolled alloys, the zone is usually elongated in the rolling direction [7]. The deformation zones develop around constituent particles larger than 1 µm and consist of a rotated zone with highly misorientated small subgrains found close to the particle, as illustrated in Figure 2.9. Further away from the particle, the subgrains become elongated and distorted, referred to as the distorted region in Figure 2.9. These zones can act as nucleation sites for recrystallization, due to a locally high stored energy from small subgrains, high dislocation density and a high misorientation gradient between the matrix and the particle, consisting of HAGBs. The nucleation mechanism for creation of recrystallization nuclei is termed particle stimulated nucleation (PSN) which is further discussed in Section 2.5.2.
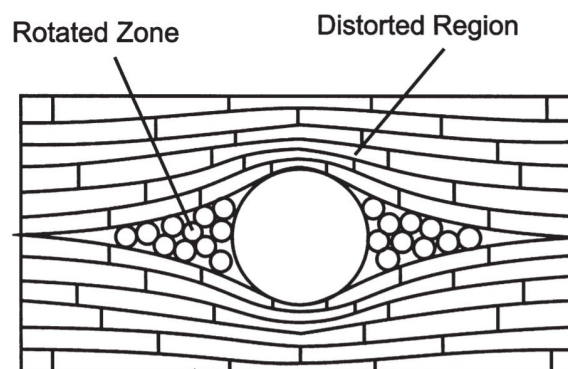
Figure 2.9: Schematic illustration of a deformation zone around a constituent particle [31].

Old grain boundaries are already present in the microstructure before deformation as equiaxed grains. As mentioned, grains become flat and elongated with cold deformation. The grain boundaries acts as obstacles for dislocation movement similar to a constituent particle, resulting in a sharpening of the of the lattice rotation and a refinement of the structure close to the boundary [32]. Thus becoming ideal sites for nucleation by strain induced boundary migration (SIBM) due to high local stored energy and the misorientation [9].

2.5   Annealing

Annealing is conducted after cold deformation to restore the ductility in the material. During annealing, the material is heated and held at an elevated temperature for a specific amount of time. There are three main phenomena occurring during the annealing processes, which are recovery, recrystallization and precipitation. Recovery involves annihilation and rearrangement of dislocations into low energy configurations and subgrain growth. Typically, recovery occurs at the initial stages of annealing and at lower temperatures. During recrystallization, new strain free grains nucleate and consume the deformed and recovered microstructure. Both recovery and recrystallization lead to a reduction in hardness. Concurrent precipitation involves the formation of dispersoids which retard recovery and recrystallization [7, 9, 10, 33].

2.5.1   Recovery

Recovery refers to the process where the stored energy is reduced in the deformed material without any changes in the grain structure. During recovery, properties will partially be restored to their values before deformation was conducted through rearrangement and annihilation of dislocations [33]. It is termed static recovery when the process occurs prior to recrystallization during heat treatment, while dynamic recovery occurs during deformation [7]. It is sometimes difficult to differentiate recovery from recrystallization, however it has been suggested by Doherty et al. [29] that recovery is all annealing processes occurring in deformed materials that occur

without the migration of a high angle grain boundaries. The subgrains formed during recovery consist therefore mainly of low angle boundaries, with a misorientation less than 15°. As both recovery and recrystallization are driven by the stored energy of the deformed state, these are competitive processes. A significant amount of recovery will lower the stored energy and therefore affect the recrystallization kinetics. In addition, the formation and growth of subgrains can influence the nucleation behaviour of the recrystallization [7].
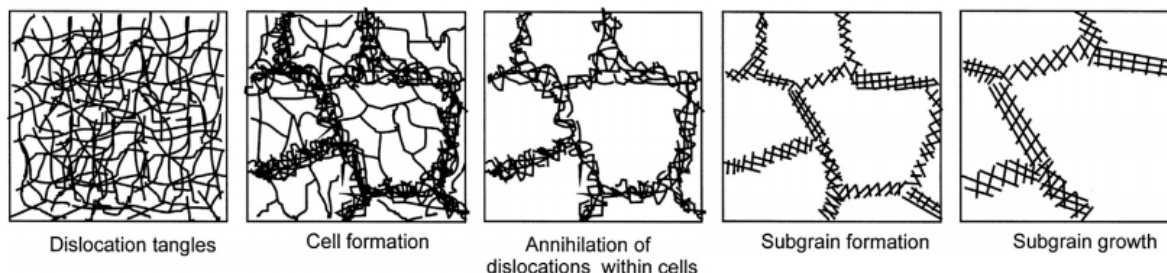
Figure 2.10: Various stages in the recovery of a deformed material [7].

The structural changes during recovery are illustrated in Figure 2.10. Initially, there are a rapid loss of point defects followed by annihilation and rearrangement of dislocations, subgrain formation and subgrain growth. The various stages of recovery can occur simultaneously. Furthermore, alloys with high stacking fault energy such as aluminium alloys, can form a well developed cell structure during deformation.

In the early stages of annealing, the reduction in stored energy is caused by the annihilation and rearrangement of dislocations. Dislocations of Burgers vectors of opposite signs annihilate, and the excess dislocations which cannot be removed by annihilation will rearrange into low grain angle boundaries, transforming the cell structures into subgrain structure through glide, climb and cross-slip. The simplest form of rearrangement of dislocations is known as polygonization, where a tilt boundary is formed. A tilt boundary consisting of an array of parallel edge dislocations [7, 34, 35]. For a tilt boundary, the angular misorientation θ across the boundary is given as [34]:

$$\theta = \frac{b}{h} \tag{2.7}$$

where b is the magnitude of the Burger vector of the dislocation in the boundary h. The energy of a tilt boundary is given by the Read Shockley equation (cf. Equation 2.6). According to the Read-Shockley equation, the energy of a boundary increases with increasing misorientation, as illustrated in Figure 2.11. The dislocation spacing is very large at small misorientations and will further be reduced with increasing misorientation, where the strain fields of the dislocations will cancel out [34]. As a result, the rate of increasing energy decreases with increasing misorientation

(i.e. the energy per dislocation decreases with increasing misorientation), and it is therefore a driving force to form fewer and more misorientated boundaries [7].
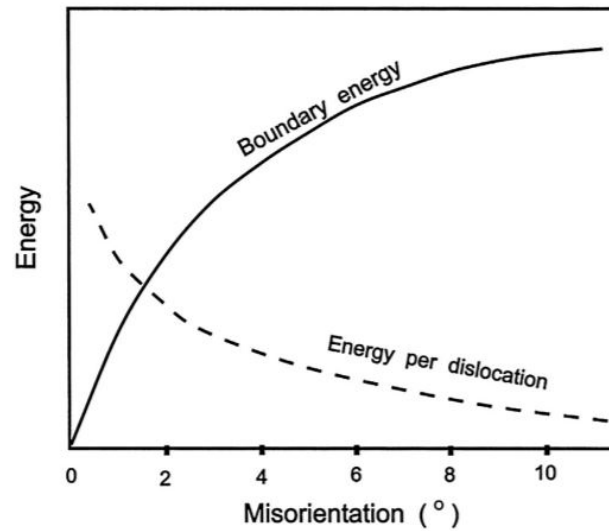
Figure 2.11: The energy of a tilt boundary and the energy per dislocation as a function of misorientation [7].

The stored energy is further lowered during recovery due to subgrain growth, which leads to a reduced area of low angle boundaries in the alloy [7]. The most accepted mechanism for subgrain growth is subgrain migration where smaller subgrains are consumed by larger subgrains. In addition, an alternative mechanism where proposed by Hu [36], based on subgrain rotation and coalescence, which is of importance after small deformations and at low temperatures.

In the presence of particles, subgrain growth may be controlled by coarsening of particles. As recovery occurs during annealing, the subgrains will grow and stabilize at a size given by the interparticle spacing. As the particles are coarsened with further annealing, the interparticle spacing increases and the subgrains are allowed to grow. This is referred to as extended recovery [7].

(a)   (b)
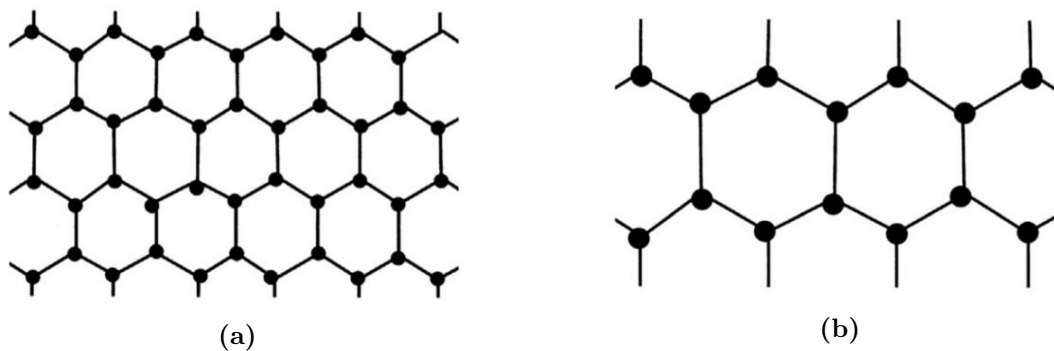
Figure 2.12: Extended recovery controlled by the coarsening of second-phase particles [7]

2.5.2   Recrystallization

Recrystallization is the process involving nucleation and growth of strain free grains with low dislocation density, leading to a softer material. The difference from recovery is that high angle grain boundaries migrate during recrystallization and will consume both the deformed and recovered microstructure. The driving force for recrystallization is the difference in internal energy between the unstrained and strained material [7, 30].

A series of statements have been formulated to rationalize the recrystallization behaviour. By condensing recrystallization as a thermally activated nucleation and growth phenomenon, the effect of initial microstructure and annealing temperature and deformation strain, on the time for recrystallization and on the grain size after recrystallization can be predicted [7]. The statements are as following:

1. A minimum deformation is required to provide a nucleus and the stored energy for it to grow.
2. The temperature needed for recrystallization to occur decreases as the time of annealing increases.
3. The temperature required for recrystallization to occur decreases as strain increases. As strain increases, the stored energy which provide the driving pressure for recrystallization, increases. A higher strain also promotes nucleation of new grains
4. The recrystallized grain size decreases with increasing deformation as large amount of deformation provides more nuclei per unit volume.
5. The recrystallization temperature will increase with a larger starting grain size and higher deformation temperature. As grain boundaries are favorable nucleation sites, a large initial grain size provides fewer nucleation sites leading to a lower nucleation rate. A higher deformation temperature leads to recovery which lowers the driving pressure.

Furthermore, the solute content and second phase particles will influence as well. Solutes retard recrystallization by hindering grain boundary movement and is referred to as the solute drag [30]. Larger constituent particles promote recrystallization through PSN, which is further explained later in this section and results in weak recrystallized texture [7]. In contrast, small dispersoids hinders recrystallization through a Zener drag. The Zener drag results in slower recrystallization kinetics and larger recrystallized grains which is further explained in Section 2.5.3.

The JMAK-equation is often used to model recrystallization kinetics where the fraction recrystallized grains is given by [37–39]:

$$X_v(t) = 1 - \exp(-kt^n) \tag{2.8}$$

where k is a constant, t is time and n is the growth exponent. The model is based on constant growth rate in three dimensions and assumes a random distribution of nucleation sites. In theory, the growth exponent is equal to 3 with site saturation nucleation kinetics, which occurs when the nucleation rate decreases so rapidly that all nucleation events effectively occur simultaneously at the start of recrystallization. At a constant nucleation rate, n=4 is applied. However, the measured n-value for aluminium alloys are approximately 2 or less [31]. The final recrystallized grain size D_{rex} is calculated as following [26]:

$$D_{rex} = \left(\frac{1}{N_{tot}} \right)^{\frac{1}{3}} \tag{2.9}$$

Where N_{tot} is the number of nucleation sites per volume.

It is assumed for recrystallization that all the nuclei are present in the deformed state and that they grow at a constant rate. In order to grow, the nuclei must be thermodynamically stable and of a certain size. The critical diameter (σ_c) of a nuclei can be calculated by the Gibbs-Thomson relation [26, 34]:

$$\delta > \delta_c = \frac{4\gamma_{gb}}{P_D - P_Z} \tag{2.10}$$

where δ is the diameter of a deformation free volume, γ_{gb} is the specific grain boundary energy, P_D is the stored energy, P_Z is the Zener drag. The nuclei will grow at a rate v given by [26]:

$$v = M(P_D - P_Z) \tag{2.11}$$

where mobility M of the grain boundary is defined by [26]:

$$M = \frac{M_0}{RT} \cdot \exp\left(\frac{-U_{GB}}{RT} \right) \tag{2.12}$$

where U_{GB} is the activation energy for grain boundary migration, M_0 is a constant, R is the universal gas constant and T is temperature. The mobility will in some cases be influenced by their misorientation as illustrated in Figure 2.13, due to a special orientation relationship. These boundaries are referred to as special high angle boundaries [34]. An example of such a boundary is the 40° <111> tilt boundary [7]. It has been observed that the mobility of the 40° <111> tilt boundary in a high purity Al-0.05wt% Si alloy is 10 times larger than the 40° <111> twist boundary, where the twist boundary had a similar mobility as those seen for random high angle boundaries [40, 41].
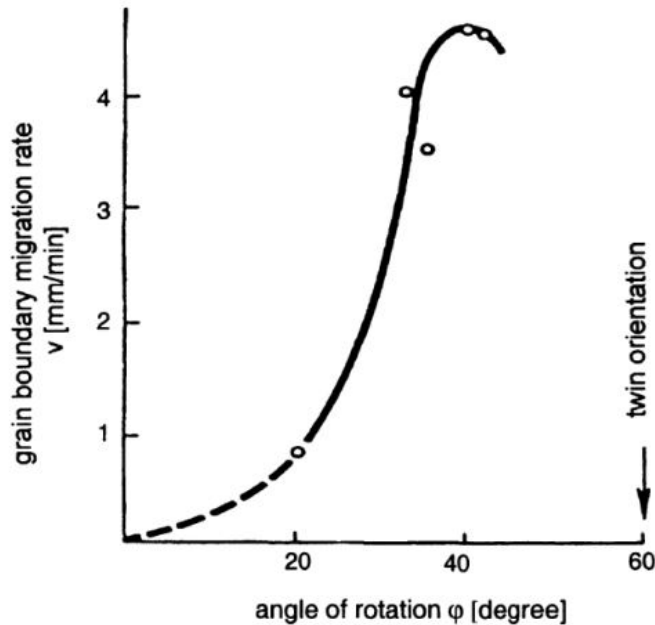
Figure 2.13: Dependence of the grain boundary migration rate on the angle of rotation of <111> tilt boundaries in aluminium [42].

In general, a nuclei will grow rapidly when having a high misorientation relationship to the neighbouring deformation structure. Nucleation occurs typically at heterogeneities in the deformed microstructure which include shear bands, transition bands, deformation zones and pre-existing high angle grain boundary. The mentioned heterogeneities are presented below.

Shear bands

As described in Section 2.4.2, recrystallization may occur in shear bands due to the high stored energy and a large orientation gradient. While shearbanding occurs in several materials, Nes and Hutchinson [43] found that the orientations of the nucleated grains were very case dependent. In aluminium, Hjelen et al. [44] reported that S orientation is prominent. The grain orientations in an α-brass investigated by Duggan et al. [45], were found to be widely scattered.

Transition bands

As reported by Dillamore et al. [46], transition bands act as a nucleation site for recrystallization. Rapid subgrain growth may occur due to the sharp misorientation gradient in the band which result in the formation of a high angle boundary after small amount of growth [8]. The orientation of the recrystallized grains are a direct result of the slip process and the strain path. In aluminium, Hjelen et al. [44] reported of nucleation of both cube and Goss oriented grains.

Strain induced boundary migration

Strain induced boundary migration (SIBM) occurs when a pre-existing high angle grain boundary bulges out due to differences in stored energy on each side of the grain boundary, as

seen in Figure 2.14. The difference in stored energy is the result of unequal subgrain size. The side with the largest subgrain size and therefore lowest stored energy, will grow at the expense of the side with smaller grain. According to Somerday and Humphreys [47], SIBM has been shown to be an important nucleation mechanism in Al-Mn1.3 alloy cold rolled to 90%.
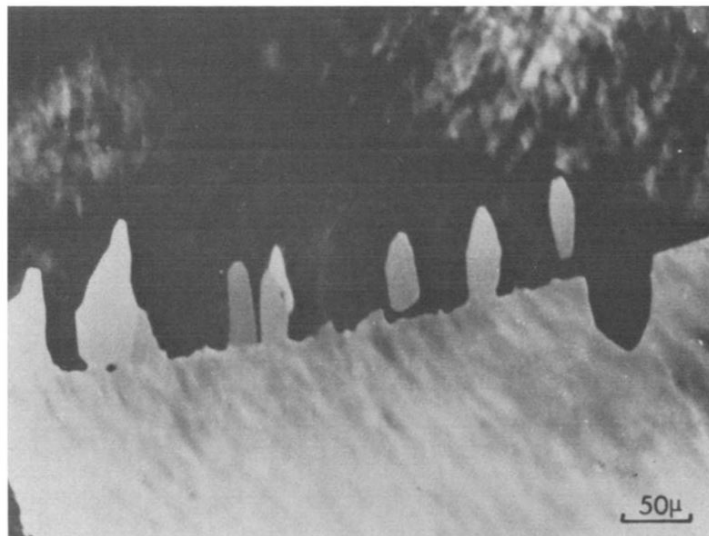
Figure 2.14: Nucleation by SIBM at a prior high angle grain boundary in a high purity aluminium, compressed 40% [48].

Ordinary grain boundary nucleation

Ordinary grain boundary nucleation also occurs at pre-existing grain boundaries. However, the new grains have significant different orientation from the parent grains and are separated from the parent grains by sharp boundaries [8]. This mechanism was observed by Hutchinson in iron bicrystal [49], where the new grain was rotated of with 30°from the orientation from the parent grains. The mechanism behind this type of recrystallization and the grain orientations of the recrystallized grains are still unclear [7].

Particle Stimulated Nucleation

Nucleation at deformation zones are an important nucleation mechanism in alloys containing particles. Particle stimulated nucleation (PSN) occurs in deformation zones surrounding large constituent phase particles due to high stored energy and large misorientation gradients, which are ideal for nucleation [7]. PSN is found to occur in alloys with particles larger than a critical diameter [50]. Humphreys [50] reported that the critical diameter is approximately 1 µm for a deformed aluminium alloy. As the number of nucleation sites are determined by constituent particles, the recrystallization can be controlled by composition and processing of the alloy [7].

Several characteristic features of PSN have been found. Firstly, recrystallization originates at a pre-existing subgrain within the deformation zone, but not necessarily at the particle surface. Second, nucleation occurs by rapid sub boundary migration. The orientation gradient within

the deformation zone promotes rapid formation of mobile high angle grain boundaries as the sub grain growth velocity is proportional to the magnitude of the orientation gradient. A recrystallization nucleus is formed when the misorientation have reached 10-15°, which is equal to a HAGB. Last, the grain may stop growing when the deformation zone is consumed as the material further away from the particle is less deformed and with a lower lattice curvature [7, 33].

2.5.3   Precipitation

Precipitation is associated with the decomposition of supersaturated solid solution. As mentioned, most of the Mn exist in solid solution and the solubility is reduced as the alloy is cooled down. This results in a solute level which exceeds the solubility of the solid solution and the Gibbs free energy is increased [51]. The system minimizes the energy by decomposition of the solute, which occurs as nucleation and growth of Mn-bearing dispersoids. Nucleation occurs at heterogeneities, such as subgrain and grain boundaries, dislocations and clusters of vacancies, as the average free energy is higher at heterogeneities than in the matrix. The most common dispersoids seen in 3xxx aluminium alloy are Al_6(Mn,Fe) and α-Al(Mn,Fe) and will influence the recrystallization kinetics through the Zener drag and concurrent precipitation during annealing.

The Zener drag

The Zener drag is the retarding force exerted on grain boundaries from the dispersion of small precipitates or dispersoids [52]. The interaction between the precipitates and a moving boundary are illustrated in Figure 2.15b. At $t=t_1$, the grain boundary moves unhindered. However, as the grain boundary intersects with the particle at $t=t_2$, a part of the grain boundary ceases to exist due to equilibrium between the surface tensions at the interface between the particle and grain boundary resulting in a lowering of energy [53]. A force must therefore be applied to separate it from the particle.
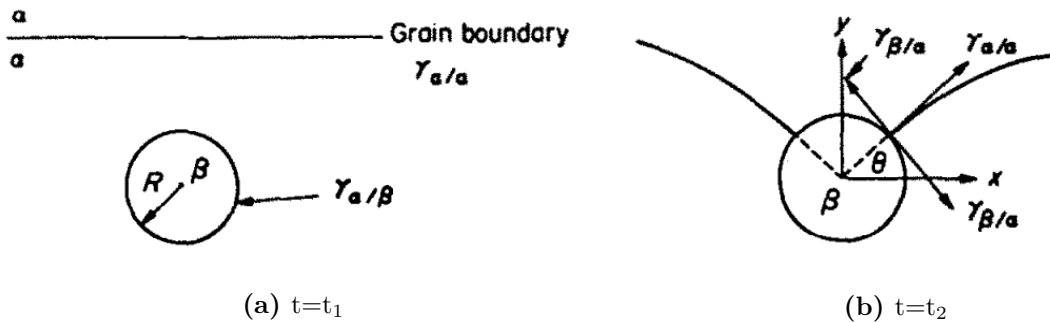

(a) t=t$_1$ **(b)** t=t$_2$

Figure 2.15: Schematic illustration of the pinning effect of a spherical particle on a moving grain boundary [53].

The interaction force acting on a grain boundary from a incoherent spherical particle is given as:

$$F = 2\pi r \gamma_{gb} \cos\theta \sin\theta \qquad (2.13)$$

where r is the radius of a circular particle, γ_{gb} is the grain boundary energy and θ is the angle where the particle meets the grain boundary, as seen in Figure 2.15b. The max force on the grain boundary from a particle is at $\theta = 45°$ [53, 54]. For a random distribution of particles, the Zener drag is expressed as:

$$P_z = \frac{3f\gamma_{gb}}{2r} \qquad (2.14)$$

where f is the volume fraction of particles with equal radius r [53]. The Zener drag retards both high and low angle grain boundaries and affects therefore both recovery, recrystallization and grain growth. During recovery, dispersoids prevents the subgrains from growing large enough to nucleate new strain free grains which retards nucleation and growth of recrystallized grains leading to larger recrystallized grain size. During recrystallization, the precipitates retards grain boundary movement, resulting in slower recrystallization kinetics.

Concurrent Precipitation

The softening behaviour of a supersaturated aluminium alloy can be influenced by precipitation during annealing. If the precipitation occur before recrystallization has completed, the dispersoids may affect the softening reactions. The phenomenon is referred to as concurrent precipitation and was first investigated by Hornbogen and Köster on two saturated and deformed aluminium alloys [55].

The recrystallization and precipitation behaviour as a function of time and temperature is schematically illustrated in a time-temperature-transformation (TTT) diagram in Figure 2.16 for a material rapidly heated to the annealing temperature [31]. The start and finish line for recrystallization are those found for dilute alloys without precipitation. The precipitation line represents the occurrence of sufficient precipitation to affect the behaviour of recrystallization and the intersecting points A and B represent the interaction between the two processes, precipitation and recrystallization. The diagram is divided into three regions I, II and III.
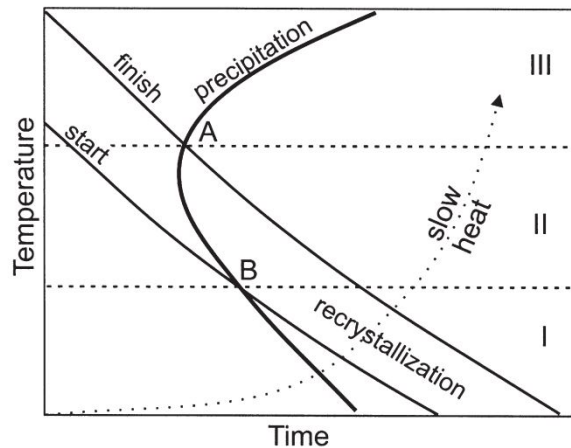
Figure 2.16: Schematic TTT-diagram for recrystallization and precipitation in cold rolled aluminium alloys, rapidly heated [31].

Above the temperature T_A in region III, recrystallization will be fully completed before any precipitation has occurred. The microstructure will consist fine equiaxed grains. Below T_A, both recrystallization and precipitation may occur. In region II, precipitation occurs simultaneously with recrystallization. As seen from Figure 2.16, various amount of recrystallization will occur before precipitation starts. Higher temperature leads to an increased amount of recrystallization before precipitation occurs. As precipitation begins, dispersoids will pin the grain boundaries, resulting in slower recrystallization. The slowed down recrystallization causes the number of recrystallized grains to be low which gives each grain a lot of space to grow, giving the coarse grain structure. In region I, a significant amount precipitation occurs before the recrystallization have started and can therefore inhibit recrystallization through the Zener drag. In addition, the heating rate will influence as well. A slow heating rate result in a high density of precipitates which cause the starting temperature for recrystallization to increase [7].

2.6   Texture

Texture refers to the statistical distribution of crystallographic orientations in a polycrystalline material [56]. During manufacturing, metals develop preferred grain orientations depending on the thermomechanical process as deformation will occur by gliding dislocations on the most favourably oriented slip system. Thus, making it possible to characterize and control the texture development during processing which is important as texture gives rise to anisotropic properties. The crystallographic orientations in the material are expressed relative to an external fixed coordinate system. For rolled products, the coordinate system is given by the rolling direction (RD), transverse direction (TD) and normal direction (ND). Texture is typically be represented as pole figure, orientation distribution functions or inverse pole figures and is measured using EBSD and XRD [30, 56, 57].

A pole figure is a stereographical projection showing the distribution of a chosen crystallographic direction with respect to a reference coordinate system. The pole figure is created by the intersection area between the normal plane to the chosen direction and the unit sphere. The construction of the equatorial (100) pole figure is illustrated in Figure 2.17, where the chosen crystallographic direction is the normal to the (100) plane. As illustrated in Figure 2.17c, the projection points will be evenly distributed for a material with randomly oriented grains. In contrast, a material with grains with a preferred orientation will cluster together in certain areas of the pole figure, as illustrated in Figure 2.17d, which is often referred to as a strong or sharp texture. Pole figures are often presented with contour lines rather than showing the individual points as shown in Figure 2.17e [30].
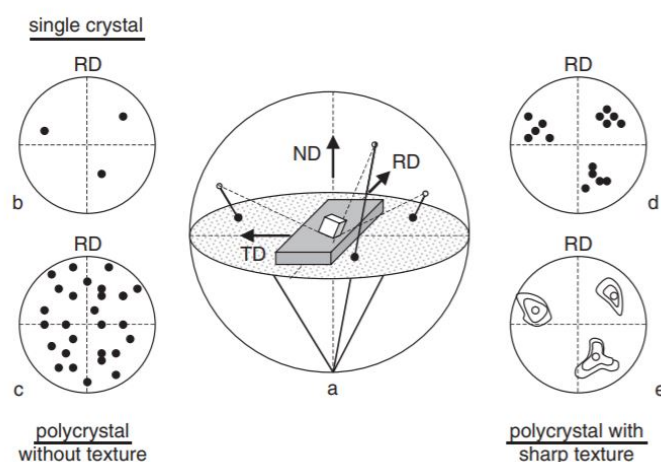
Figure 2.17: Construction of a (100) pole figure. (a) Stereographic projection of the (100) poles; (b) projection of the (100) poles of one grain on the equatorial plane; (c) projection of the (100) poles of a polycrystal; (d) projection of the (100) poles of a textured polycrystal; (e) contour map of the (100) pole density distribution [30].

However, the description of texture from pole figures is incomplete as a pole figure is only a 2D representation while three parameters are required to describe a grain orientation. A complete description is can be provided by using the orientation distribution function (ODF). The ODF describes the orientation distribution of the grain orientations using the Euler angles (φ_1, Φ, φ_2). The Euler angles describes how to rotate the specimen coordinate system onto the reference coordinate system. The most commonly used way of expressing the Euler angles is formulated by Bunge as illustrated in Figure 2.18. The rotations are [56]:

1. A rotation φ_1 about the normal direction ND, transforming the transverse direction TD into TD' and the rolling direction RD into RD'
2. A rotation Φ about the axis RD' (in its new direction)
3. A rotation φ_2 about ND" (in its new direction)
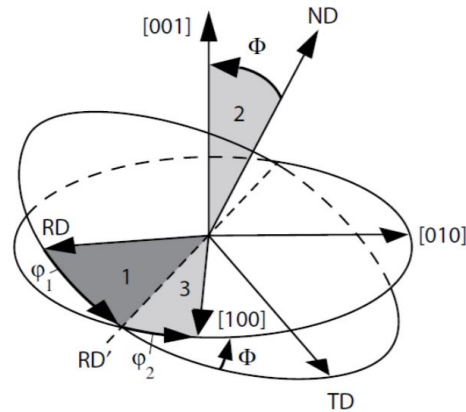
Figure 2.18: Diagram showing how rotation through the Euler angles in order 1, 2, 3 [56].

The three Euler angles represents the axes in a three dimensional space called the Euler space as seen in Figure 2.19. Each point in the Euler space corresponds to a crystal orientation. The angles are defined over $0° \leq (\varphi_1, \varphi_2) \leq 360°$ and $0° \leq \Phi \leq 180°$. For crystals with cubic crystal symmetry (e.g. from rolling) the range of the angles is reduced to $0° \leq (\varphi_1, \varphi_2, \Phi) \leq 90°$ [30, 56].
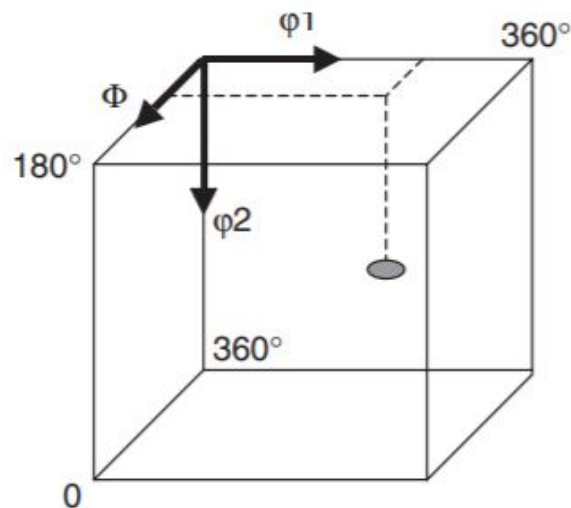
Figure 2.19: Schematic illustration of the Euler space with a graphical representation of a crystallographic orientation (grey circle) with Euler angles: $\varphi_1 = 270°$, $\varphi_2 = 60°$ and $\Phi = 180°$ [30].

In literature, the Euler space is presented as two-dimensional sections with a 5° interval of the angle φ_2. A schematic illustration of the sections is seen in Figure 2.20.
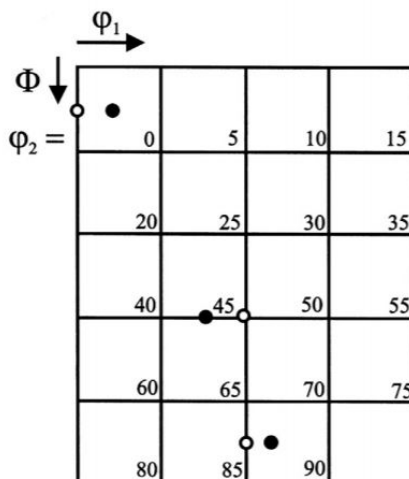
Figure 2.20: ODF sections with a 5° interval. The Euler section is reduced to $0° \leq (\varphi_1, \varphi_2, \Phi) \leq 90°$. The orientation $\{110\}<112>$ and $\{110\}<001>$ orientations are given as filled circles and an open circles, respectively [7].

By expressing the orientation g as:

$$g = (\varphi_1, \Phi, \varphi_2) \tag{2.15}$$

The ODF can be defined as [58]:

$$ODF = \frac{dV(g)}{V} = f(g)dg \tag{2.16}$$

Where V is the total sample volume, dV is the volume of a crystallite possessing the orientation g in the range dg.

2.6.1   Deformation Texture

During plastic deformation, the grains in a polycrystal will change shape and orientation depending on applied stress. The intensity of the texture increases with increasing deformation. Deformation texture for fcc alloys with high stacking fault energy after plane strain deformation can be represented as fibers through the Euler space. The α fiber consist of Goss and Brass-orientation, where all orientations have a $<011>$ axis parallel with the rolling plane normal. The β fibre starts at the brass orientation, goes through S and ends at the Copper orientation [30]. A visualisation of both fibers are illustrated in Figure 2.21.

23
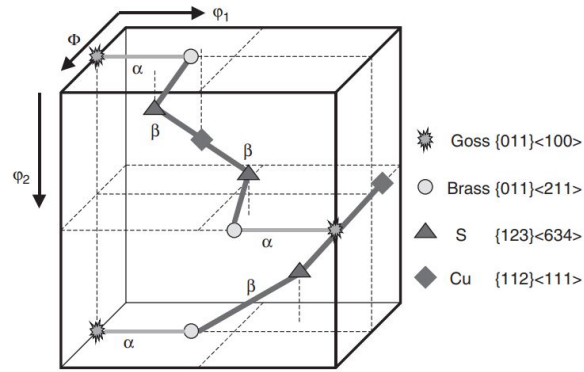
Figure 2.21: Schematic representation of cold rolling texture of fcc materials [30].

Common deformation texture components for fcc are given in Table 2.1, as given by Humphrey [7].

Table 2.1: Deformation texture components in fcc metals [7].

Component	{hkl}	<uvw>	φ_1	Φ	φ_2
Copper	112	111	90	35	45
S	123	643	59	37	63
Goss	011	100	0	45	90
Brass	011	211	35	45	89

An ODF of a 90% cold rolled aluminium is seen in Figure 2.22, with several orientations highlighted. In literature, sections for $\varphi_2 = (0, 45, 65)$ are commonly used to show the most important components.
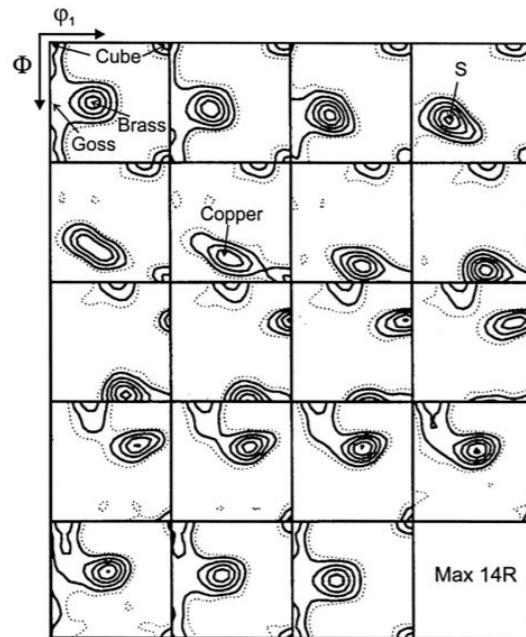
Figure 2.22: ODF of 90% cold-rolled aluminum with the positions of some important orientations indicated [7, 59].

2.6.2 Recrystallization Texture

Texture evolution during recrystallization in fcc metals are influenced by several components including the homogenization texture, percent cold deformation, grain growth overlap and purity of the metal. [30]. The most important recrystallization components in Al-alloys are presented in Table 2.2, as described by Humphreys [7].

Table 2.2: Recrystallization texture components in fcc metals [7].

Component	{hkl}	<uvw>	φ_1	Φ	φ_2
Cube	001	100	0	0	0
	236	385	79	31	33
Goss	011	100	0	45	0
S	123	643	59	37	63
P	011	122	70	45	0
Q	013	231	58	18	0
P	124	211	57	29	53

In Al-alloy, all dominating recrystallization texture components except for the R component are found in the $\varphi_2=0°$ section of the ODF. The different texture components are highlighted and positioned in a ODF section for $\varphi_2=0°$ is illustrated in Figure 2.23 and further presented below.

25
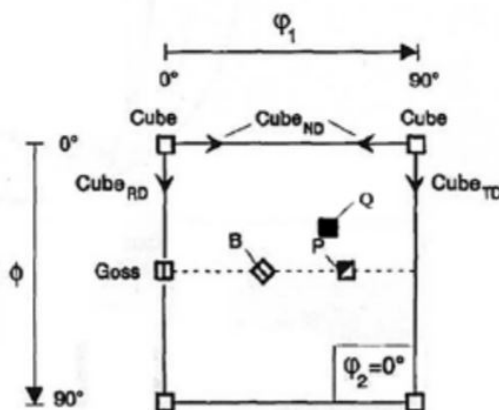
Figure 2.23: Position of different texture components of the $\varphi_2=0°$ -section of an ODF [9].

Cube

The origin of Cube texture ({001}<100>) is still unclear. Dillmore and Katoh [60] suggested that Cube nuclei existed in the deformed state as transition bands, separating volumes of major rolling components. The orientation gradient in the band would give the Cube component a growth advantage. The decrease in Cube texture during deformation is assumed to be related to the metastable Cube orientation as it rotates around RD towards the Goss-orientation. Another explanation is the increased stored energy form large deformation, which leads to an increase in amount of nucleation sites competing with the Cube nucleus, such as PSN-sites [9, 10].

It has been reported that cube has an approximate 40 °<111> relationship to the S-component and from each S-variant, there is one 40°-rotation that yields the Cube texture. The 40° relationship to the S component could explain the high intensity of Cube after recrystallization [9]. The 40°<111> boundary have higher mobility than random boundaries combined with high volume fraction of S-orientated grain after plastic deformation [7, 61]. Further, several studies have reported Cube grains growing into adjacent deformed S-oriented grains [62–64].

ND-rotated Cube

ND-rotated cube has a 40° <111> rotation of the Copper-orientation. A previous work has reported that ND-rotated Cube has a growth rate advantage at concurrent precipitation due to shorter incubation time compared to other orientations [61]. Tangen et al. [65] observed strong ND-rotated Cube with concurrent precipitation during annealing. Sjølstad [9] reported that PSN played a significant role in nucleation of both P and ND-rotated Cube texture component and that P and ND-rotated Cube had a growth advantage in the early stages of annealing.

P-texture

P-texture also has a 40 degree <111> rotation to the Copper-orientation, and has been termed the ND-rotated Goss texture. Strong P and ND-rotated Cube are observed in the case of concurrent precipitation of Mn-rich dispersoids in Al-Mn alloys [10, 65]. Nucleation of P

component has been shown to preferably occur in the deformation zone around large constituent particles [66]. Tangen et al. [10] observed a preferred nucleation in deformation zones and found that P-texture acts as an indication of PSN. The intensities of the P and ND-rotated Cube texture increase with cold rolled strain, supersaturation of Mn and dispersoid density while the intensities are reduced with annealing temperature.

Goss

The Goss orientation is usually present as a minor component in the deformation texture and a pronounced amount of Goss orientation in the recrystallized texture leads to poor formability. The Goss orientation is the favoured texture formation in transition bands [10].

Q-texture

Q-texture is often observed together with P-texture in the case of inhomogeneous deformation, due to the presence of particles or from the formation of shearbands [10].

2.7 Strengthening Mechanisms

As the material is deformed, dislocations will glide in response to the applied shear stress on a defined crystallographic plane in a defined crystallographic direction. The resolved shear stress on a slip system for a tensile test of a single crystal is given by [57]:

$$\tau = \sigma \cos \phi \cdot \cos \lambda \tag{2.17}$$

where σ is the normal stress acting on the slip plane, ϕ is the angle between the direction of σ and the normal to the slip plane, λ is angle between the σ and the slip direction. $\cos \phi \cdot \cos \lambda$ is referred to as the Schmid factor m. Slip occurs when the shear stress reaches a critical value τ_R (termed critical resolved shear stress) on the slip system with the highest Schmid factor [57]. The highest possible Schmid factor, m=0.5, corresponds to λ=ϕ=45°. The critical resolved shear stress is related to the yielding for a tensile test of a single crystal as seen in Equation 2.18.

$$\sigma_y = \frac{\tau_R}{m} \tag{2.18}$$

where σ_y is the yield strength. For a polycrystal, the Taylor factor M is utilized to relate the critical resolved shear stress to the yield strength given as

$$\sigma_y = \tau_R \cdot M \tag{2.19}$$

The Taylor factor accounts for the texture in the polycrystal. For a fcc metal with a with random distribution of the grain orientations, a Taylor factor equal to 3.1 is used [57].

2.7.1 Work Hardening

The work hardening behaviour of materials is often displayed through a stress-strain curve, which is usually divided into four stages, as illustrated in Figure 2.24 for a tensile test of a single crystal.
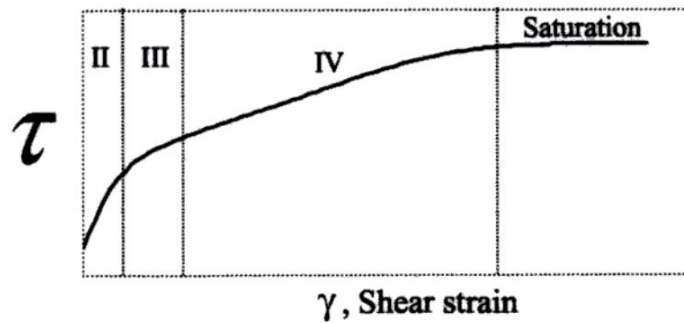
Figure 2.24: Schematic illustration of the stress-strain curve with the different stages indicated [29].

Stage I consist of easy glide, where dislocations are able to move over a relatively large distance without encountering obstacles. During easy glide, slip only occurs at one slip system and is therefore not seen in polycrystals. Stage II is related to the storage of dislocations and are independent of temperature. Multislip occur as several slip systems are activated simultaneously and are seen as a nearly linear part of the curve where the strain hardening increases rapidly. Intersecting dislocations which limits mobility are the largest contribution to increased hardening. Further hindering is caused by microstructural obstacles such as precipitates, grain boundaries, dislocations and solute atoms. At stage II, the dislocation density correlates to the resolved shear stress according [57]:

$$\tau = \tau_0 + \alpha G b \rho^{\frac{1}{2}} \tag{2.20}$$

Where α is a correction factor, G is the shear modulus, b is the Burgers vector, τ_0 is the shear stress and ρ is the dislocation density [57]. Stage III is a region where the rate of strain hardening decreases. Dynamic recovery start due to cross slip, climb and annihilation of dislocation and is therefore temperature dependent [30]. Stage IV is distinguished with a linear hardening rate [67].

The work hardening rate is often plotted in a Kocks Mecking plot, as illustrated in Figure 2.25. Stage I is associated with very low work hardening followed by rapid increase at stage II. Stage

III exhibits a linear reduction in the work hardening rate with increasing stress. At larger strains, stage IV is observed where the rate stagnates and slowly reduces with strain. The mechanisms for the hardening rate at stage I and stage II are single slip and initiation of multislip, respectively. Stage III consist of annihilation of stored dislocations while the mechanisms at stage IV is still unclear [68]. For polycrystalline material, stage I and stage II are not observed. Stage I is not present as deformation in a polycrystal only occur by multislip while stage II is not seen as the process of annihilation occurs at the onset of deformation which diminishes the extent of the stage. The latter is especially seen for metals with high stacking fault energy [67, 68].
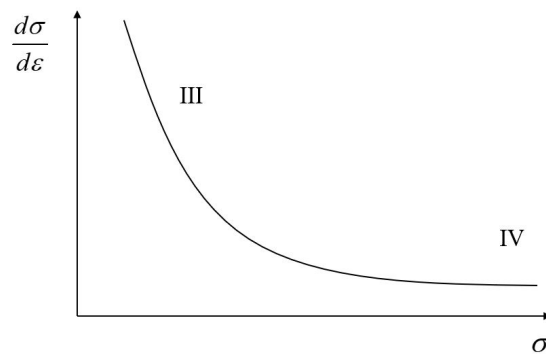
Figure 2.25: Schematic sketch of the strain hardening rate as a function of stress for a polycrystalline material.

2.7.2   Solid Solution and Cluster Strengthening

Solid solution strengthening is the result of interactions between dislocations and solutes. Depending on the size of the alloying element, strengthening can occur either interstitial or substitutional. Solute atoms that are smaller than the solvent will fill interstitial vacancies while the solute atoms of similar size as the solvent atoms can occupy a vacant point in the lattice. Substitutional strengthening is the solid solution strengthening mechanism in aluminium alloys, where additions of Mn, Mg and Cu are common contributors to strengthening. The interaction between the solutes and dislocations are caused by the strain field which arises due to the size misfit or by the different bonding around the solute which creates hard or soft spots in the lattice, known as modulus misfit. Both types of misfit result in elastic interactions with mobile dislocations where an additional stress is required for the dislocation to bypass the solute [57].

The dislocation solute interaction are further divided into two groups [69]: i) Stationary solute atoms act on moving dislocation (dislocation friction) and ii) Solute atoms collect at dislocation at rest (dislocation locking). The distribution of solutes and how the dislocation intersect with the solute will determine the hardening contribution. Interactions for dilute, strong point defects are treated by Feischer-Friedel theory where the obstacles are touched by the dislocation at a

full interaction force. Concentrated solutions with weak obstacles are treated by Mott-Labusch, where the dislocation touches the obstacles at the entrance side and the exit side, creating forces in the forward and backward directions [15, 70].

2.7.3 Precipitation Hardening

Hardening from particles will depend on the nature of the particle (size, strength, coherency) and the strengthening mechanism are therefore divided into whether a particle is shearable or non-shearable. As a dislocation meet a weak or coherent precipitate, the dislocation will be able to shear the precipitate. The cutting of a precipitate requires a higher stress compared to the requires stress to move in the matrix phase, thus leading to increased strength as dislocation movement is restrained. The increase in required stress can arise from several mechanisms. In coherent precipitates, dislocation motion is restrained due to a coherency strain field which formed due to a lattice mismatch between the matrix and the precipitate. Stacking fault strengthening occurs as a result of the difference in stacking fault between the matrix and the precipitates. Chemical hardening is related to the energy required to form a new surface between the precipitate and the matrix while order strengthening is the formation of anti-phase boundary as the upper and lower part of the precipitation are shifted relative to each other [57].

Incoherent particles can not be sheared, and the dislocation must bow out between the particles as illustrated in Figure 2.26. As the dislocation line reaches a critical curvature, the dislocation will bypass by bowing around the particle and leave a loop.
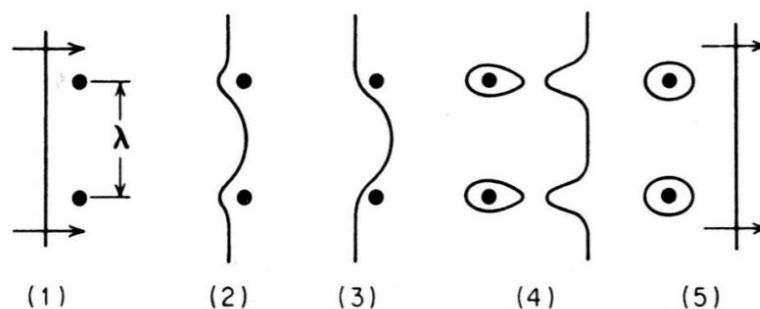

Figure 2.26: Schematic drawing of a dislocation passing non shearable particles [57].

The build-up of dislocation loops exerts a back stress on the particle and an increased stress is required for further dislocation movement. Non shearable particle with loops will cause the matrix to strain harden rapidly [57]. The strength required to force a dislocation between the

obstacle is known as the Orowan equation and is given by [57]:

$$\tau = \frac{Gb}{\lambda} \tag{2.21}$$

Where G is shear modulus, b is the burger vector and λ is the distance between the particles. The interparticle spacing can be expressed as a function of the particle size and the volume fraction f as:

$$\lambda = \frac{4(1-f)r}{3f} \tag{2.22}$$

where r is particle radius.

The Orowan equation has in later years been modified, as refined estimates of the dislocation line tension and correction for the interaction between the dislocation segment on either side of the particle have been introduced [57]. The most used modification is the Orowan-Ashby equation, given by [71]:

$$\sigma = \frac{0.84Gb}{2\pi(1-v)^{1/2}\lambda} \ln \frac{r}{b} \tag{2.23}$$

where v is the Poisson's ratio, r is the radius and M is the Taylor factor.

2.7.4   Grain Boundary Strengthening

The grain size will affect the mechanical properties of the material as well. Grain boundaries act as barrier against dislocation movement and will also distributes the slip between several grains. A fine grained material is stronger than a coarse grained material, as it has a larger total grain boundary area to hinder dislocation movement [72]. Hall-Petch is used to describe the relationship between yield strength and grain size, given by [57]:

$$\sigma_i = \sigma_o + k\frac{1}{\sqrt{D}} \tag{2.24}$$

where D is the grain size, σ_o is the lattice friction and k is a material constant.

2.8   The Stress-Strain Curve

The tensile test is used to study the deformation behaviour of materials. As a continuous increasing uniaxial load is applied on a tensile specimen, the material becomes elongated until fracture. The typical stress-strain relationship is illustrated in Figure 2.27.
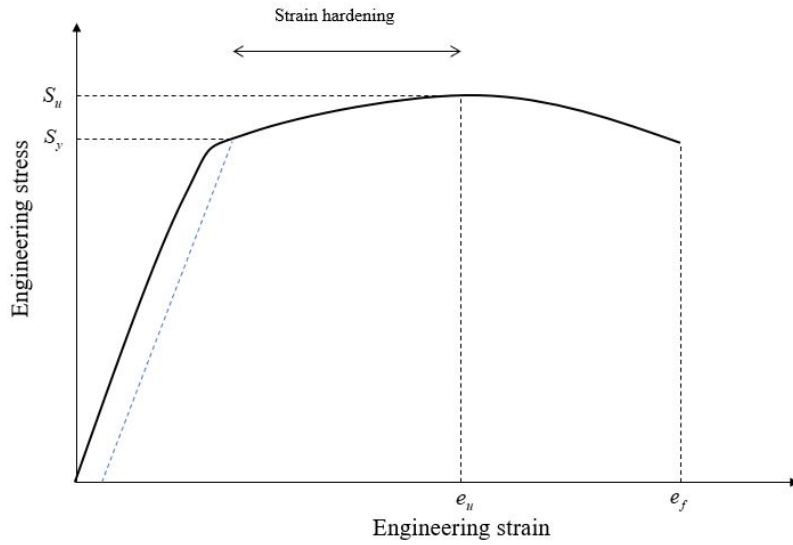
Figure 2.27: Schematic illustration of a engineering stress-strain curve.

The material transitions from elastic to plastic deformation as the stress is no longer proportional to strain. As it is often difficult to measure the exact stress where yielding or plastic deformation occur, the offset yield stress is used. The offset yield stress, $R_{p0.2}$, is the stress needed to induce a 0.2% plastic strain. When plastic deformation occurs, the dislocation density increases, causing the necessary stress for further deformation increases, which is known as strain hardening. The necessary stress increases until a maximum stress level is reached where the onset of necking occurs. The maximum stress level is referred to as the ultimate tensile strength, S_u and the corresponding strain in termed uniform elongation e_u. Fracture occurs at fracture strain e_f which is also known as total elongation [72].

The engineering stress S and strain e is defined as:

$$S = \frac{P}{A_0} \tag{2.25}$$

$$e = \frac{l_i - l_0}{l_0} \tag{2.26}$$

where P is the applied load, A_0 is the initial cross section area. The original length of the specimen is given as l_0 and l_i is the instantaneous length. True stress and strain take into account the change in cross section area, A_i, upon deformation and is expressed as:

$$\sigma = \frac{P}{A_i} \tag{2.27}$$

$$\epsilon = \ln \frac{l_i}{l_0} \tag{2.28}$$

The engineering stress and strain can be converted into true stress and strain by the following equations:

$$\sigma = S\left(1 + e\right) \tag{2.29}$$

$$\epsilon = \ln\left(1 + e\right) \tag{2.30}$$

2.9   Anisotropy

As a result of plastic deformation, metals often exhibit directional dependent properties, known as anisotropy. For a rolled sheet, mechanical properties such as elastic modulus, yield stress, ductility and ultimate tensile stress in the sheet plane will vary with the direction relative to the rolling direction [20]. Anisotropy arises mainly because of texture, however grain shape, precipitates and dislocation structures may influence as well.

The plastic strain ratio (r-value) is utilized as a measure of the anisotropy in a material and is given as [73]:

$$r = \frac{\epsilon_w^p}{\epsilon_t^p} \tag{2.31}$$

where are ϵ_w^p and ϵ_t^p is the plastic strain width and thickness, respectively. An anisotropic behaviour corresponds to different contraction rate in width and thickness, causing the r value to deviate from 1 [74]. A material with high r-value corresponds to a high resistance towards thinning and will only get narrower, while a small r-value corresponds to rapid thinning. For rolled aluminium sheets, the material can have a lower resistance towards thinning in the rolling direction compared to the transverse direction as the r-value is higher in the latter one [75, 76]. As it is difficult to measure the thickness of thin sheets, the r-value is commonly found by using longitudinal and width plastic strain.

By assuming volume preservation, the r-value can be expressed as [77]:

$$r = \frac{\epsilon_w^p}{-\left(\epsilon_w^p + \epsilon_l^p\right)}$$ (2.32)

Where ϵ_l^p is the plastic longitudinal strain. The plastic strains are found using the following equations:

$$\epsilon_l^p = \epsilon_l - \epsilon_l^e = \epsilon_l - \frac{\sigma}{E}$$ (2.33)

$$\epsilon_w^p = \epsilon_w + \epsilon_w^e = \epsilon_w + v\frac{\sigma}{E}$$ (2.34)

where ϵ_l and ϵ_w is the total longitudinal and width strain, respectively, v is the Poisson's ratio and E is the E-modulus.

2.10   Strain Path Changes

Abrupt changes in strain path during deformation tend to cause the mechanical behaviour to change from those seen with monotonic loading. Effects of a strain path change are associated with a transient stress response on the stress-strain curve, seen either as an increase or lowering of the yield strength caused by an orthogonal or reverse reloading. Alloys with a high stacking fault energy are especially susceptible towards strain path changes, where aluminium alloys have been subjected to thorough investigations [78, 79]. Less pronounce effect has been observed in metals with lower stacking fault energy [80, 81].

The influence of an abrupt strain path change can be quantified by the parameter ϕ from the following equation:

$$\cos\phi = \frac{\mathbf{D}_1 : \mathbf{D}_2}{\|\mathbf{D}_1\| \cdot \|\mathbf{D}_2\|}$$ (2.35)

Where $\mathbf{D}_1$ is the strain rate tensor under prestrain, $\mathbf{D}_2$ is the subsequent strain rate tensor and ϕ is the angle between the tensors, referred to as the Schmitt angle [82]. Monotonic loading is represented by $\cos\phi$=1, while orthogonal and reverse strain path change is represented by $\cos\phi$=0 and $\cos\phi$=-1, respectively. A $\cos\phi$ value close to 1, -1 or 0, are termed pseudo-monotonic, pseudo-reverse and pseudo-orthogonal, respectively.

In literature, most experiments on strain path changes are preformed using two step tests. First, deformation is applied to a large sample before a smaller sample is cut out at an angle α to the

prestrain direction. The strain rate tensor for a two step tensile test can be expressed as [83]:

$$\mathbf{D}(\alpha) = \begin{pmatrix} 1 + (1 + 2r)\cos(2\alpha) & (1 + 2r)\cos(2\alpha) & 0 \\ (1 + 2r)\cos(2\alpha) & 1 - (1 + 2r)\cos(2\alpha) & 0 \\ 0 & 0 & -2 \end{pmatrix} \frac{\sqrt{3}\dot{\epsilon}_{vM}}{4\sqrt{r^2 + r + 1}} \qquad (2.36)$$

where $\dot{\epsilon}_{vM} = \sqrt{\frac{2}{3}\mathbf{D}:\mathbf{D}}$ is the Von Mises effective plastic strain rate and r is the r-values for the strain directions. The Schmitt angle, according to Equation 2.35, for a two step test with a sequence of rolling ($r_1 = 0$) and uniaxial tension can be calculated as:

$$\phi = \cos^{-1}\left(\frac{3 + (1 + 2r_2)\cos(2\alpha)}{4\sqrt{r_2^2 + r_2 + 1}}\right) \qquad (2.37)$$

where r_2 is the r-value for the tensile strain and α is the angle between the strain directions. For a sequence of two step tensile test, the Schmitt angle is given as:

$$\phi = \cos^{-1}\left(\frac{3 + (1 + 2r_1)(1 + 2r_2)\cos(2\alpha)}{4\sqrt{r_1^2 + r_1 + 1}\sqrt{r_2^2 + r_2 + 1}}\right) \qquad (2.38)$$

where r_1 and r_2 are the r-values for the two tensile straining direction.

2.10.1   The Mechanical Behaviour

As mentioned, there are two main types of observed effects after strain path changes. A reverse strain path change is associated with a decrease in yield strength after reloading and is referred to as the Bauschinger effect. The Bauschinger effect occurs when the material is loaded past the yield stress in one direction which causes a reduction in yield stress in the opposite direction [57]. In addition to a lower yield strength, a transient increase is seen on the work hardening rate. An orthogonal strain path change is associated with an increase in yield strength, referred to as cross hardening. The increase in yield is accompanied by a transient reduction of the work hardening rate followed by a resumption of work hardening. The softening can cause instability, especially after larger prestrains, leading to early strain localisation and necking [78]. In general, a larger prestrain results in a larger deviation from the monotonic yield stress level. In addition, permanent changes to the flow stress has been reported by several [78, 81]. The transient behaviour in work hardening after strain path changes is associated with a high initial hardening rate after reloading followed by a rapid decrease. The hardening rate reaches a minimum before it increases and approaches the monotonic hardening curve.

2.10.2 Mechanisms for Behaviour

The mechanisms behind the transient behaviour observed with strain path changes are still somewhat unclear. Several authors have concluded that the formation of cell walls is necessary for the transient behaviour to occur [78, 79, 84–86]. However, transient behaviour after strain path changes has been reported of where no evolution in the cellular dislocation structure was seen and it has been suggested that the transient response may be caused by interactions between dislocation interactions on the slip system level [87].

Many investigations have referred to the concept of an alien or unstable substructure upon a strain path change [78, 80, 88, 89]. Depending on the reloading, slip systems can either change or new slip systems activate, resulting in an unstable dislocation structure. The unstable dislocation structure is gradually replaced either by dissolution or reorganisation process into a stable structure under the new straining condition. The initial change in yield strength seen with a strain path change may be caused by the requirement of an activation stress which may be greater or lower than for a monotonic test [89].

Microbands have also been observed after orthogonal strain path changes. TEM investigations conducted by Rauch and Schmitt [90] on a low carbon steel after a cross test (tension-simple shear), showed microbands cutting through the pre-existing dislocation structure. The bands were parallel or normal to the shearing direction. It was further seen that the all shear deformation was mainly concentrated within the band. It is assumed that initial increase in yield strength seen upon an orthogonal strain path change is caused by the high stress required to form microbands. The following softening and localisation occur because of the low dislocation density, i.e. disappearance of the pre-existing substructure within the band [91]. While microbands are mainly seen mild steel [91], Lewandowska [92] reported of microbands in aluminium alloys (AA6016 and AA5182) after a 20% shear deformation. Gaspérini et al. [93] also observed strain localisation in terms of shear bands by preforming shear test on a 90% cold rolled AA3004 sheet.

Latent hardening may also explain the increase in yield strength seen with an orthogonal strain path change. A higher shear stress is needed to activate slip systems which were latent during prestraining, as the newly activated slip system must cut through the stored dislocations formed by the previous active slip systems.

Orowan [94] proposed that the lower yield strength seen with reversal reloading is the result cell formation. As the material is deformed in one direction, dislocations migrate into cell walls. During a load reversal, the dislocations can move at a lower shear stress because of the barrier to the rear of the dislocations are weaker compared to those in the front. However, Rauch [90] later investigated the influence of dislocation structure on reverse test and found that a material

with a homogeneous dislocation distribution had a 10% lower yield stress upon a reloading than the same material with a cell structure. Rauch concluded that the concentration of dislocations drives the Bauschinger effect, and not the cellular structure. In addition, Vince et al. [95] compared the structural evolution in low carbon steel and a commercial pure aluminium upon a load reversal at low temperatures. While the aluminium alloy had formed a cell structure after prestraining, no heterogeneous dislocation distribution was formed in the steel. However, a Bauschinger effect and stress plateau was observed for both alloys. It was suggested that the structural features like cell dissolution are not responsible for the effect, but merely a correlated to the observed transient stagnation of the hardening rate. The authors concluded that the mechanical behaviour is controlled by individual interactions between moving dislocations and the obstacles lying on their slip plane.

3   Literature Review

In this section, an overview is given on previous investigations and proposed theories relevant to evolution in mechanical behaviour for the 3xxx alloy during the lacquering process. For this thesis, the short heat exposure related to the drying of the lacquer and strain path changes has been examined. The literature review starts with research conducted on the typical annealing behaviour in 3xxx aluminium alloys at low temperatures and the influence of deformation strain, amount of alloying elements in solid solution and dispersoids. Higher strains promote both softening and concurrent precipitation while higher amount of alloying elements retard softening. Dispersoids can retard softening and are observed as stable at low annealing temperatures. Furthermore, a review on the influence of dispersoids on strengthening through the Orowan bowing mechanism is given and their influence of work hardening. Recent investigations on the precipitation of metastable Mg_2Si in 3xxx is then presented followed by a review on the hardening on annealing phenomenon observed in early stages of low temperature annealing of non-heat treatable alloys and its dependency on strain level and supersaturation. Investigations on mechanisms causing hardening by strain path changes in aluminium alloys are then reviewed, where the objective is the influence of the dislocation structure and anisotropy. Last, a summary of the obtained results from the work conducted by the author during the specialization project, including a characterization of a AA3005 alloy with the same deformation degree and temper as the investigate alloy and results from flash annealing experiments. This work is included as the access to laboratories were restricted due to COVID-19.

3.1   Softening and Concurrent Precipitation

In 2003, Somerday and Humphrey [47] investigated the behaviour of concurrent precipitation in a supersaturated Al-1.3Mn alloy at low annealing temperatures. Prior to annealing, the alloy had a rolling reduction of 90% with typical rolling structure, consisting of large elongated grains and subgrains which were slightly elongated in rolling direction.

After 1 hour of annealing at 350°C, subgrains were slightly larger than before annealing, however, they were still elongated and only a minor increase in mean misorientation were observed (from 5° to 6°). It was observed a large fraction of dispersoids on high angle grain boundaries (misorientation above 15°) compared to medium and lower grain boundaries, suggesting that while HAGB is sufficiently pinned, subgrain growth is still possible. As annealing continued, precipitation began on lower misoriented boundaries, as seen from Figure 3.1. The dashed horizontal lines represent equal probability of random precipitation. Medium angle grain boundaries (MAGBs) were defined as 10-15° misorientation while low angle grain boundaries were defined as below 10°. A probability above or below this level indicate more or

less precipitation than expected, respectively.
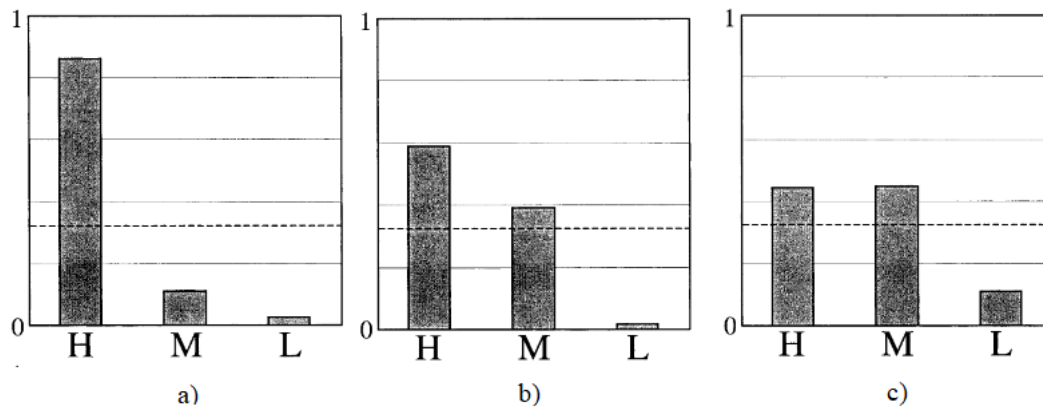
Figure 3.1: Probability of precipitation at high (H), medium (M),and low (L) angle boundaries in Al-1.3Mn after annealing at 350°C for a) 1h b) 4h c) 24h [47].

With longer annealing time, the precipitation occurred at less misorientated grain boundaries as well. After 24 hours, the precipitation occurred with the same frequency at HAGBs and MAGBs while the frequency was lower at LAGBs. As precipitation had occurred prior to the onset of recrystallization, recrystallization would be prevented as both high and low angle boundaries were sufficiently pinned by the dispersoids.

In 2003 Sjølstad [9] investigated the annealing behaviour of a 3013 alloy (Al-0.57Fe-0.12Si-1Mn and other elements <0.02%wt). Prior to annealing, three different homogenization treatments were conducted to investigate the influence of Mn in solid solution. The material was further cold rolled to strains of ϵ=0.5, 1.5 and 3 to investigate the influence of strain. Annealing was conducted in the temperature range of 250-500°C and the annealing behaviour was followed by conducting hardness and electrical conductivity measurements. The softening curves and the electrical conductivity measurements for the material with a strain of 3 and 1.5 is seen in Figure 3.2 and Figure 3.3.

Figure 3.2: Softening and conductivity curves of AA3103 deformed to a strain of 3 for three different levels of Mn solid solution a) high b) medium c) low [9].
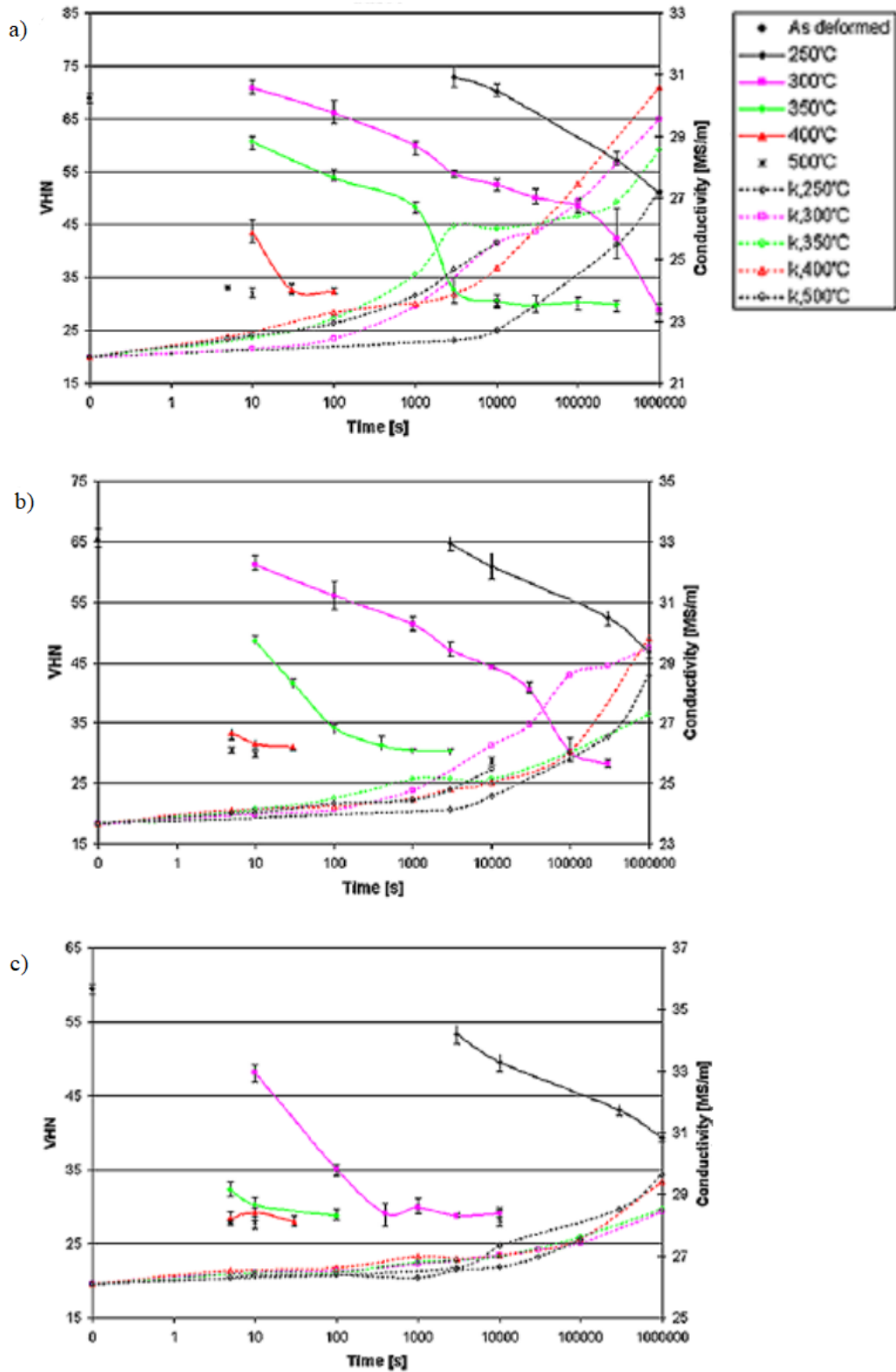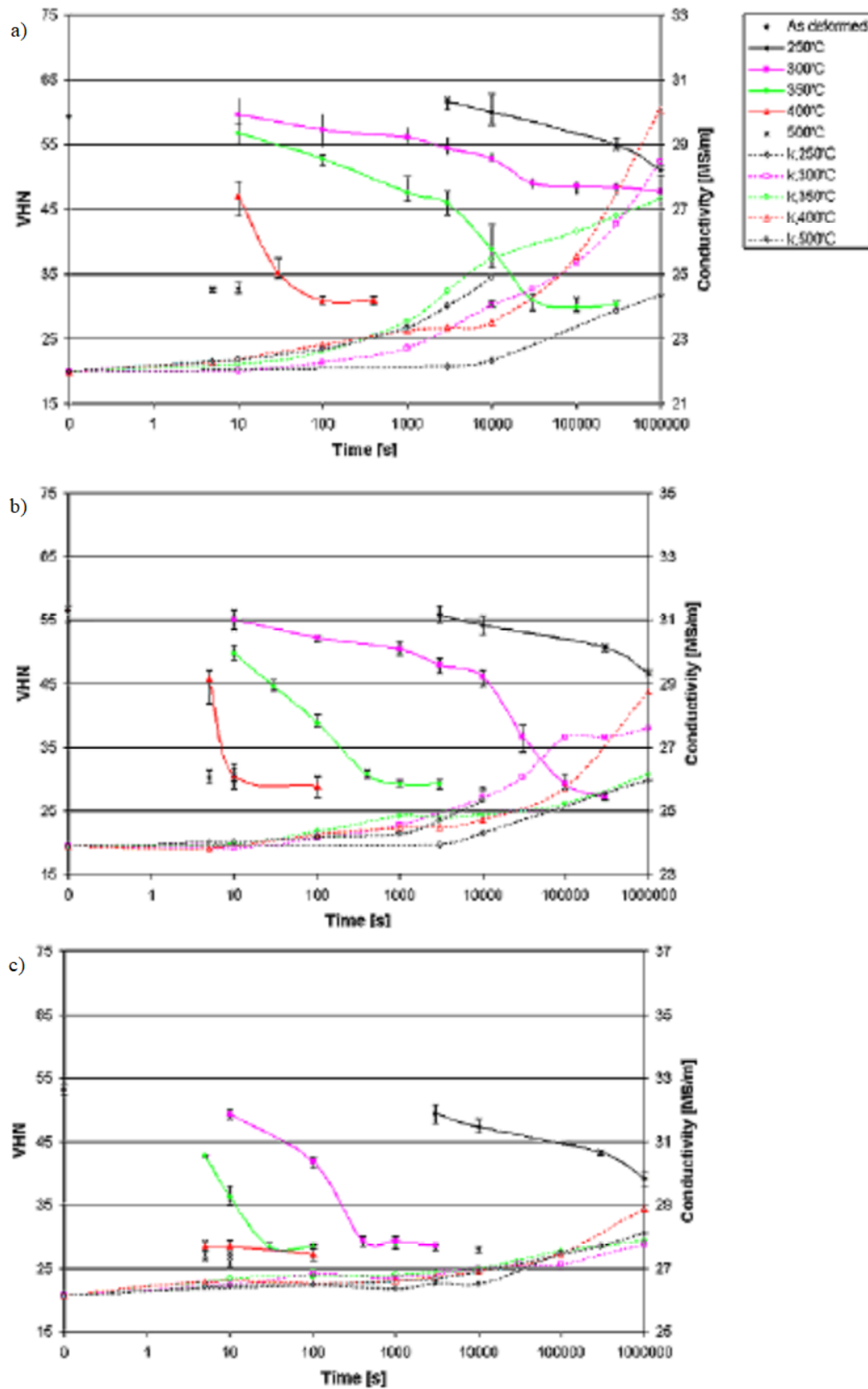
Figure 3.3: Softening and conductivity curves of AA3103 deformed to a strain of 1.5 for three different levels of Mn solid solution a) high b) medium c) low [9].

It was reported that at the lowest annealing temperature (250°C), none of the samples had recrystallized withing the 11 days of annealing. Sjølstad further observed that while concurrent precipitation had an influence on softening, the effect was small compared to the total drop in hardness during annealing. However, higher amounts of alloying elements in solid solution did slow the softening reactions down. At the lowest temperatures, the softening was completely stopped.

It was further seen for lower annealing temperatures, that as softening was retarded, the conductivity increased, indicating concurrent precipitation. As the amount of Mn in solid solution increased, precipitation occurred more rapidly. In the sample with the highest level of Mn, precipitation occurred within minutes at 350°C. The author attributed this to migration of Mn through grain boundaries into clusters formed during deformation which precipitated upon annealing, as diffusion of Mn is too slow during low annealing temperatures. This was confirmed by SEM investigations, where the dislocation density was nearly constant upon annealing, i.e. there were no formation of dispersoids after an initial stage of annealing, only growth. On the strain dependency, the author reported that higher strains promoted both recrystallization and precipitation. It was suggested that concurrent precipitation only occurs at lower temperatures due to the mobility of the grain boundaries. As the mobility increased with increasing temperature, the mobility becomes too high for solute atoms to migrate toward dispersoids and will stay in solid solution as clusters.

In 2010, TTT-diagrams were published by Tangen et al. [65] on the same alloy. In addition to the three homogenized samples, an as cast variant was investigated as well to observe the influence on annealing of a supersaturated solid solution (Mn_{ss}=0.72wt%). A 25% softening was defined as the onset for recrystallization and 2.5% increase in conductivity was defined as the start of precipitation. The authors defined a critical temperature T_c, which indicated the temperature where the precipitation curve crosses the curve indicating the start of recrystallization.
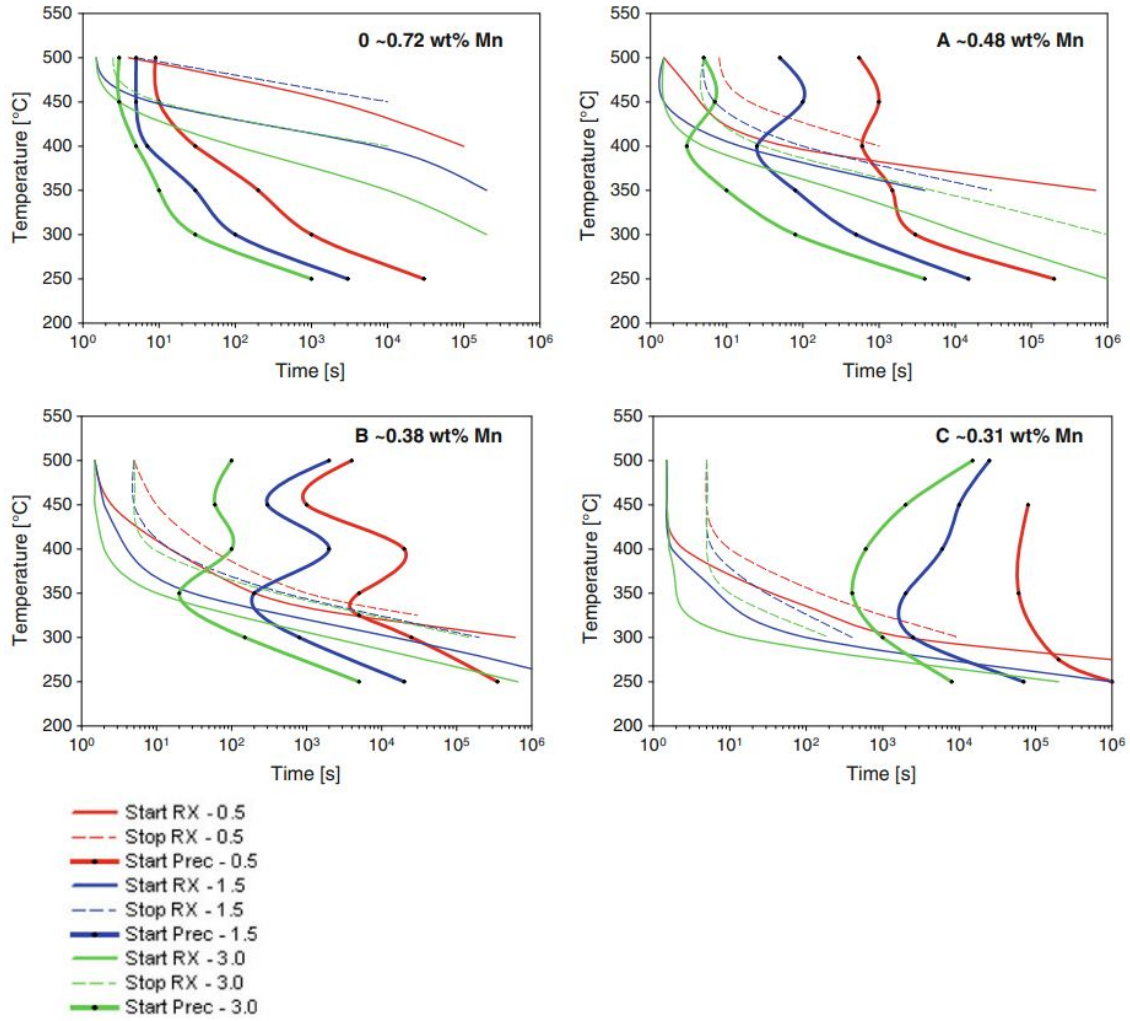
Figure 3.4: TTT diagrams for the AA3013 alloy. The onset of the precipitation reaction is indicated by thick solid lines, while start and finished recrystallization are indicated by thin solid and broken lines respectively [65].

The authors observed that increasing strain both lead to a larger driving pressure for recrystallization and increased driving pressure for precipitation of Mn-bearing dispersoids. This was attributed to a larger amount of stored deformation energy and higher density of microstructural heterogeneities available for nucleation of recrystallization and dispersoids. It was further reported that the temperature where precipitation occurred most rapidly, i.e.the precipitation nose in the TTT-diagram, shifted toward shorter times and higher temperatures with increasing concentration of Mn_{ss}.

Upon early stages of annealing, dispersoids were observed to precipitate on HAGBs, defined as a grain boundary with a misorientation higher than 10°, as seen from the BSE image in Figure 3.5. With further annealing, dispersoids precipitated on lower misorientated grain boundaries as well. The solute rich zone seen at the high angle grain boundary in the Figure 3.5 were suggested to be precursors to dispersoids on grain boundaries. The authors concluded that the both the

solute zones and dispersoids would retard softening and HAGBs would therefore experience the strongest Zener drag during annealing as they contained the highest concentration accumulated alloying elements and had a high number of precipitates.
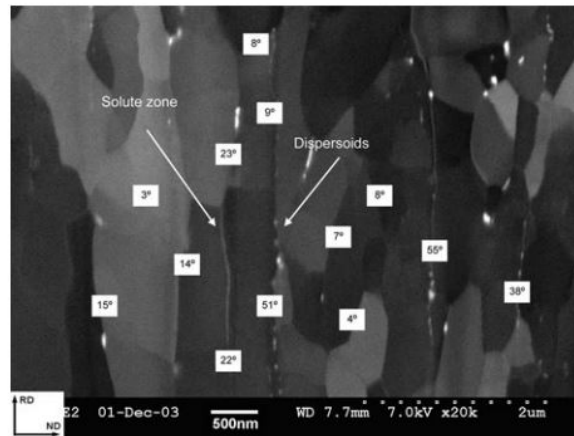
Figure 3.5: Micrograph showing dispersoids and solute zones after annealing at 350°C at 10^3s. The numbered text boxes represent the misorientation [65].

Below the temperature T_c, the recrystallization grain structure was elongated and coarse with a characteristic pancake shape due to a large Zener drag from the dispersoids precipitated along RD/TD plane. The grain size increased with increasing strain and higher initial concentration of Mn in solid solution. The variant with the high supersaturation is seen in Figure 3.6. Above T_c, the microstructure was unaffected of concurrent precipitation. The author concluded that above T_c, recrystallization was not affected by concurrent precipitation.
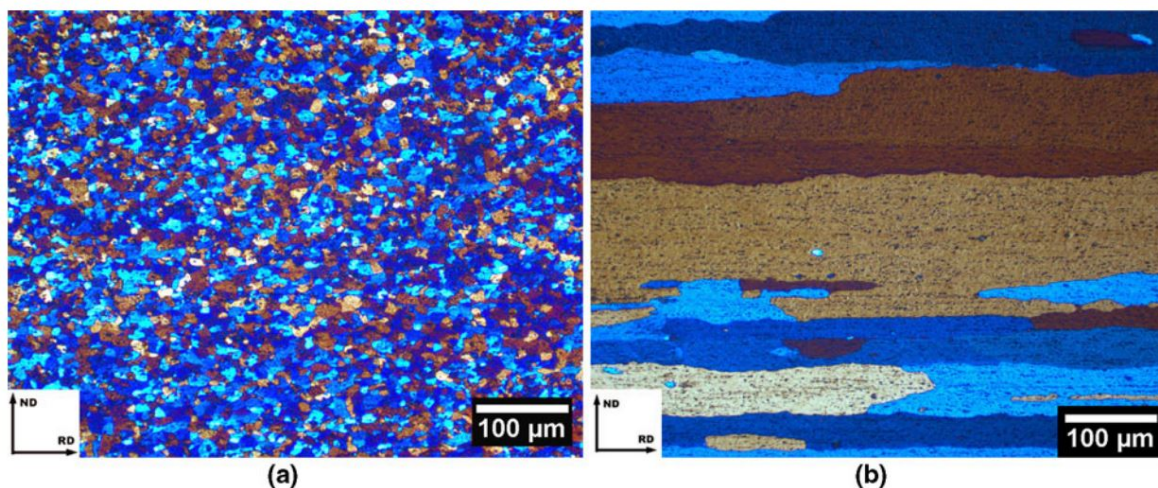
Figure 3.6: Recrystallized grain structures for the as-cast material variant (0.72 wt pct Mn_{ss}) cold rolled to a true strain of 3.0 and isothermal annealed at a temperature of (a) above T_c and (b) below T_c [65].

It was found from texture measurements that P and a weaker ND-rotated Cube components dominated in samples affected by concurrent precipitation, where the larger strain increased the

intensity of both components. This was attributed to an initial growth advantage compared to PSN sites due to their 40° ⟨111⟩ relationship to the copper component. The boundaries between PSN sited was assumed to be highly perfect boundaries. These boundaries are less affected by solute segregation and precipitation, resulting in an early growth advantage compared to other boundaries and therefore increasing the intensity of P and a weaker ND-rotated cube.

The influence on softening from a randomly distribution of dispersoids was investigated by Tangen [10] in 2004. The investigation was conducted on a cold rolled AA3103 alloy with a composition of 0.58 wt%Fe, 1 wt%Mn and 0.1wt% Si in balance with Al. Subsequent to annealing, various heat treatments and cold rolling reductions were conducted to obtain a wide range of distributions of Mn-bearing dispersoids. To isolate the influence of pre-existing dispersoids from concurrent precipitation, a two-step deformation process was conducted which randomized the dispersoid distribution. Annealing was conducted between 250 to 500°C for various amount of times to study the softening and precipitation behaviour.

Based on softening curves, the author reported that the dispersoid density controlled the softening kinetics. Softening was significantly slower in samples with higher number densities, which were attributed to a strong Zener drag. It was further observed that a smaller dispersoid size and a lower driving pressure for softening enhanced the Zener drag.

The influence of a heterogeneous distribution of dispersoids was investigated by Huang et al. [96] in a Al-0.39Mn-0.53Fe-0.152Si alloy in 2015. Prior to annealing, the material was cold rolled to a strain of 3. Various annealing programs were conducted to investigate influence of concurrent precipitation and pre-existing dispersoids. The authors observed that at low annealing temperatures both pre-existing dispersoids and concurrent precipitation, resulted in a strong Zener pinning effect on subgrain and grain boundaries, resulting in elongated and coarse grain structure. Pre-existing dispersoids were seen to have a minor effect on texture compared to concurrent precipitation, as only a weak P component was detected. This was attributed to the larger size for the pre-existing dispersoids compared to those seen at concurrent precipitation.

3.2   Thermal Stability of Dispersoids at Low Temperatures

In 2012, Li et al. [97] studied the precipitation and growth of α-Al(Mn,Fe)Si dispersoids in a AA3003 alloy with 1.15 wt%Mn, 0.58 wt%Fe, 0.20 wt%Si and 0.08 wt%Cu during two heat treatments. The as casted material was first heated up to 500°C with a heating rate of 50°C h^{-1} followed by a immediate quenching into cold water. TEM investigations revield that after the first heat treatment, the dispersoids size were in the range of 50-200 nm with a block or plate shaped morphology with a partial coherency with the matrix. These results were further compared to the distribution and size of the dispersoid after a second heating, where the material

was heated up to either 375°C or 600°C with the same heating rate as the first heat treatment and were held for 24 hours. At 375°C, the authors reported of a large quantity of fine dispersoids. The mean diameter of the dispersoids were 43 nm and the volume fraction were 0.77% (density of $3.6\cdot10^20$ m^{-3}). As no size difference was detected, it was concluded by the authors that the dispersoids were thermally stable at low temperatures and that coarsening or growth of the dispersoid would be slow. This was attributed to the low diffusion rate of Mn and Fe in the alloy. It was further suggested that the partial coherent interface between the dispersoids and the matrix would hinder the growth of dispersoids as the interface has a low energy and low mobility. For the alloy annealed at 600°C, no dispersoid were found, which were attributed to dissolution of dispersoids and coarsening of larger constituent particles.

3.3   Influence of Mn-bearing Dispersoids on Strength and Work Hardening

Most investigated on 3xxx aluminium alloys have only considered the influence of Mn bearing dispersoids on softening through the Zener drag and not their strengthening effect. In recent years however, dispersoids have been found to have a hardening effect which is briefly reviewed in the following section.

Early investigations of dispersoids in copper crystals conducted by Ashby in 1966 showed that small volume fraction of dispersoids lead to parabolic work hardening at small strains compared to single crystals without dispersoids [98]. Humphrey and Hirsch [99, 100] further developed a theory of work hardening at low temperatures based on investigations of deformation in single crystals of copper and copper-zinc containing alumina particles. The theory of working hardening was developed based on glide dislocations generating rows of prismatic loops by cross slip at the particles the particles. The parabolic hardening was related to an increase in dislocation density due to prismatic loops. The model was deduced from electron microscope observations and were able to predict a parabolic work hardening curve above an initial region of low hardening at low temperatures.

The effect of dispersoids on the work hardening rate in 3xxx aluminium alloy were investigated by Forbord et al. [101] in 2000. By comparing the strength level in a AA3202 with and without dispersoids, it was found that dispersoids resulted in a higher work hardening rate at small strains (below 5%) while the opposite occurred at higher strains, leading to a lower maximum strength. As the amount of Mn in solid solution were different in the annealed sample and the recrystallized sample, at 0.1 and 0.2 at% respectively, the behaviour was seen as a combined effect of a higher amount dispersoids and a lower level of solid solution.

In 2012, Li et al. [97] studied the precipitation and growth of α-Al(Mn,Fe)Si dispersoids in a AA3003 alloy with 1.15 wt%Mn, 0.58 wt%Fe, 0.20 wt%Si and 0.08 wt%Cu during two heat
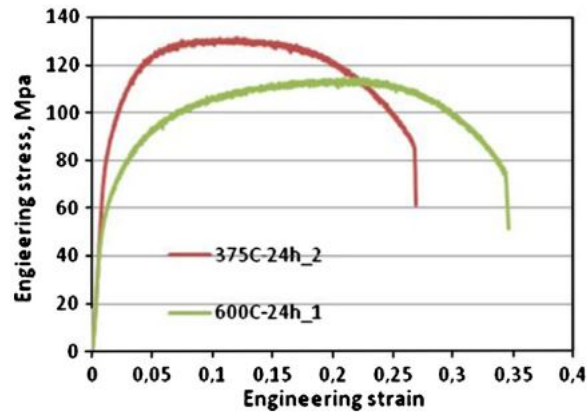
Figure 3.7: Stress–strain curve of the 3003 alloy, one specimen without dispersoids (600C 24h 1) and one specimen with dispersoids (375C 24h 2) [97].

treatments, either 375°C or 600°C, for 24 hours. The sample heated at 375°C contained dispersoids while the sample heated at 600°C did not contain dispersoids. Tensile tests were performed as seen in Figure 3.7. A significant increase in both yield and tensile stress were observed in the specimen containing dispersoids combined with a reduction in total elongation. Electrical conductivity measurements showed that both samples had a similar amount of Mn and Fe in solid solution which confirmed that the increase in strength was not associated with solid solution strengthening. The authors attributed the strength to the high density of fine dispersoids by correctly estimating the increasing yield by assume that the strengthening is the result of the Orowan bowing mechanism for by-passed particles and utilizing the Ashby-Orowan equation (cf. Equation 2.23).

The influence of dispersoids on work hardening was further investigated by Zhao et al. [102] in 2013 on an Al-0.97Mn-0.50Fe-0.15Si alloy. To isolate the influence from dispersoids, the solute level was controlled by different homogenization treatments. Four different homogenization treatments were conducted, leading to two different levels of solute and for each solute level, two different size and distributions of dispersoids. Samples denotes 'A' had high solute level, while samples denoted 'B' had a lower level. The dispersoid distribution for samples with a low level of solutes is given in Figure 3.8. As seen, the sample denoted 'BH' had a narrow distribution with a low mean diameter, while the sample denoted 'BL' had a broad distribution with a higher mean diameter.
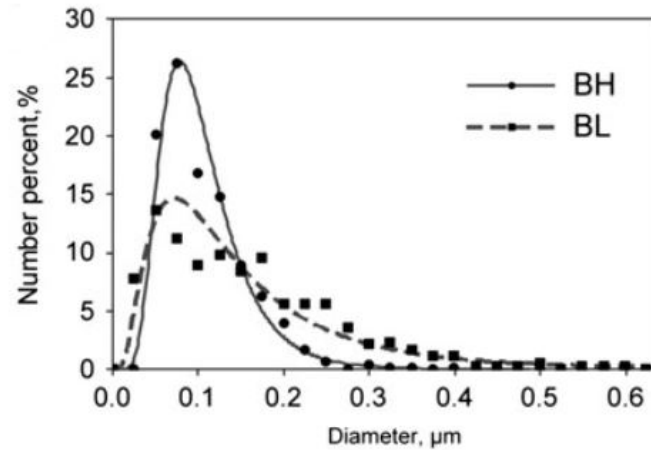
Figure 3.8: The size distribution of dispersoids in BH and BL in the Al-0.97Mn-0.50Fe-0.15Si alloy [102].

After a tensile strain of 16%, the influence from dispersoids on the dislocation structure was clearly detected by TEM imaging. As seen from Figure 3.9a, a narrow distribution and small dispersoid size resulted in a large amount of loose dislocation tangles around the dispersoid. It was further reported that the BH sample had a higher dislocation density and smaller cell size than the BL sample. The authors attributed the influence on the microstructure on the formation of dislocation loops, both Orowan loops formed around the particle and rows of prismatic loops in the vicinity of dispersoids. The extra loops formed would result in a higher dislocation density and further promote cell wall formation, leading to a reduced cell size. The influence on the microstructure from dispersoids during rolling was further investigated by conducting cold rolling on the homogenized samples. It was seen that the subgrain size decreased with increasing rolling strain and that the dispersoids were located at subgrain boundaries. The influence from dispersoids on the subgrain size diminished at large strains, which was attributed to the dispersoids spacing (dispersoid density). As the dispersoids spacing was reduced, the density of dislocation loops (GNDs) would increase, leading to a uniform dislocation distribution in the matrix. The reduced influence at higher strains was also attributed the influence of strain on subgrain size. At larger strain, the subgrain size is smaller than the dispersoids spacing, and the effect of dispersoids would therefore diminish.

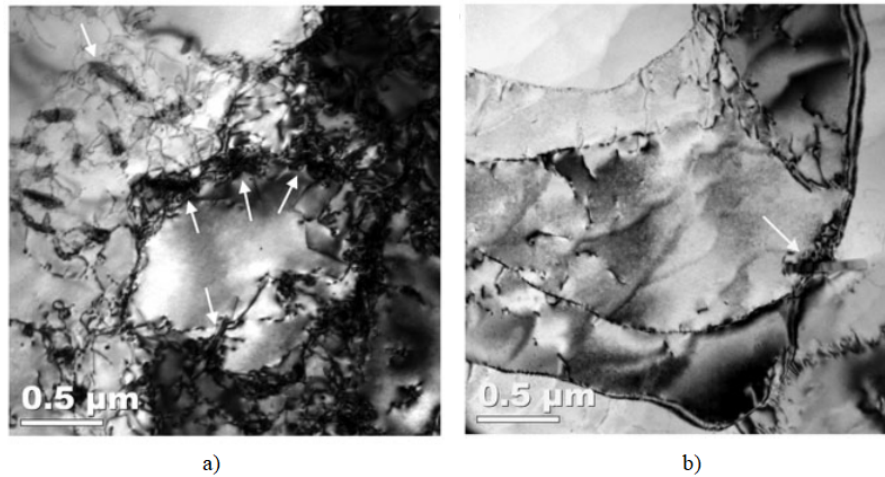**Figure 3.9:** TEM bright-field images of the cross-sections of Al-0.97Mn-0.50Fe-0.15Si alloy a) BH and b) BL at 16% tension strain. Cell walls formed by connecting dislocation networks around dispersoids (indicated by the arrows) [102].

Tensile testing and reverse strain path (Bauschinger) test were conducted to investigate the effect of the pileups of dislocation loops and the influence of internal stress on the work hardening. It was seen from the tensile test for the homogenized samples that the yield strength was higher for the BH sample than for the BL sample which the authors attributed to the high density of dispersoids resulting in a high work hardening rate in the initial deformation stage. Furthermore, it was seen that the flow stress converged at larger strain which indicated that the influence of dispersoids was reduced. A similar trend was seen for the AH and AL sample, however the differences between the samples was of a smaller magnitude and the flow stress converged at lower strains. From the reverse strain path test, it was observed that the internal stress increase rapidly at small strains where it contributed to 10-20% of the total work hardening. The contribution increased with a larger fraction of small dispersoids. The internal stress saturated at higher strains and it was therefore concluded that it did not contributed to the rate of work hardening. The strain dependency was attributed to the dispersoids spacing and subgrain size, as found from the microstructural investigation.

3.4   Precipitation of Metastable Mg_2Si in 3xxx Aluminium Alloys

While the addition of Mg in non-heat treatable alloys is used for solid solution strengthening, Mg in combination with Si has been observed to form metastable Mg_2Si precipitates in 3xxx alloys. These precipitates are typically found to precipitate in supersaturated Al-Mg-Si alloy. The stable Mg_2Si precipitate is denoted as β and is incoherent while the metastable phases are denoted as β'' and β', both semi-coherent and contributes to strengthening in Al-Mg-Si alloys [4].

In 2000 Lodgaard and Ryum [103] investigated the precipitation sequence of Mn bearing dispersoids Al-Mg-Si alloys during continuous heating from room temperature. It was observed during heating at 100-350°C that the β' precipitates nucleated homogeneously and grew with increasing temperature due to supersaturation of Mg and Si on the alloy. Above 350°C, an intermediate phase termed u-phase, formed heterogeneously on the dissolving β' precipitates, which contained higher amounts of Mg, Si, Mn and Fe. As the temperature increased above 400°C, α dispersoids heterogeneously nucleated on the u-phase precipitates and further consumed the it. It was seen that several α-dispersoids had precipitated on a single u-phase, resulting in a chain of α-dispersoids as seen in Figure 3.10a. The precipitation sequence is schematically illustrated in Figure 3.10b.
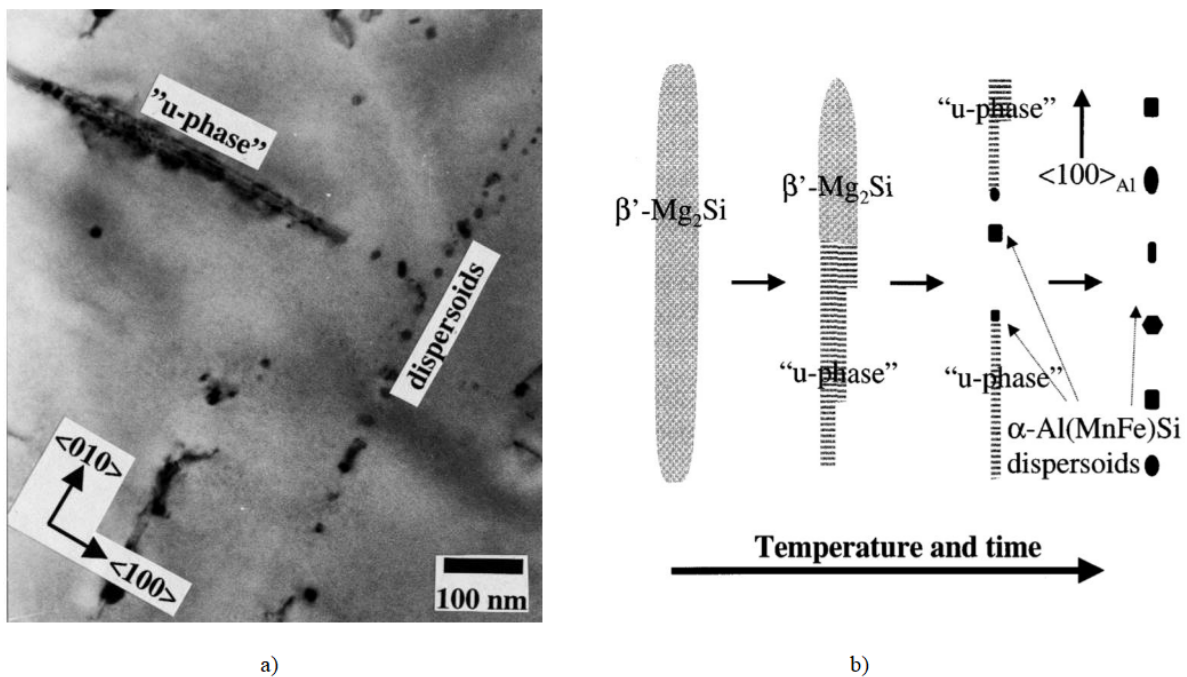
Figure 3.10: a) TEM bright-field micrograph of a 'u-phase' particle and Mn bearing dispersoids after continuous heating to 400°C in the Al-Mg-Si alloy b) Illustration of precipitation sequence [103].

The precipitation of metastable Mg_2Si precipitates in an Al-1.25Mn-0.26Si-0.57Fe alloy was investigated by Li et al. [104] in 2018. It was observed that with additions of Mg, metastable Mg_2Si precipitated in as-casted alloys. Upon continuous heating (5K/min), metastable Mg_2Si precipitates was observed to form at low temperatures due to the supersaturation of Si and Mg in the alloy. However, as the temperatures reached 275°C, the precipitates dissolved, leaving local Si-rich zones in the matrix. The authors did not detect the u-phase found by Lodgaard and Ryum [103]. These local Si-rich zones acted as favourable nucleation sites as α-dispersoids were observed to precipitate in the Si-rich zones. This occurred at temperatures above 350°C. A schematic diagram of the formation of α dispersoids based on metastable Mg_2Si is given in

Figure 3.11. By conducting isothermal heat experiments on the as cast alloy, the authors found that β'' and β' could form in the alloy and where stable at 175°C and 250°C respectively.
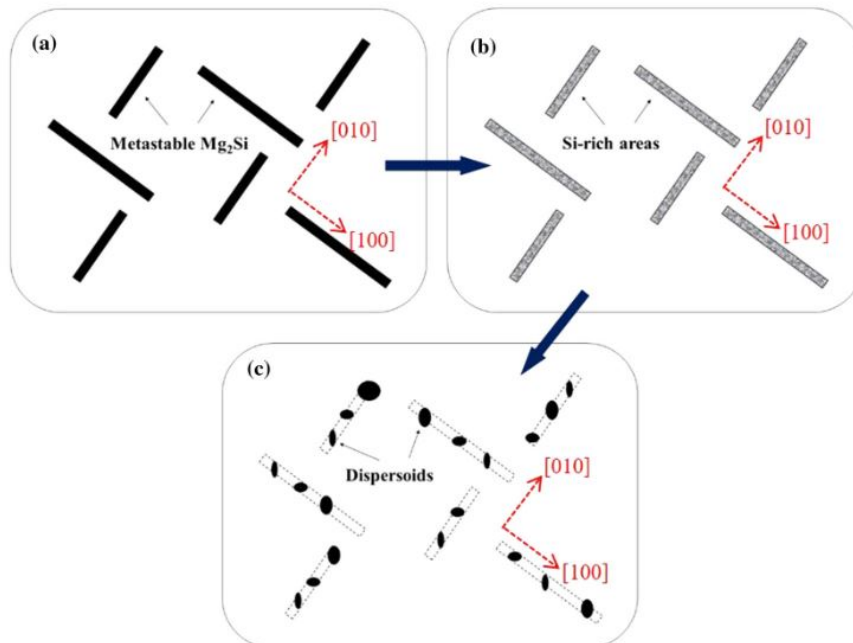
Figure 3.11: Schematic diagram (a) metastable Mg_2Si precipitated,(b) Mg_2Si dissolved forming Si-rich areas (c) α-Al(MnFe)Si dispersoids nucleate and grow in the Si-rich sites [104].

3.5   Hardening on Annealing

The 3xxx aluminium alloys are non-heat treatable and typically annealing reduces the strength level and increases the ductility of the material. However, a hardening effect has been observed at the early stages of annealing and has been referred to as hardening on annealing (HOA) which is typically associated with nanostructured materials. In nanostructured materials (materials with extremely fine microstructures from severe plastic deformation), HOA has been explained by dislocation source limitation where a heat treatment reduces the density and interaction of the dislocations. As the density of potential dislocation sources is reduced, the strength of the material increases and ductility is reduced [105, 106]. However, the hardening effect observed for the 3xxx series are seen at much lower strain levels. It has usually been observed during investigations of the annealing behaviour at low temperatures [9, 107–110]. While several investigations have reported of this behaviour, the phenomenon itself has not been widely studied and the mechanism behind is still unclear. In the following section, the literature which describe the evolution in mechanical properties seen during the hardening upon annealing phenomenon and their investigations on the mechanism.

In 1997 Sæter [24] studied annealing of an Al-0.89Mn-0.14Fe-0.07Si alloy. Prior treatment of the alloy was homogenization and cold rolled to strains of ϵ= 0.5, 1 and 3. The annealing behaviour was studied by isothermal flash annealing in oil and salt baths from 160°C to 320°C at various time intervals followed by quenching in water. The author reported of an age hardening effect from the hardness tests for the alloy cold rolled to a strain of 3 at annealing conducted at 160°C to 200°C. The time needed to obtain maximum hardness decreased with increasing temperature. At 200°C, the peak hardness was obtained at 100 seconds, while the peak was obtained after 1000 seconds at 160°C. This hardening effect was not observed at lower strains or at annealing temperatures above 200°C.

It was suggested by Sæter that the hardening is caused by zone or cluster formation. Tensile testing was conducted on samples annealed for 10 and 100 seconds at 200°C in the rolling direction, seen in Figure 3.12. The author observed that both flow stress and the ultimate tensile strength increased while the fracture elongation decreased with increasing annealing time. The flow stress increased with 13 MPa after 10 seconds and 10MPa after 100 seconds. Sæter was unable to detect any cluster formation by high resolution imaging investigations and concluded that no underlying mechanism had been unveiled by his investigations.
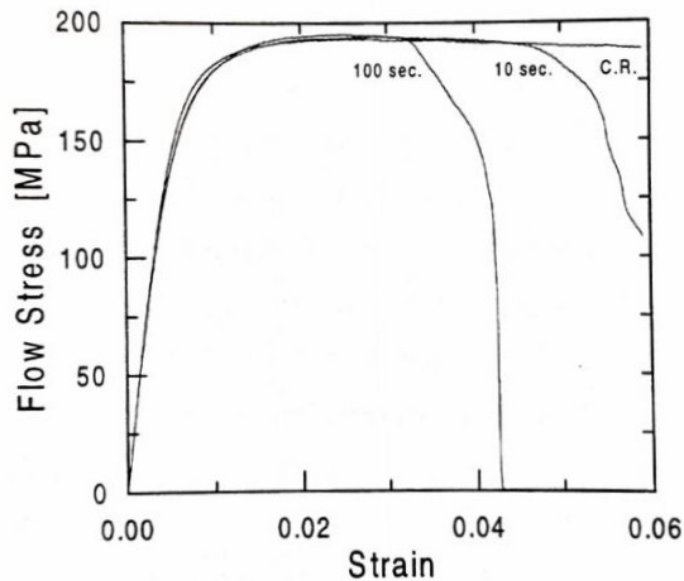
Figure 3.12: Stress-strain curves for Al-Mn alloy after cold rolled to ϵ=3 and annealed at 200°C for 10 and 100 seconds [24].

Similar studies were conducted by Tangen [10] in 2004. The experiments were conducted on an AA3103 aluminium alloy with composition 1 wt%Mn, 0.12 wt%Si and 0.57 wt%Fe. The hardening effect was investigated for four difference levels of Mn in solid solution, ranging from 0.31 to 0.72wt%. The different levels of supersaturation were achieved by utilizing three different homogenization treatments in addition to an as-cast variant. Before annealing was conducted,

all samples were cold rolled to a strain of ϵ=0.5, 1.5 or 3. Hardness tests and electrical resistivity measurements were carried out to follow the annealing behaviour.

The hardening effect was observed after annealing at 250°C for samples of various strain levels. At the lowest strain level, 0.5, the effect was only observed in the as cast variant (0.72wt% Mn_{ss}). With higher strains, the effect was observed for lower levels of solid solution after annealing for times ranging from 100-1000 seconds. The author did not report of any significant changes in conductivity during the hardening, which indicated no precipitation. No hardening was observed for the sample with the longest homogenization treatment i.e. lowest amount of Mn in solid solution. It was therefore concluded that the hardening effect is both dependent on strain level and on the amount of Mn in solid solution. Larger strain is needed to initiate the effect if the level of Mn in solid solution is lower. It was suggested by the author that with an increasing strain, the diffusion and nucleation rate increased as a result of a larger volume fraction of deformation heterogeneities.

The as cast variant with a strain of ϵ=3 was used to further investigate the phenomenon in FESEM to detect precipitation. No dispersoids were detected in the sample after 100 seconds where the hardening effect had been observed. At 1000 seconds of annealing, the hardness had decreased and had reached the initial level of hardness prior to annealing. However, the FESEM did not detect any dispersoids before the sample had been annealed for 10 000 seconds and the material had softened. The author did report of Mn- or solute bands after longer annealing times or at higher temperatures in which dispersoids later precipitated on as seen in Figure 3.5. The dispersoids had precipitated in bands on the deformation structure and it was therefore suggested by the author that precipitation had originated from the solute bands. It was concluded that the increase in hardness was the result of formation of solute zone or cluster of high Mn concentration, as a pre-stadium for dispersoids.

In 2006, Ryen et al. [111] investigated strengthening mechanisms in solid solution in aluminium alloys. Several high purity, commercial-grade and 3103 aluminium alloys were utilized to study the effect of alloying elements. In addition, different levels of Mn in solid solution in 3103 alloy was investigated by conducting various homogenization treatments. It was seen from tensile testing that Mn and other trace elements (Fe, Si, Ti, Cu) in solid solution had a stronger strengthening effect in commercial grade alloys than for high purity ones. It was suggested that this was the result of a synergy or clustering effect, creating harder spots in the alloy. To further investigate this effect, isothermal annealing was conducted on an AA1050 (Al-0.09Si-0.27Fe) and AA3103 (Al-1Mn-0.12Si-0.57) alloy with a rolling reduction of 95% (ϵ=3). The annealing temperature ranged between 100 and 200°C and hardness test was conducted at various times during the annealing. The change in hardness after annealing at 160°C is seen in Figure 3.13. As seen from the figure, a hardening effect was observed. The hardness in the AA3103 alloy had

increased with 10% during the first 15 minutes. It was reported of similar behaviour at 100°C and 200°C for different reaction times.
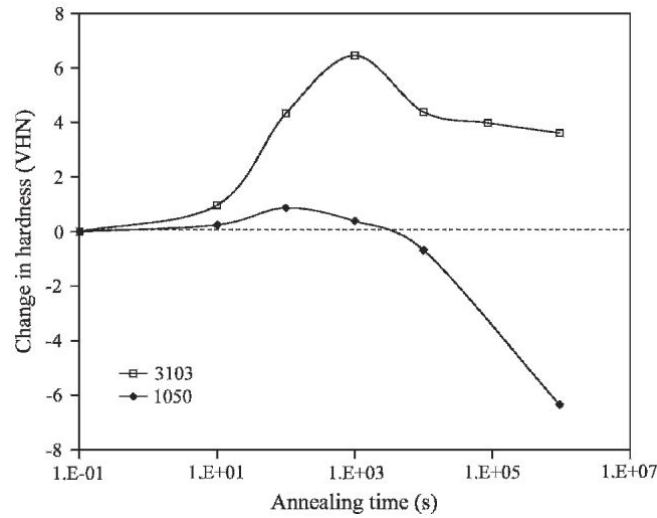
Figure 3.13: Change in hardness with isothermal annealing at 160°C of AA1050 and AA3103 95% rolling reduction [111].

It was stated by the authors that the hardening effect resembled ageing characteristics of age hardenable alloys but for the investigated alloys, the effect was in balance with recovery of dislocations as softening was observed at longer annealing times. The hardening effect was less pronounced in the AA1050 alloy, where the alloy had an increase of less than 2% and softening occurred at an earlier stage of the annealing. The lower resistance against recovery was attributed to the lower levels of solute in the AA1050 than in the AA3103. It was argued that the formation of cluster is possible despite the low diffusivity of Mn and further suggested that the low diffusivity would result in an increase in chemical potential for clustering due to supersaturation. The authors concluded that the formation of cluster is mainly attributed to a synergy effect, a result of dislocation core stimulated interaction between Mn and Si (as Si have higher diffusivity in aluminium) and possibly other trace elements in solid solution.

Birol et al. [107] found a similar hardening effect in a supersaturated Al-1.19Mn-0.61-Fe-0.16Si cold rolled thin sheets during isothermal annealing at lower temperatures. Each annealing procedure was held for 2 hours before hardness and conductivity measurements were conducted. As seen from Figure 3.14a, an increase in hardness was observed for the samples with a strain above 2.3 while no changes were observed in the conductivity measurements below 350°C.
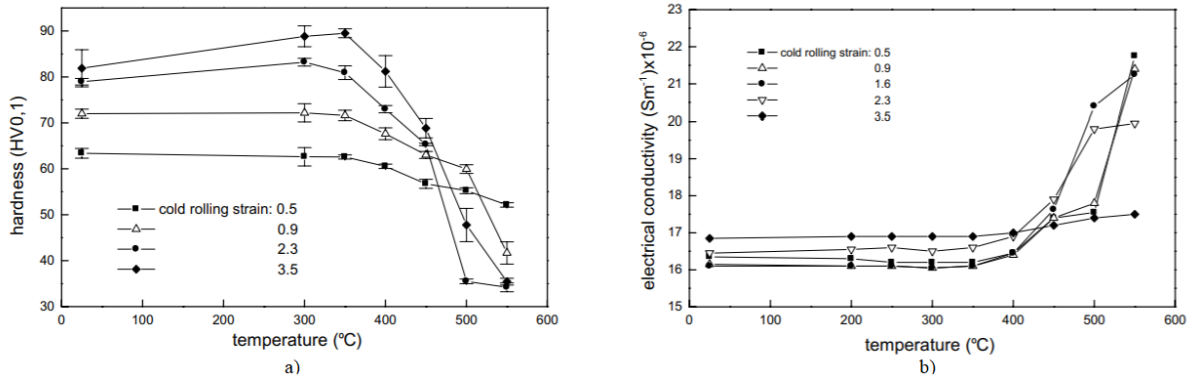
Figure 3.14: a) Change in hardness with annealing temperatures with strain levels indicated for the Al-1.19Mn-0.61-Fe-0.16Si alloy with corresponding b) change in electrical conductivity with annealing temperatures with strain levels indicated [107].

The annealing behaviour was further investigated by DSC, seen in Figure 3.15, as exothermic reactions such precipitation or softening can be detected due to changes in heat flow. As the exothermic peak near 350°C corresponded with the decomposition of the supersaturated solid solution, this peak was attributed to precipitation of Mn bearing dispersoids. The peak at 450°C was identified as the onset for recrystallization. However, an additional exothermic peak was as observed at lower temperature. The peak was detected for the sheets starting at a strain of 1.6 near 300°C, where the magnitude of the peak increased with increasing strain. The author suggested that this peak is caused by recovery activities as it was related to the release of deformation energy and the corresponding softening curves in Figure 3.14a. While it was argued that recovery restricted precipitation at strains above 1.6, the author did not further discuss any specific mechanism for the hardening phenomenon.
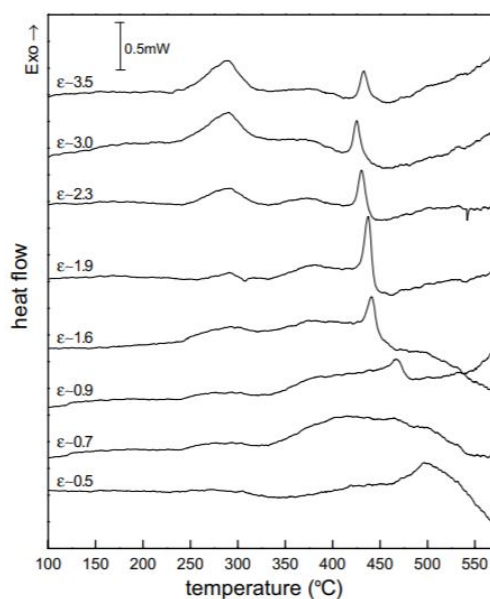
Figure 3.15: DSC scans of the Al-1.19Mn-0.61-Fe-0.16Si alloy at indicated strain levels [107].

In 2012 Lee et al. [112] observed a similar hardening effect during their investigations on the effects of Mn on the tensile properties of rolled 1xxx aluminium alloys sheets during recovery annealing. The effect from Mn were investigated by studying alloys with varying composition of Mn and Si and by conducting heat treatments to reduce amount of Mn in solid solution. All sample had a rolling reduction of 95.5% prior to annealing.

Hardness measurements were conducted after 3 hours of annealing at temperatures below 300°C. As seen from the measurements in Figure 3.16, an increase in hardness was observed after annealing between 200°C and 220°C. It was deduced from the hardness measurements that the phenomenon is influenced by the amount of Si (and Fe) in solid solution. By comparing samples with different compositing as seen in Figure 3.16a, a clear trend was observed where higher higher additions of both Mn and Si increased the magnitude of HOA. It was further observed from Figure 3.16b that lower amount of elements in solid solution reduced the possibility of HOA. Furthermore, the result from Figure 3.16c implied that the hardening was related to Si and Fe.
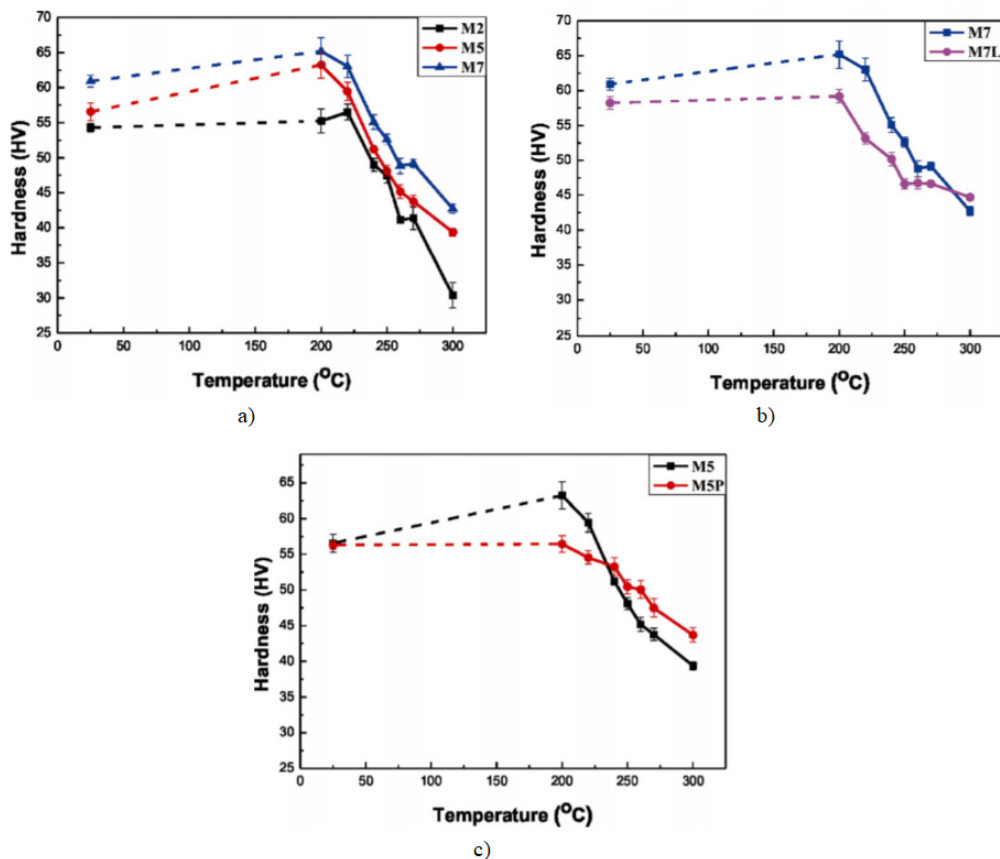
Figure 3.16: The change in hardness with annealing temperature a) for alloys with increasing amount of Mn and Si (M2: low, M5: medium and M7: high) b) for alloys with high (M7) and low (M7L) amount of Mn in solid solution c) M5 have additions of Mn, Si and Fe while M5P is a binary Al-Mn alloy [112].

It was argued by the authors that it is unlikely that the hardening is caused by neither diffusion of Fe and Mn as both have a low diffusivity in aluminium nor precipitation of Mn bearing dispersoids, as it would not occur at low annealing temperatures. They suggested precipitation of Si as a possible mechanism as precipitates of Si had been observed by TEM Al-Fe-Si at temperatures below 250°C. However, the authors did not further investigate this mechanism and none of samples with increased hardness was investigated by TEM or SEM.

In 2013 Govindaraj et al. [106] studied the hardening on annealing behaviour in a cold rolled AA3103 alloy by tensile testing. The AA3103 alloy had a composition of 0.98 wt% Mn, 0.54 wt% Fe and 0.12 wt% Si in balance with Al. To study the effects of Mn and Si in solid solution during annealing, different homogenization treatments were applied on the AA3103 alloy and an Al-0.5Si alloy was tested as well. After the homogenization, the AA3103 alloy was cold rolled to a series of strain levels ranging from 0.57 to 4.7 followed by annealing conducted on a wide range of combination of temperatures and times. In addition, some samples (with strain of 4.2) was subjected to additional deformation by accumulated roll bonding before annealing were performed. From the annealing experiments seen in Figure 3.17, a clear trend was observed where the hardening peak shifted from longer to shorter times with increasing strain at a given temperature. In addition, the maximum obtained increase of the hardening peak increased with increasing strain.
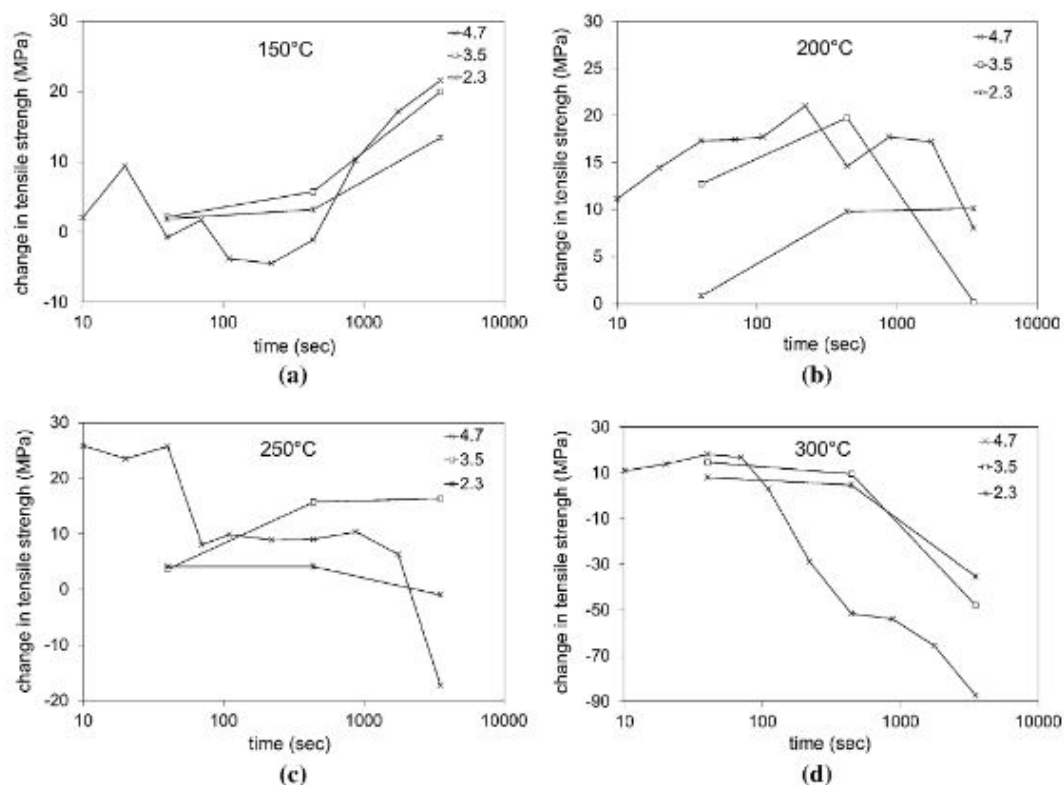
Figure 3.17: Changes in the tensile strength of AA3103 as a function of times at a) 150 b) 200 c) 250 and d) 300°C as a function of time for rolling strains 2.3, 3.5 and 4.7 [106].

57

Tensile tests after annealing at 225°C for 10 minutes are seen in Figure 3.18. It was observed that for samples of low strain, the annealing resulted in an increase in elongation with or without a small decrease in tensile strength. The transition from softening on annealing to hardening on annealing at 225°C for 10 minutes is observed in the strain rage of 1.15 to 1.7. At larger strains, the uniform elongation decreased and was accompanied by an increase in ultimate tensile strength. The increase in ultimate tensile strength varied from 5 MPa to 30 MPa, where the magnitude increased with larger prestrains. No significant increase in 0.2% offset yield strength was observed below a strain of 3.5.
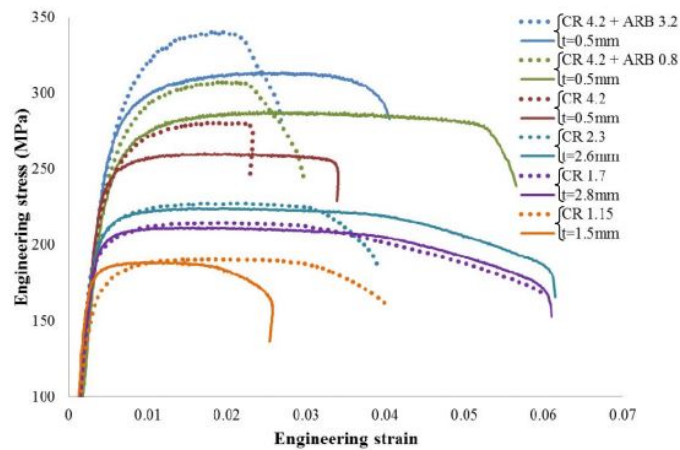
Figure 3.18: Engineering stress-strain curves of AA3103 strips at different strain levels in the as-deformed and annealed conditions represented by solid lines and dotted lines respectively after annealing at 225°C in 10 minutes. The thickness of the tensile specimens are indicated by t. Tensile test is preformed in the rolling direction [106].

The evolution in tensile properties seen after annealing at 225°C for 10 minutes could not be explained by texture as no changes was detected. The (111) pole figure for the sample deformed to a strain of 4.2 before and after annealing at 225°C for 10 min is given in Figure 3.19. As seen, no significant differences are observed.
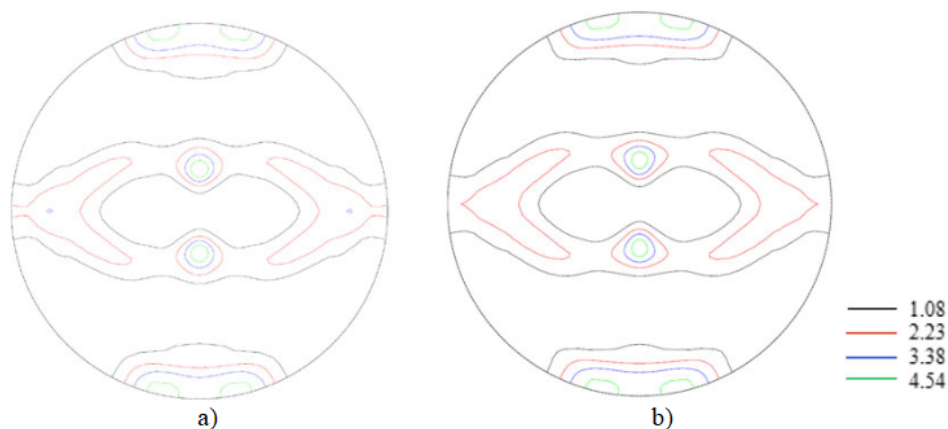
Figure 3.19: The (111) pole figure of AA3103 at a) deformed to a strain of 4.2, b) deformed to a strain of 4.2 and annealed at 225°C for 10 min [106].

The change in mechanical properties could not be explained by a evolution in microstructure either, as only minor variations was detected in the subgrain misorientation. TEM images of the subgrain structures before and after annealing at 225°C for 10 min are seen in Figure 3.20. A similar trend was seen from the electrical conductivity measurements as well, where the changes between the as deformed state and the annealed state. Neither TEM investigations did not detect any precipitation of particles after 10 minutes of annealing. Small precipitates, in the range of 10-20 nm, was however detected in TEM after annealing at 225°C 4 hours.
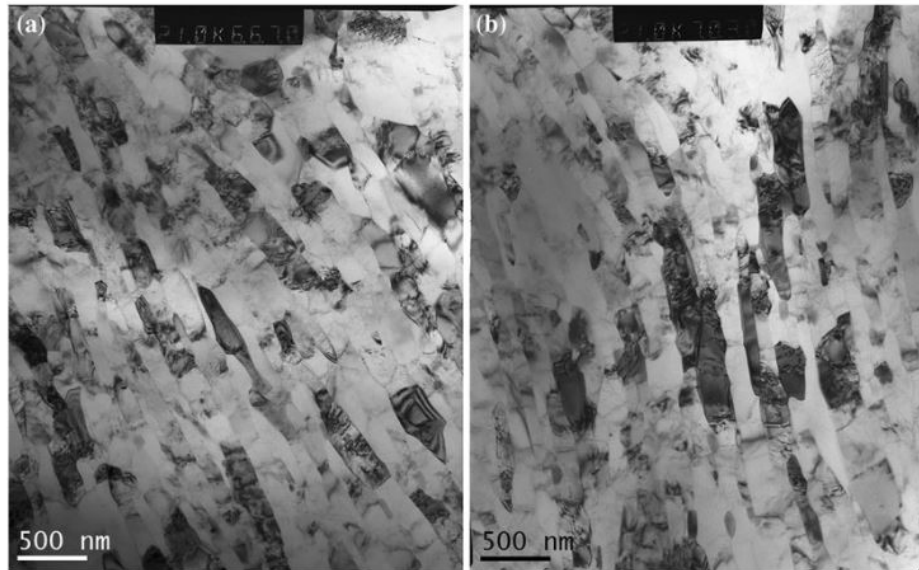
Figure 3.20: TEM images of subgrain of AA3103 a) cold rolled to strains of 4.2 followed by one pass ARB, b) after annealing at 225°C for 10 min [106].

The authors further applied additional 15% rolling on the annealed samples and compared its mechanical properties to the annealed and as deformed samples. It was observed from Figure 3.21 that the additional deformation did not cause the tensile properties to change from those seen for the annealed ones.
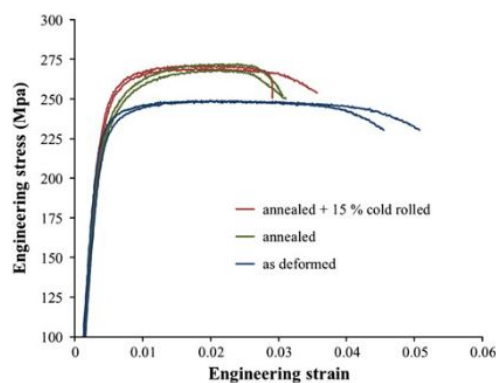
Figure 3.21: Engineering stress–strain curves of AA3103 at a rolling strain of 3.5 in the as-deformed, annealed at 225° for 10 min, and annealed + 15% cold-rolled conditions [106].

59

The authors discussed the hardening on annealing phenomenon in terms of how it would alter the balance between storage and dynamic recovery of dislocations. While changes in the storage rate of dislocation could increase hardness, this was seen as not likely as a significant amount of observable dislocation obstacles like grain boundaries or dispersoids had to be introduced.

It was therefore argued that the rapid hardening is caused by a reduced dynamic recovery by the introduction of weaker obstacles for dislocation pinning subsequent to the annealing treatment. Both static strain aging and the dislocations them self as pinning points were not seen as likely as both effects would be erased by the additional 15% rolling. It was therefore proposed that HOA was caused by precipitation of small particles or rearrangement of solutes cluster, both difficult to detect and verify.

DSC scans revield exothermic peaks at below 300°C, which the authors suggest could be caused by precipitation of Si which would be to small for detection in TEM. However, from the experiments conducted on samples with longer homogenization treatments, it was observed that lower amounts of alloying elements (Si and Mn) in solid solution did not influence the magnitude of the HOA. It was therefore argued that the influence from Si on HOA in Al-Mn is minor as the amount of Si in solid solution are very small upon longer homogenization treatments. As no HOA effect was observed for the Al-0.5Si alloy, the authors concluded that Mn is crucial for the effect to occur, however the level of Mn in solid solution is of little importance for HOA. It was also suggested that diffusion of Si into the vicinity of Mn, creating clusters, could be a possible explanation for HOA as Si have a higher diffusivity in aluminium.

While the samples with higher strains could be explained dislocation source limitations, it was argued by the authors that the hardening is caused by other mechanisms as HOA was observed at strains below 3. And it was further pointed out that if this was caused by dislocation source limitation, then the 15% rolling preformed on the annealed sample would remove HOA effect.

3.5.1   Models for Cluster Strengthening in Aluminium Alloys

While cluster strengthening has been observed during early stages of aging of heat treatable alloys (i.e. Al-Cu-Mg and Al-Mg-Si alloys) [113–116], the mechanism behind the phenomenon is still unclear. As these cluster are small, strengthening models derived from larger cluster (GP-zones) are not applicable. Recently, application of atom probe tomography (APT) and atomistic simulations have reviled that small clusters can contribute considerably to strength [117–119]. In the following section, two models are presented together with an application of these models on a strengthening on a 3xxx alloy.

In 2009 Starink and Wang [120] proposed a model where strengthening from a cluster arises from order strengthening in combination with modulus hardening. The model was deduced from the

simplest form of a co-cluster, consisting of 2 atoms from two different alloying elements, termed dimers.

The order strengthening was suggested by the authors to occur because of the interaction between a dislocation and the dimer. As seen from the Figure 3.22, the model was based on a dimer set on two {111} planes in the lattice with a dislocation located in between those {111} planes. Depending on the configuration of the dimer, the dislocation would either shift the dimer one Burgers vector or break it subsequent to the dislocation passing. In the case of elimination or cutting of a co-cluster, additional energy is required while two atoms brought together as seen in the bottom of Figure 3.22 would release energy.
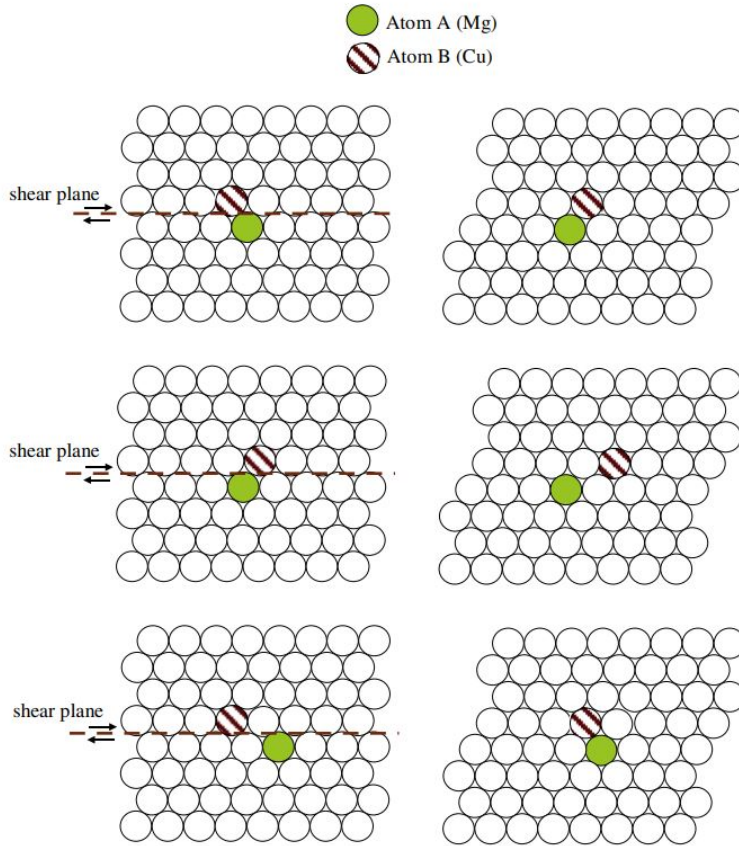
Figure 3.22: A {111} plane in a fcc lattice with a 2 atom cluster being cut by a dislocation [120].

The work done from the moving dislocation per unit area on the slip plane was given by:

$$\Delta\tau_{SRO} = \frac{\gamma_{SRO}}{b} \tag{3.1}$$

where γ_{SRO} is the change in energy per unit area on slip plane from the passing dislocation and b is the Burger vector. To further analyse γ_{SRO}, the change in area density of the bonds nearest the atoms from a passing dislocation was considered. The initial area density of the nearest

neighbouring bonds was given by:

$$\rho_{A-B}(n_d = 0) = \frac{y_a + y_b}{S_{111}} \tag{3.2}$$

where $S_{111} = \sqrt{3}b^2/4$ is the area of the {111} plane occupied by one atom, y_a and y_b is the amount of A and B atoms in the co-cluster respectively. Furthermore, the authors considered the geometry of the fcc lattice. As each atom have 12 nearest neighbours, each atom adjacent to a slip plane have 3 nearest neighbours on the other side of the {111} slip plane. A passing of a dislocation in the {111} plane, would result in a 1/3 of the nearest neighbour bonds to an atom will remain while the rest is broken. The total area density after passing of a single dislocation was therefore given as:

$$\rho_{A-B}(n_d = 1) = \frac{1}{S_{111}} \left[\frac{2}{3}(y_a + y_b) + \frac{2}{3}y_a x_b + \frac{2}{3}y_b x_a + 2x_a x_b \right] \tag{3.3}$$

where x_a and x_b is the amount of A and B atoms in the M-rich phase respectively. As the first dislocation experiences the greatest resistance towards further movement, additional passing of dislocations would not contribute to further strengthening. The cutting of bonds in the dimer was further related to the enthalpy for cluster formation, ΔH_{A-B}, and the strengthening contribution from clustering was given by:

$$\Delta \tau_{SRO} = \frac{\Delta H_{A-B}}{b} \left[\rho_{A-B}(n_d = 0) - \rho_{A-B}(n_d = 1) \right] \tag{3.4}$$

The strengthening contribution from modulus hardening was attributed to the interaction forces of screw and edge dislocation as they pass through the area (the precipitate) consisting of a different shear modulus then the matrix and was given by:

$$\Delta \tau_m = 1.4 \alpha^{3/2} \Delta \gamma^{3/2} f^{1/2} b \left(\frac{r_p}{b} \right)^{3\beta/2 - 1} (2\pi S)^{-1/2} \tag{3.5}$$

where S is the dislocation line tension, f is the volume fraction of clusters, $\Delta \gamma$ is the difference shear modulus between the cluster and the surrounding metallic phase and r_p is the radius of the precipitate. The α and β parameters are obtained from dislocation core models based on the interaction forces between dislocation and precipitate. As these parameters are dependent on the model used, the values from $\Delta \tau_m$ was stated as uncertain. Any strengthening from the classical shearing of precipitates caused by the interfacial energy between the precipitate and matrix was neglected.

The model was tested with various Al-Cu-Mg alloys where the contribution from order

strengthening was estimated with calorimetry (DSC) by considering the evolution in heat flow. The authors reported that the model was able to predict the enthalpy change caused by interaction of co-clusters and was further able to estimate strengthening contribution from co-clusters on the yield strength in alloys aged or heat treated at low temperatures (20-220°C). The increase in strength was proportional to the enthalpy change corresponding to the formation of co-cluster. As the predicted strength based on heat flow resembled the measured strength, the authors concluded that the main strengthening contribution was caused by order strengthening. In 2012, Starink et al. [121] used a similar model to predict the strengthening contribution from clusters in Al-Mg-Si alloy aged at room temperature after solution treatment.   3-D atom probe analysis were preformed to verify the model by detecting formation of clusters. The clusters contained 2 to 16 atoms with an average Mg:Si ratio close to 1. The increase in strengthening were observed to be proportional to the change in enthalpy related to co-cluster formation.

In 2014 Zhao [122] proposed a model for strengthening from small clusters (less than 1 nm in diameter) by considering the elastic effect of size misfit. Similar to solute strengthening, the model was based on the misfit strain field which arises from clusters in the matrix. The assumptions for the model was that the clusters were treated as point obstacles with a low density and the volume misfit of a small cluster was assumed to be equal the sum of misfit of all the atoms in the cluster, i.e the volume of the misfit of a small cluster i was given as:

$$\Delta V_{cl} = i\Delta V \tag{3.6}$$

The interaction energy ΔE of a substitutional atom with a edge dislocation was given as:

$$\Delta E = \frac{1-v}{1+v}\sigma_h \Delta V \tag{3.7}$$

where v is Poisson's ratio and σ_h is the hydrostatic stress induced by an edge dislocation. The interaction force between the dislocation in the glide direction y and a solute atom was given as:

$$f = -\frac{d\Delta E}{dy} \tag{3.8}$$

The critical shear stress from a solute was deduced from the Fleshier-Friedel model and was given by:

$$\Delta \tau_F = A_{fm}^{3/2} c_0^{1/2} = A_1 \Delta V^{3/2} c_0^{1/2} \tag{3.9}$$

where c_0 is the total solute concentration, A and A_1 are constants, and f_m is the maximum interaction force between a solute and a dislocation. The critical shear stress for cluster follows from Equation 3.6 and 3.9 and was given by:

$$\Delta\tau_{Cl,f} = A_1\Delta V^{3/2}c_0^{1/2}i = i\Delta\tau_F \tag{3.10}$$

Which is valid at 0 K. The stress contribution will be reduced at elevated temperature due to the atomic thermal motion where the temperature dependence was given by:

$$\Delta\tau(T) = \Delta\tau_0 \quad \exp\left(-\frac{kT}{0.51E_b}\ln\frac{\dot{\epsilon}_0}{\dot{\epsilon}}\right) \tag{3.11}$$

where E_b is the energy barrier, given as:

$$E_b \approx A_2\Delta V^{2/3}c^{1/3} \tag{3.12}$$

where A_2 and $\dot{\epsilon}_0$ are constants. By comparing the model to a coherency strengthening model, it was seen that the model was applicable for cluster of with less than 10-20 atoms. It was further observed that the strengthening contribution is proportional to the mean number of atoms per clusters. It was commented that the misfit stress model is a transition between solute strengthening to coherent particle strengthening. Zhao further discussed the proposed model with the order strengthening model. It was suggested that both Cu-Mg and Mg-Si clusters are energetically favourable and would therefore have smaller elastic misfit than single atoms. The misfit strengthening contribution would therefore be low or negligible and their strengthening contribution may therefore be explained by the order strengthening. Cluster containing atoms with a larger volume misfit, however, can be explained by the proposed model (i.e. Mg-Mg, Cu-Si).

A simplified cluster strengthening model were further developed by Zhao et al. [123] in 2015. Compared to the previous models, the model included the localised influence of clusters on dislocation dissociation and stacking fault (i.e. splitting of dislocations). The model was used to explain the significant increase in strength seen in Al-Mn-Si alloys compared to binary Al-Mn alloys. The model addressed both the order strengthening and size misfit effects from atom dimers and the total strengthening from the cluster where expressed as

$$\Delta\tau_{clu} = \Delta\tau_{mis} + \Delta\tau_{ord} \tag{3.13}$$

Where $\Delta\tau_{mis}$ is the misfit straightening and $\Delta\tau_{ord}$ is the order strengthening. The contribution

from order strengthening were modified from Equation 3.1 and 3.4, expressed as

$$\Delta\tau_{ord} = \frac{\Delta E_s}{bS_{111}}2c_{cl}P_{sh} \tag{3.14}$$

Where ΔE_s is the required energy to breaking of a cluster, $P_{sh} = \frac{1}{6}$ is the fraction of dimers modified by the gliding dislocation and $2c_{cl}$ is the statistical chance for an atom at one of the adjacent 111 plane is Mn or Si and part of a dimer, similar to the breaking of a cluster illustrated in 3.22. The misfit strengthening at 0 K was expressed as

$$\Delta\tau_{mis} = A_1\Delta V_{cl}^{4/3}c_{cl}^{2/3} \tag{3.15}$$

Where ΔV_{cl} is the sum of volume misfit of a cluster and c_{cl} is the cluster concentration. The temperature dependence was expressed as in Equation 3.11.

The predicted yield stress from the model was compared with tensile tests conducted on pure binary Al-Mn and ternary Al-Mn-Si alloys at 78 K and at room temperature. The input parameters (binding energy and misfit) for the two strengthening contributions were estimated by preforming atomistic calculations on the interaction energy between pairs of solutes based on Si and Mn. Interaction between Si-Si and Mn-Mn were neglected as the attraction from Si-Mn cluster were the strongest and are more likely to occur.

The results from the predicted shear stress and the experimental values are seen in Figure 3.23. Only yield stress was considered to avoid strengthening contribution from dislocations during work hardening. The contribution from grain size was corrected to be able to compare alloys with different grain size. It was observed by the authors that the predicted strength contribution from cluster misfit corresponded well with the trends of the measured values while the contribution from order strengthening were only 0.2 MPa. It was therefore concluded that misfit strengthening plays a major role on the strengthening contribution from clusters in Al-Mn-Si alloys.
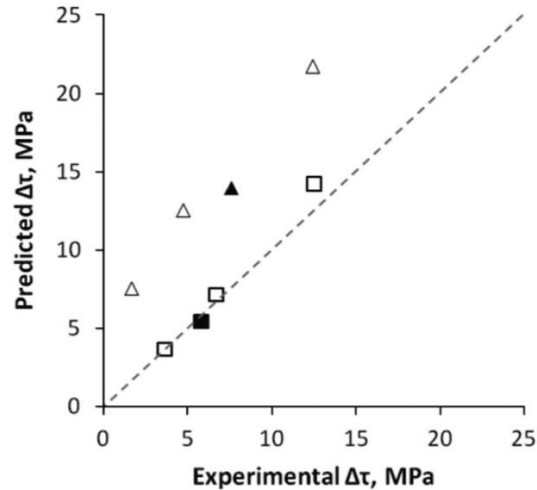
Figure 3.23: The predicted shear stress of Al–Mn (open symbols) and Al–Mn–Si (filled symbols) versus experimental values. Squares represent values at room temperature and triangles represent values at 78 K [123].

3.6   Mechanisms for Hardening by a Strain Path Change

In this section, an overview of previous literature on aluminium alloys where the objective has been to characterize the influence of dislocation structure and anisotropy on transient effects on the work hardening rate.

In 1976, Hutchinson et al. [80] studied the effect of strain path changes in several metals by conducting uniaxial prestrains in tension followed by stretching perpendicular to the original tensile axis. It was seen that the influence of a strain path change was dependent on stacking fault energy, where steel and aluminium was more susceptible towards prestrains than copper and brass. The authors reported of a reduced work hardening rate when the material was strained in two different direction. For the aluminium alloy, the decrease in work hardening rate resulted in an instability even at small prestrains. It was further reported that the effect of prestrain was not just transient, as a drastic reduction in ductility was observed after prestrains above 10%. As the authors found an increase in r-value after prestraining, the observed phenomenon was suggested as an effect of a reduction in active slip system with a strain path change. As only some of the dislocations introduced during prestraining is capable of glide during the second strain path, the frequency of interactions between dislocation will be reduced which leads to the instability.

Lloyd and Sang [88] conducted similar orthogonal strain path tests on several aluminium alloys in 1979. Soft sheets of AA1100-0, AA3003-0, AA2036-T4 and AA5182-0 were subjected to a two-stage tensile straining with an initial prestrain either in the rolling or transverse direction, followed by a tensile strain 90° to the initial direction. For both the AA1100-0 and the AA3003-0

alloy, a prestrain above 10% resulted in a significant reduction in ductility. As seen from Figure 3.24, a orthogonal prestrain produced higher flow stress than seen for the monotonic curve and above 10%, the flow stress was greater than the ultimate tensile strength for the monotonic curve. The increase in flow stress was accompanied by a decreased work hardening rate. Further straining caused softening and instability. The authors conducted the same prestraining in AA2036-T4 and AA5182-0, however, it was observed that both alloys were unaffected by the strain path change.
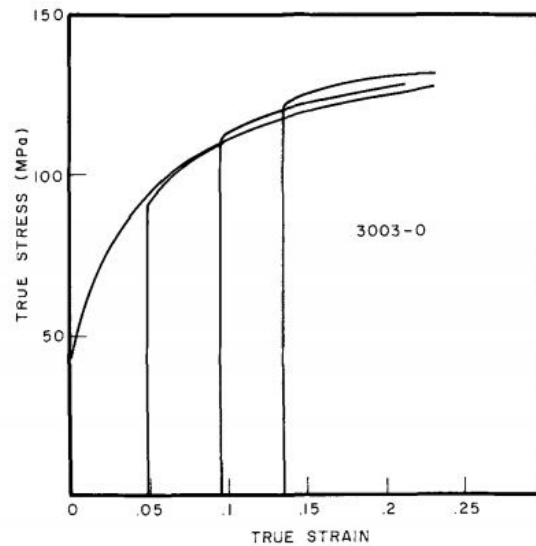
Figure 3.24: Stress-strain response of AA3003-0 after various orthogonal prestrains [88].

An analysis of the dislocation structure showed that diffuse cells structure formed at low strains in the AA1100-0 and the AA3003-0 alloy during the prestrain, seen in Figure 3.25. As the strain increased, the cell structure became more developed. In contrast, the AA2036-T4 alloy formed a banded dislocation structure and the AA5182-0 alloy formed a homogeneously distributed structure. As both AA2036-T4 and AA5182 were unaffected by the strain path change, it was suggested that these structures have a larger resistance towards changes in active slip system. The author further attributed the effects observed for the AA3003 and the AA1100 to the formation of a dislocation distribution during prestrain which becomes unstable with a 90° change in straining direction.
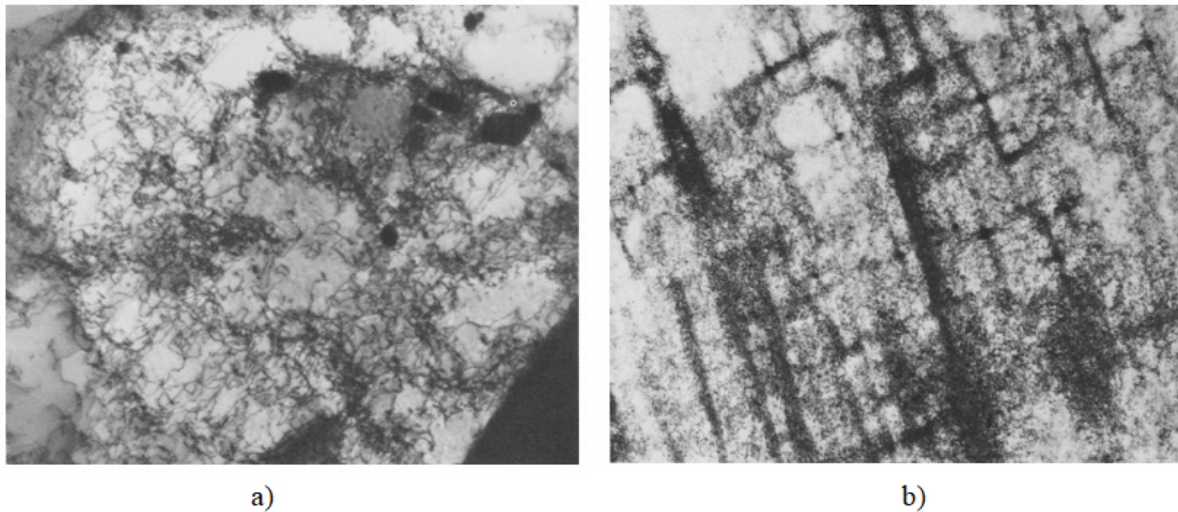
Figure 3.25: The dislocation structure developed after 10% prestrain in a) AA1100-0 and b) AA2036-T4 [88].

Zandrahimi et al. [81] investigated effects of abrupt changes in strain path on work hardening in several metals including a commercial pure (CP) aluminium alloy. Three different samples were investigated, A1, A2 and A3, to investigate the influence of texture and microstructure. While A1 and A2 had a recrystallized grain structure, A3 had a recovered structure with well developed subgrains. Samples A1 and A3 both had strong cube component and planar anisotropy, as they were stronger 45° to the rolling direction compared to 0° and 90° to the rolling direction. The A2 sample had retained rolling texture and had very little planar anisotropy.

Orthogonal strain path tests were conducted with various prestrains in the rolling direction followed by tensile testing in either 45° or 90° to the rolling direction. The results for A1, A2 and A3 are given in Figure 3.26, 3.27 and 3.28 respectively with the corresponding monotonic curves. The authors reported of a minor increase (less than 3%) in flow stress for all the samples followed by a transient reduction in work hardening rate. It was seen that samples with a recrystallized grain structure (A1 and A2), had a larger amplitude of the transient behaviour of the work hardening rate than for the recovered sample (A3). They also observed that the A1 sample resulted in a larger amplitude in the 45° tests compared to the 90° tests. However, the the required strain to give a severe reduction in uniform elongation increased for the 45° tests compared 90° tests. As this was not observed in the A2 sample, the phenomenon was attributed to the planar anisotropy and the superior work hardening rate for the A1 sample at 45°. The authors suggested that the observed reductions in hardening rate was attributed to the partial dissolution of the dislocation substructure generated during prestraining and they concluded that the work hardening is influenced by both grain structure and anisotropy.
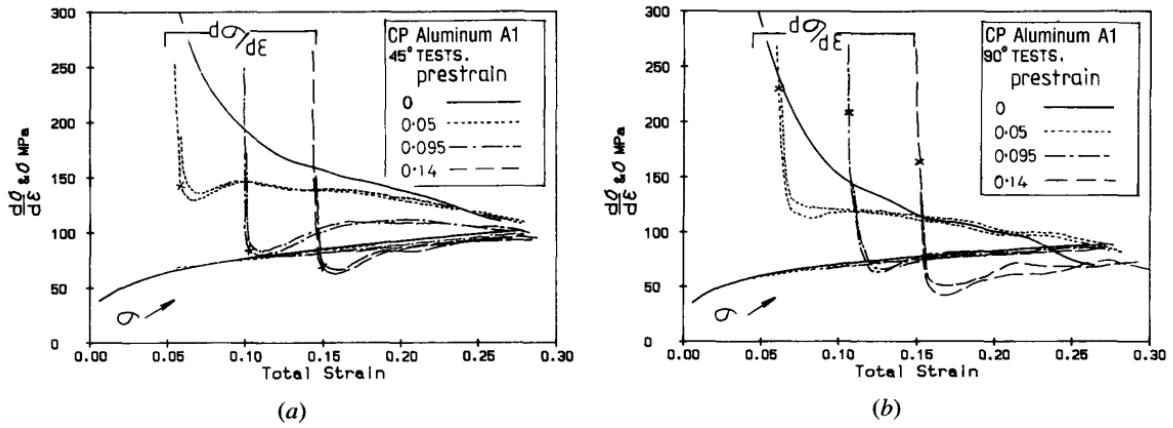
Figure 3.26: Stress and work hardening rate as a function of total effective strain for sample A1 a) 45° change in strain path b) 90° change in strain path [81].
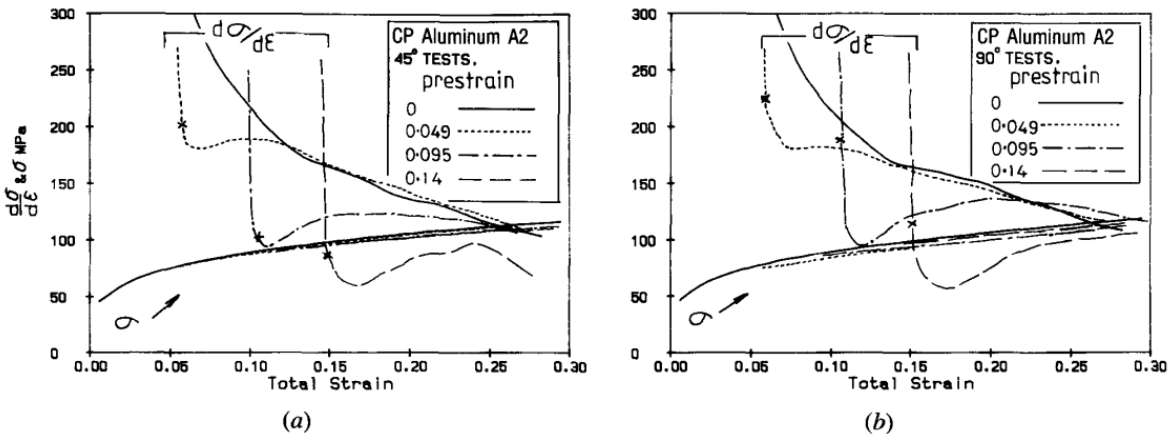
Figure 3.27: Stress and work hardening rate as a function of total effective strain for sample A2 a) 45° change in strain path b) 90° change in strain path [81].
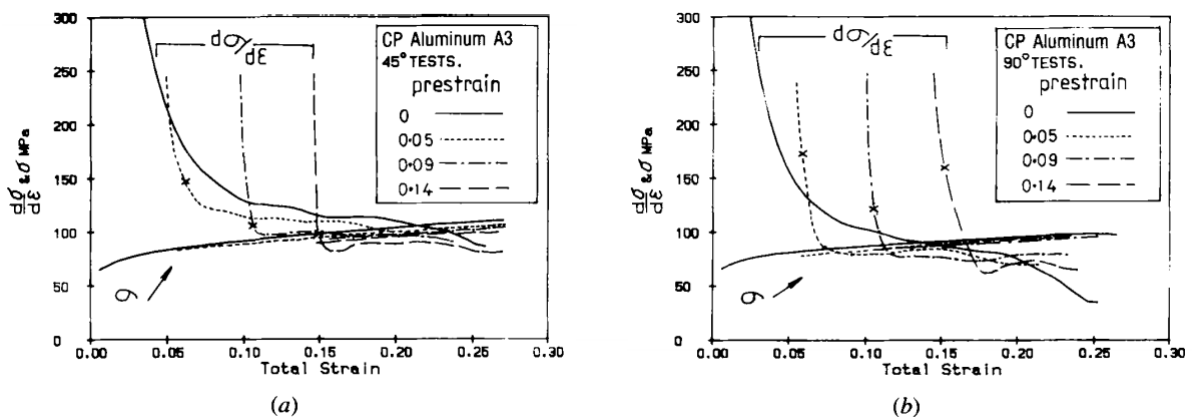
Figure 3.28: Stress and work hardening rate as a function of total effective strain for sample A3 a) 45° change in strain path b) 90° change in strain path [81].

In 1991, Li and Bate [78] investigated strain path changes in an equiaxed, cube textured commercial pure AA1100 aluminium alloy. The material was anisotropic, as it had higher strain hardening rate combined with a lower yield stress 45° to the rolling direction compared to 0° and 90° to the rolling direction. The contraction ratio was also significantly lower at a 45° to the rolling direction than the two latter ones. Tension-tension tests were conducted both with a 45° and a 90° change in straining direction and the results are given in Figure 3.29. It was seen that SPCs lead to a transient behaviour, as it resulted in higher flow stress and the work hardening rate was initially high followed by a rapid decrease. It was observed that a prestrain at 45° had a larger effect on the magnitude of the strain path change as the increase in flow stress was larger than those seen at 90°. This was attributed to the greater strain hardening of the material at 45°. The authors could however not explain the larger amplitude on the work hardening rate for tests prestrain at 45°.
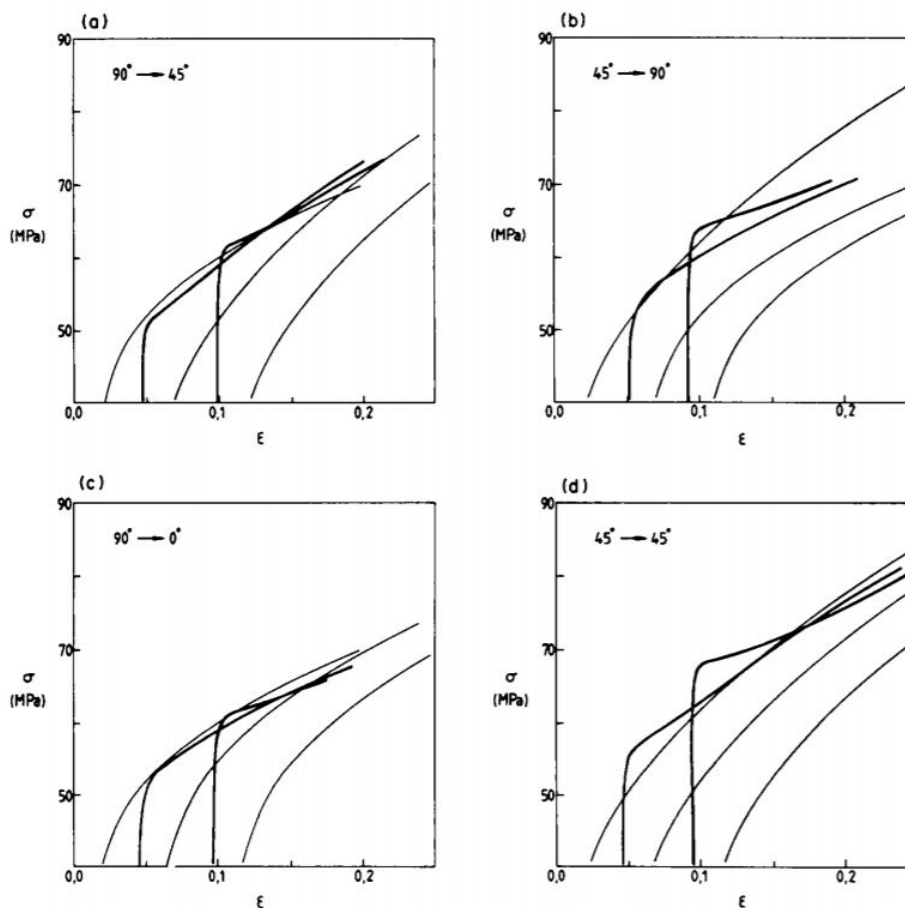
Figure 3.29: The flow stress behaviour in uniaxial tension following a change in strain path for the AA1100 alloy: (a) 90° prestrain and 45 ° test direction; (b) 45° prestrain and 90° test direction; (c) 90° prestrain and 0° test direction and (d) +45° prestrain and -45° test direction. The curves are offset in strain by the amount of prestrain. The monotonic behaviour in the prestrain direction, and the offset behaviours of monotonic tests in the test direction, are also shown as feint lines [78].

It was further reported that the strain path change produced persistent changes to the mechanical behaviour and not just the transient ones as the SPC tests did not approach the monotonic behaviour until a significant increase in stress is applied as seen in Figure 3.30.
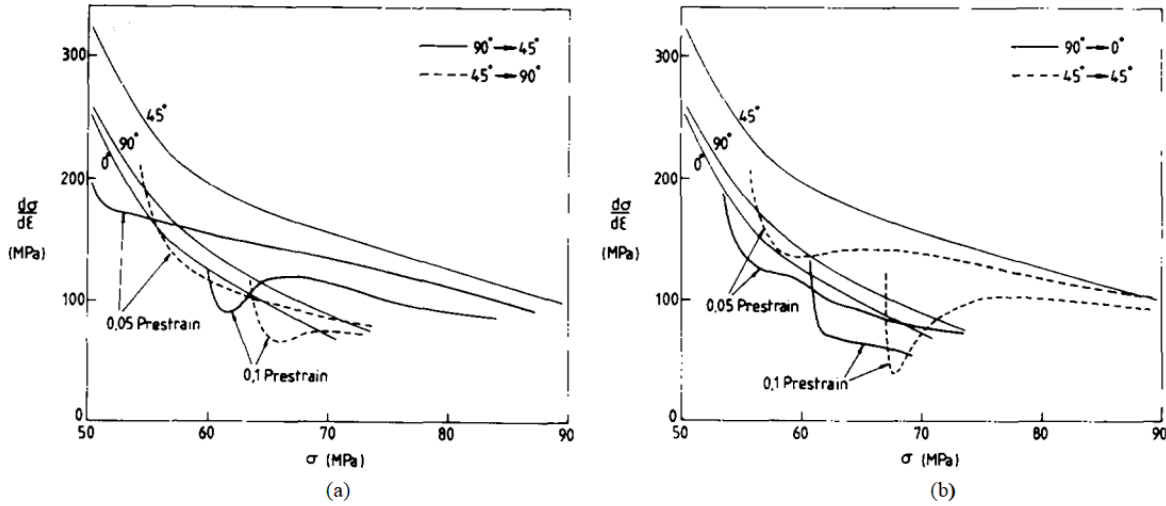
Figure 3.30: The strain hardening rate as a function of flow stress for both monotonic and path change uniaxial tension tests, with: (a) 45° differences between prestrain and test tensile axes and (b) 90° differences between prestrain and test tensile axes [78].

Barlat et al. [79] investigated strain path changes at pseudo-monotonic, cross and pseudo-reverse loading conditions for an 1050-0 aluminium alloy. The authors correlated observed changes in the mechanical behaviour seen during two step tensile-shear tests with the evolution in dislocation structure by TEM imaging. The dislocation structure seen with monotonic axial tension and simple shear seen in Figure 3.31a and 3.31b, respectively.

For the pseudo-monotonic loading (ϕ=0.85), the material yielded at a lower stress and subsequently hardened at a higher rate than the monotonic curve. However, after a small amount of strain, the hardening rate approached to the monotonic hardening rate. The authors observed that the dislocation structure was already present at low strains (below 0.15) as seen in Figure 3.32a. The authors suggested that the dislocation structure had reorganized into walls on the most active slip planes during the shear test that had already been active during the axial tension prestraining. After cross loading (ϕ=0), a lower yielding stress was observed, however the transient period with increased hardening rate was longer and resulting in a higher strength level than for the monotonic curve. It was seen from the dislocation structure up to a strain of 0.15 in Figure 3.32 that the structure was the superimposition of the previous structure seen during uniaxial tension with the new structure of the final shear mode. There was no evidence of cell dissolution. With a pseudo reverse loading test (ϕ=-0.85), the material yielded at a lower stress with a subsequent transient period of higher work hardening rate. The increase in hardening was followed by a short period of a lower hardening

before the strain hardening increased again and approached the monotonic behaviour. From TEM imaging, the prestrain structure up to a strain of 0.15 was found to be blurred. The observed single dislocations inside and between the cells indicated dissolution of the structure developed during prestraining. The stagnation of the work hardening was attributed to the dissolution of the cell structure after reloading. At strain of the order of 0.3, the dislocation structure obtained by the prestraining were completely erased in all three samples.

Based on their findings, the authors attributed the magnitude of the transient stage of the work hardening rate to the establishing of the final dislocation structures. The transient hardening stage was observed to last for a shorter strain range for the pseudo monotonic than for the cross loading and pseudo reverse, as the final dislocation structure were established at a smaller strain.

a)   b)
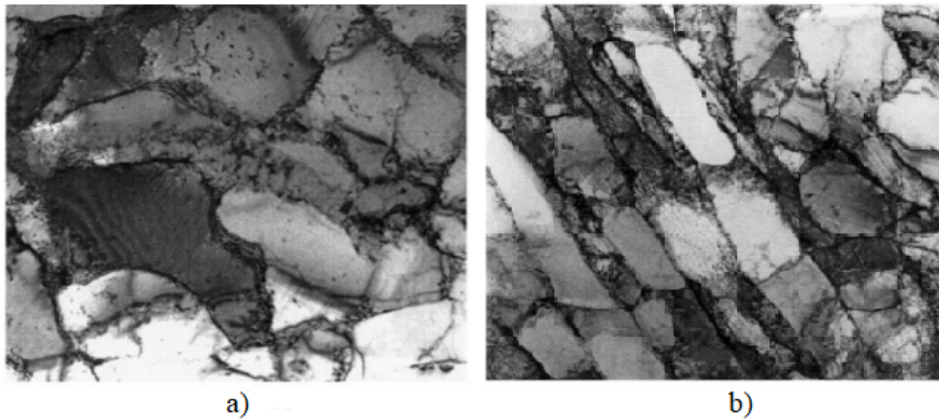
Figure 3.31: TEM micrographs of typical dislocation structures developed after plastic deformation in monotonic loading in a 1050-0 alloy: (a) uniaxial tension ϵ=0.12; (b) simple shear ϵ=0.30 [79].

a)   b)   c)
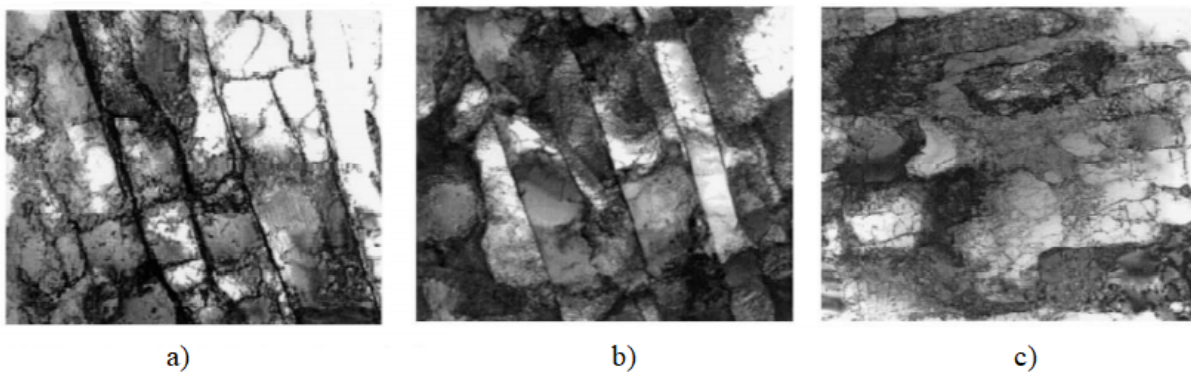
Figure 3.32: TEM micrographs of typical dislocation structures in a 1050-0 alloy developed after plastic deformation in TD uniaxial tension up to a strain of 0.14, followed by simple shear up to a strain of 0.15 in different directions with the Schmitt angle of the two step test indicated (a) 45° shear illustrating cell reorganization,ϕ=0.85 (b) 90° shear showing cell superimposition, ϕ=0 (c) 135° shear showing cell dissolution, ϕ=-0.85 [79].

In 2019, Qin et al. [124] investigated orthogonal strain path changes in AA3103 aluminium alloy. The tested AA3103 aluminium alloy was in a fully annealed condition with anisotropic properties, as the monotonic stress decreased as the angle from the rolling direction increased and the r-value had a maximum at 30-45° from the. The behaviour after orthogonal strain path changes was investigated both for tension-tension and rolling-tension. In the tension-tension test the specimens were prestrained to 8% with uniaxial tension in the rolling direction followed by tensile testing at every 15° from the rolling direction. The stress-strain curves for 0°, 45°, 60° and 90° from the rolling direction is seen in Figure 3.33 as the dashed lines. The rolling-tension test were performed with a rolling prestrain in TD followed by tensile testing parallel to RD.
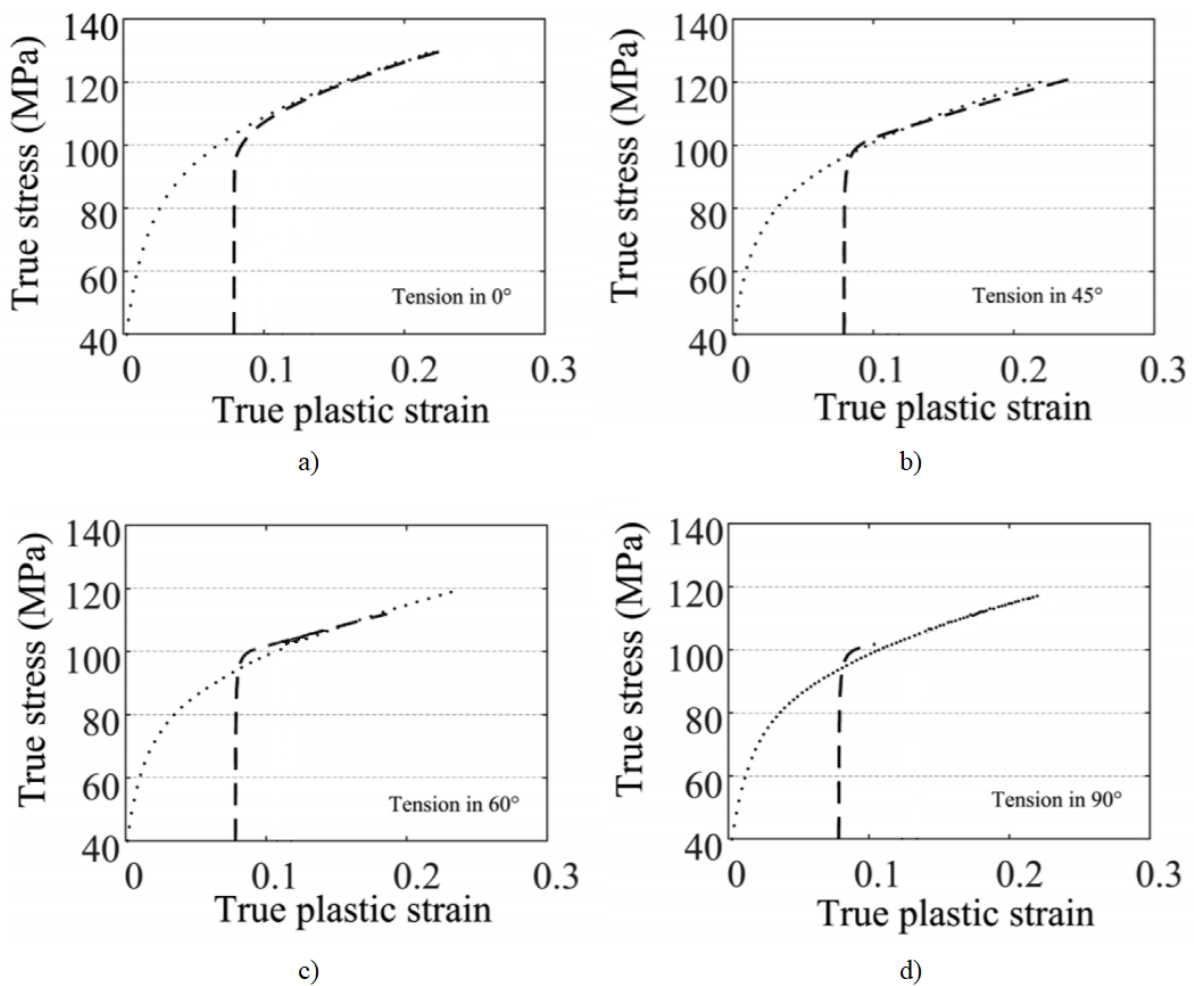
Figure 3.33: True stress-strain curves in uniaxial tension along a) 0°, b) 45°, c) 60° and d) 90° from the RD. Dotted lines represent the monotonic true stress-strain curve in the same direction as the reloading. Dashed lines represent tension tests with 8% pre-deformation in tension along the RD. All curves are plotted up to necking [124].

From the tension-tension tests, cross hardening was detected. The characteristic stress overshoots occurred at angles above 15° to the rolling direction while a reduction in necking

strain was observed for tests with an angle above 45° to the rolling direction. All tests resulted in permanent softening. For the rolling-tension tests, a consistent lower yield was observed, seen in Figure 3.34. The reduction in yield stress was reduced with increasing strain, and for the two largest strains, a hardening stagnation was observed. Further, the loading hardening rate converged towards the monotonic curve for all prestrains and the flow stress remained permanently lower than the monotonic curve. The authors did report some cross hardening in the rolling-tension tests, however it was overshadowed by an increased hardening rate and a lower initial yield resulting in cross softening.
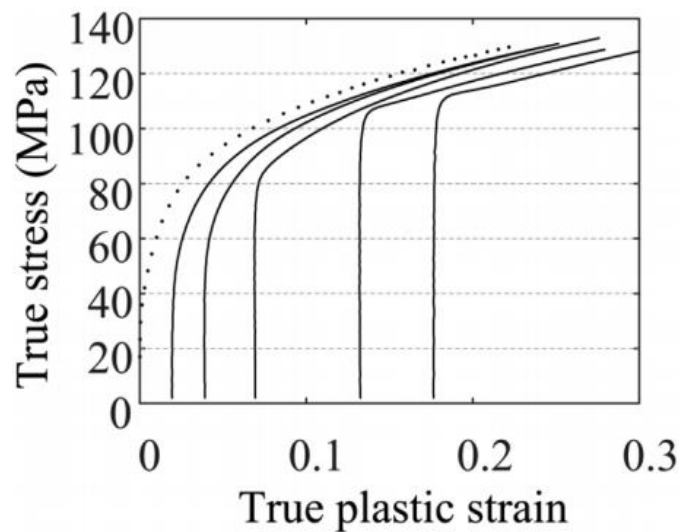
Figure 3.34: True stress-strain curves in tension along the RD after rolling in the TD to various strain levels and corresponding monotonic stress-strain curve. The true plastic prestrain by rolling is estimated by the von Mises strain. All curves are plotted up to necking [124].

By comparing the two tests, the authors observed that the hardening transients were not solely controlled by the Schmitt angle (i.e. the angle between the two straining direction). While both the rolling-tension tests and the tension-tension 60°-test had approximately the same Schmitt angle (close to 1), the two tests resulted in different behaviour. It was therefore concluded that more complex relations between the straining direction combined with influence by texture and slip system activation must be considered. The authors further discussed the effects from the dispersoids found in 3xxx alloys, as the dispersoids can cause a strong Bauschinger effect which is attributed to the reversibility of dislocation loops and structures formed around particles. It was suggested that the Bauschinger effect could weaken the stress overshoot as some slip systems can be reversed during orthogonal SPCs. However, it was concluded that an equal strong cross hardening effect would occur in the 3xxx alloy as in alloys without dispersoids, as the authors compared the observed cross hardening with previous work on 1xxx alloys.

3.7   Previous Work on AA3005

A characterisation of a 3005 aluminium alloy with similar composition was conducted by the author in 2019 prior to this thesis [2]. The alloy had a similar process history and composition as the alloy investigated in the present thesis. The alloy had an annealing temper of H27, thickness of 0.3 mm and a rolling reduction of 92%. The composition of the alloy is given in Table 3.1.

Table 3.1: Composition [2].

Material	Al	Mn	Fe	Si	Cu	Mg	Zn
AA3005	96.94	1.19	0.62	0.53	0.18	0.35	0.09

The characterization involved both a mechanical and microstructural analysis by conducting tensile testing, EBSD scans and texture measurements. The amount of Mn in solid solution was investigated by electrical conductivity measurements and an analysis on the dispersoids was conducted by BSE imaging. In addition to the characterization, an investigation on the heat exposure experienced during lacquering was also conducted by preforming flash annealing experiments. The heat exposed sample is referred to as flash annealed. The heat exposure was simulated by conducting heat treatments in two Nabertherm aircirculation ovens. The entire heating process as experienced during lacquering is given in Table 3.2. After each heat exposure, the material was quenched down to room temperature.

Table 3.2: Heat treatment.

	Oven 1	Time at room temperature	Oven 2	Time at room temperature
AA3005	230.6°C at 22 s	49.45 s	257.7°C at 22 s	49.45 s

The tensile tests were conducted in the rolling direction. The values for the E-modulus, uniform elongation, yield and ultimate tensile strength are given in Table 3.3 and the stress-strain curves are seen in Figure 3.35. It was observed that the uniform elongation was reduced after the heat exposure. A possible increase in yield strength was observed as well with the exception of the maximum measured yield strength for the as received material and the minimum measured yield for the flash annealed measured. The increase in ultimate tensile strength was not as distinctive.

Table 3.3: Results from tensile test conducted in the rolling direction [2].

Condition	Specimen	E-modulus [GPa]	S_y [MPa]	S_u [MPa]	e_u [mm/mm]
As received	1	68.0	195	208	0.0380
	2	71.2	198	212	0.0375
	3	68.0	195	208	0.0422
Flash annealed	1	74.0	205	214	0.0321
	2	71.2	202	211	0.0187
	3	68.5	198	206	0.0232
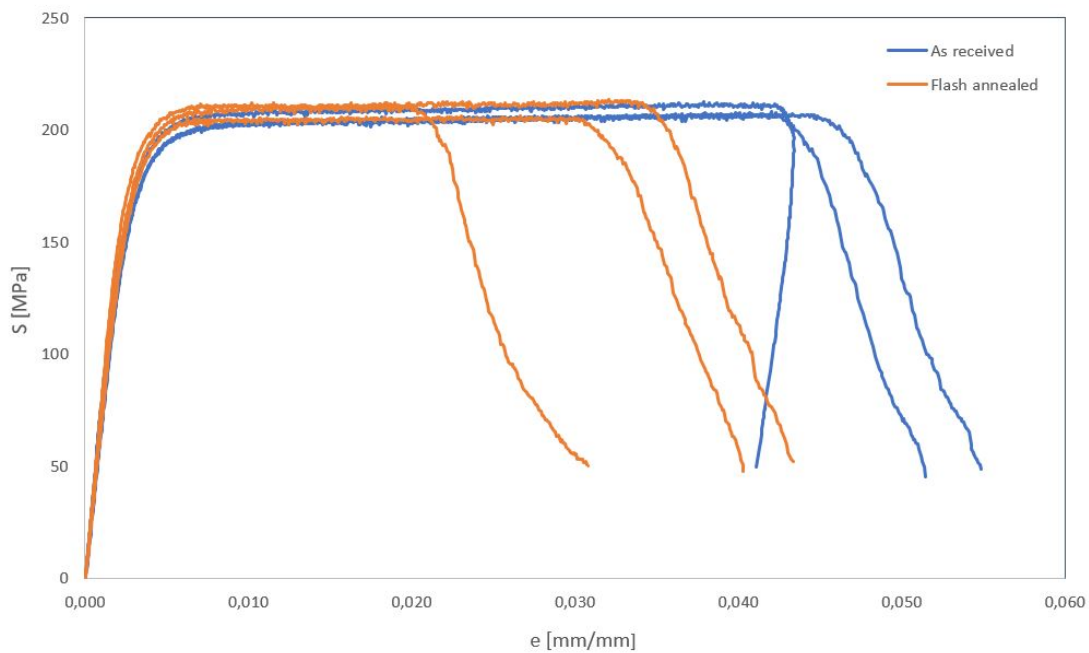
Figure 3.35: Engineering stress-strain curves tested in the rolling direction for AA3005. As received in seen in blue and flash annealed in red [2].

A summary of characteristics found by from the EBSD scans, electrical conductivity measurements and BSE imaging are seen in Table 3.4, 3.5 and 3.6, respectively. The original OIM-map together with the denoised OIM-map, fraction recrystallized and IQ-map are seen in Figure 3.36 and 3.37 for the as received sample and the flash annealed sample, respectively. The denoising and filtering of the OIM-maps were conducted by using MTEX in Matlab. The characterization revealed a typical deformation structure with small subgrains and elongated grains. Grains were characterized as recrystallized if the equivalent circle diameter (ECD) was above 2 µm, orientation spread was less than 2° and the fraction of HAGBs were (misorientation >15°) above 75%. The higher measured value in fraction recrystallized for the

flash annealed sample was attributed to an error of the characterization as some of the constituent particles had been characterized as recrystallized grains. The constituent particles are seen as the larger dark areas in the IQ-map. Only minor changes were seen between the as received and the flash annealed sample and no extended recovery or additional recrystallization was detected. The minor changes between the grain and subgrain sizes before and after flash annealing was attributed to local variations in the sheet, as two different samples were used. The IQ-map in Figure 3.37d revield grinding lines, which could affect the measured values.

Table 3.4: Grain size, subgrain size and fraction recrystallized [2].

Sample	Grain size [µm]	Subrain size [µm]	Fraction recrystallized [%]
As received	0.70	0.69	0.9
Flash annealed	0.66	0.65	1.5
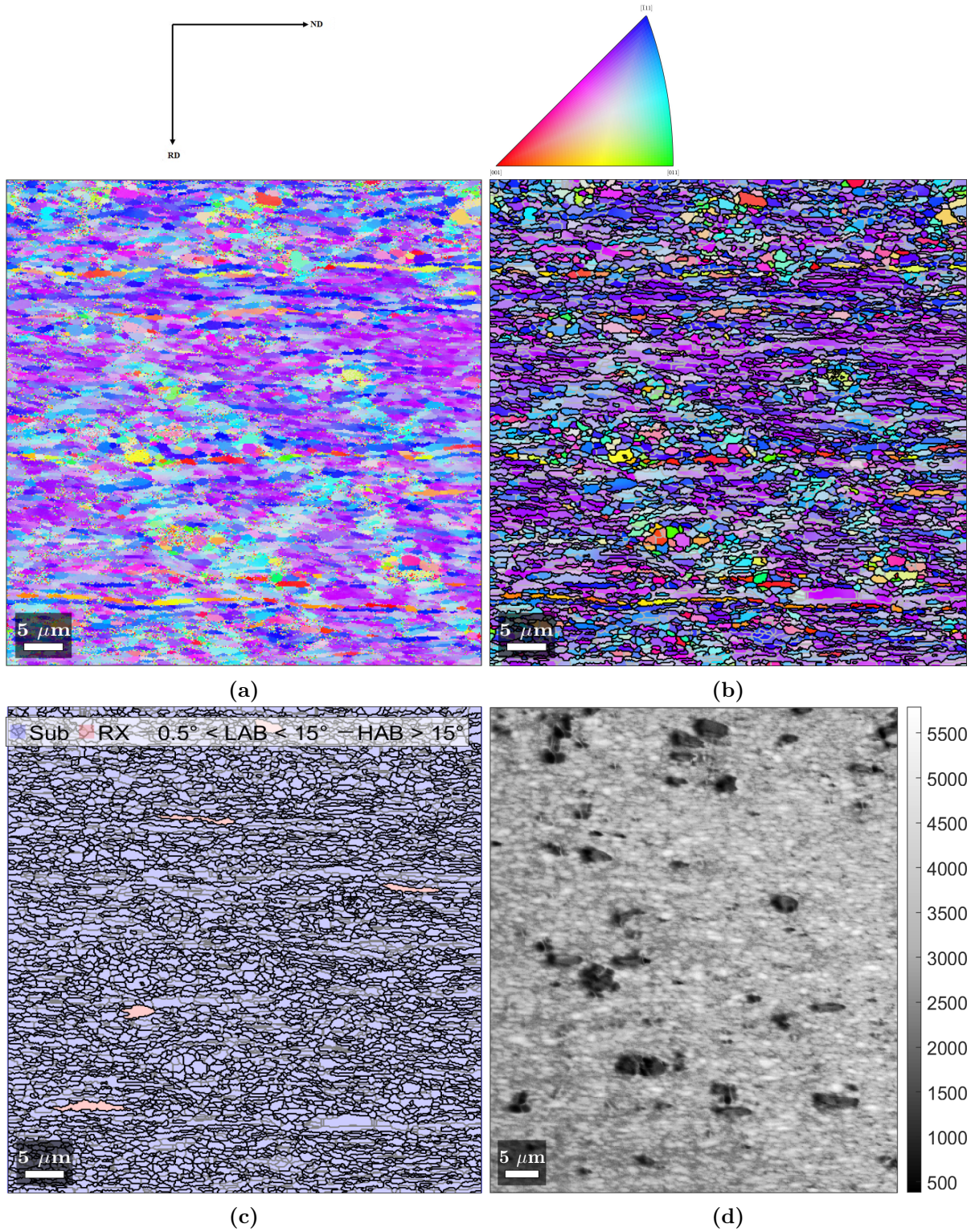
Figure 3.36: 92%CR H27 as received a) Original OIM-map b) denoised and filtered OIM-map with HAGB indicated by black boundaries and LAGB indicated in grey boundaries c) OIM-map with subgrain (Sub) and recrystallized grain (RX) indicated as characterized by MTEX d) IQ-map. The figure on the top left is the inverse pole figure indicating the grain orientation [2].
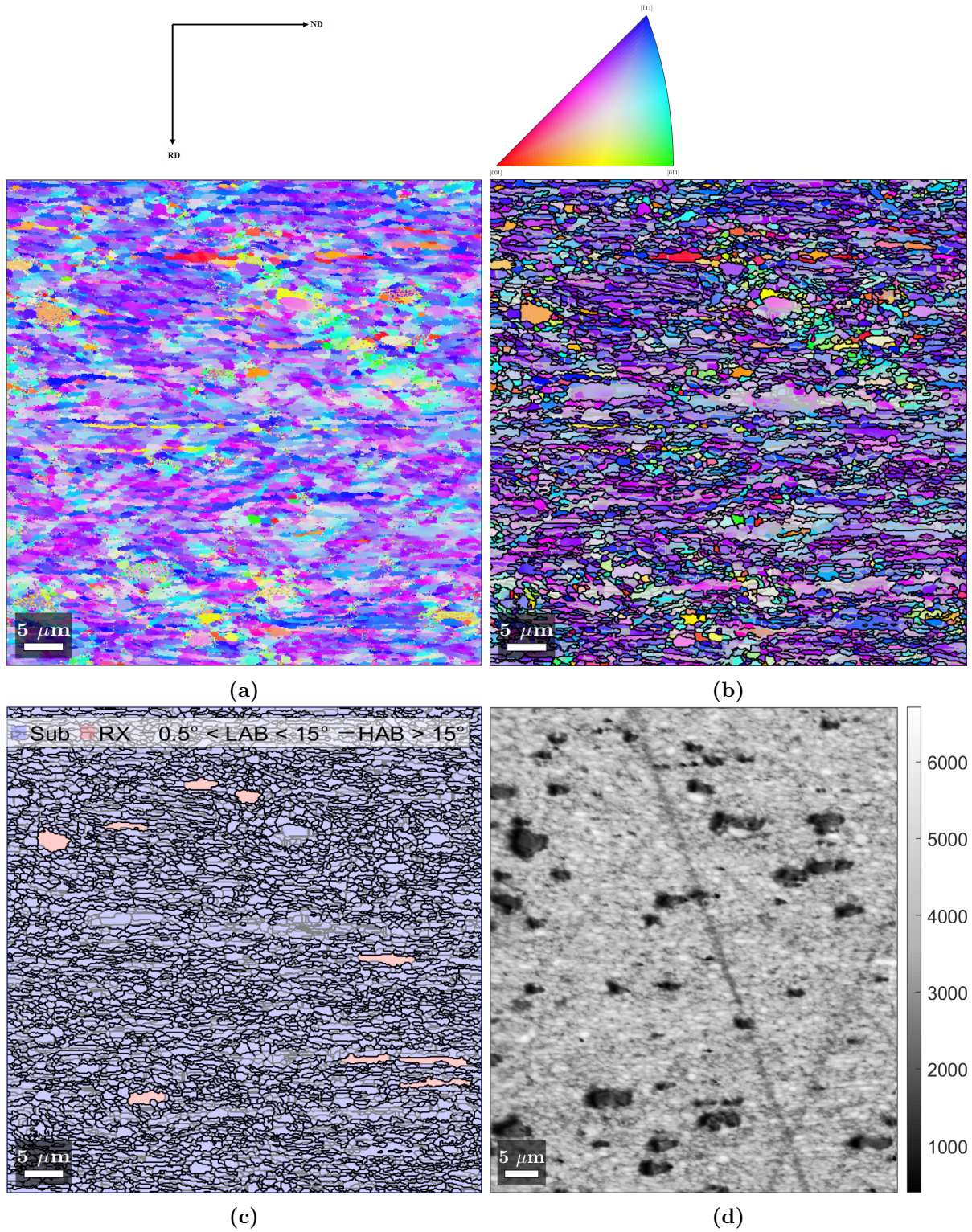
Figure 3.37: 92%CR H27 flash annealed a) Original OIM-map b) denoised and filtered OIM-map with HAGB indicated by black boundaries and LAGB indicated in grey boundaries c) OIM-map with subgrain (Sub) and recrystallized grain (RX) indicated as characterized by MTEX d) IQ-map. The figure on the top left is the inverse pole figure indicating the grain orientation [2].

The dispersoid analysis and conductivity measurements were unable to detect any precipitation or growth of dispersoids. The dispersoid distribution was similar both before and after annealing, with a peak between 0.1 µm and 0.125 µm and all samples had its highest frequency of dispersoids size between 0.075 µm and 0.150 µm. The large reduction in particle density and area after flash annealing was contributed to poor imaging rather than dissolvement of dispersoids, as no change was observed in conductivity. The BSE images and distributions from the particle analysis are seen in Figure 3.38 and 3.39, respectively.

Table 3.5: The mean measured electrical conductivity and the calculated Mn in solid solution by Equation 4.3 with standard deviation [2].

Condition	EC [MS/m]	Mn_{ss} [wt%]
As received	26.16 ± 0.03	0.320 ± 0.001
Flash annealed	26.14 ± 0.04	0.321 ± 0.002

Table 3.6: Particle diameter, particle density and particle density [2].

Condition	Sample	Diameter δ_{ECD} [µm]	Particle density [$1/\text{mm}^2$]	Particle area [%]
As received	1	0.158	$1.2 \cdot 10^6$	2.6
	2	0.157	$1.1 \cdot 10^6$	2.5
Flash annealed	1	0.156	$0.9 \cdot 10^6$	2.0
	2	0.146	$0.5 \cdot 10^6$	0.9
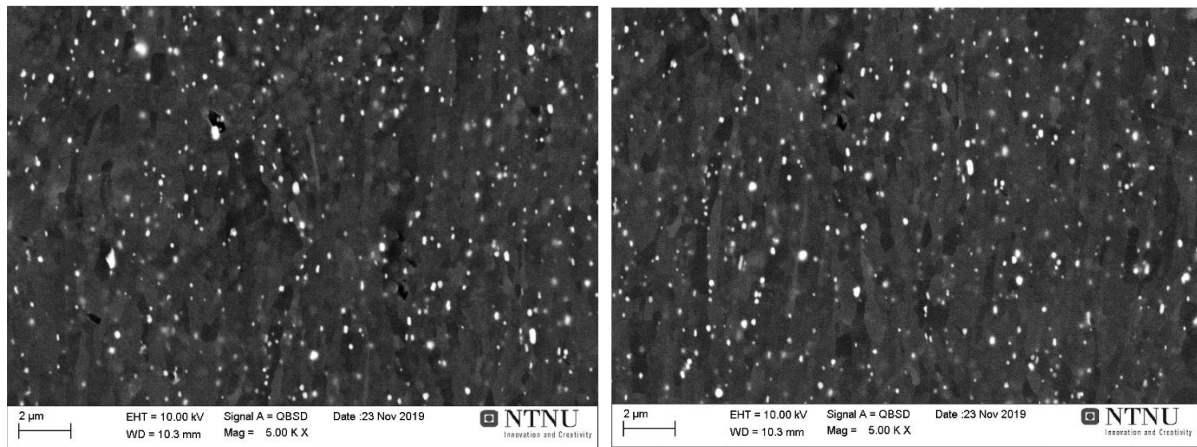
(a)   **(b)**
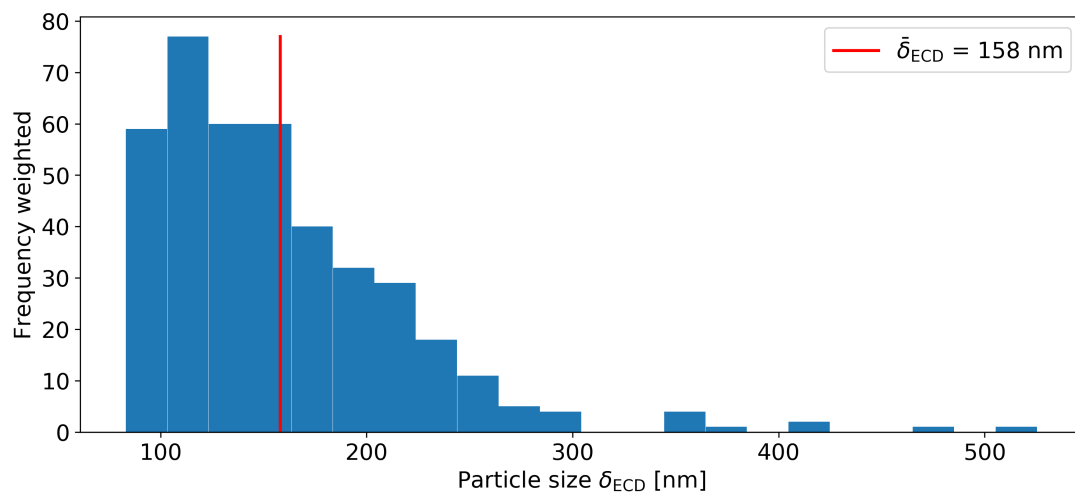
(c)
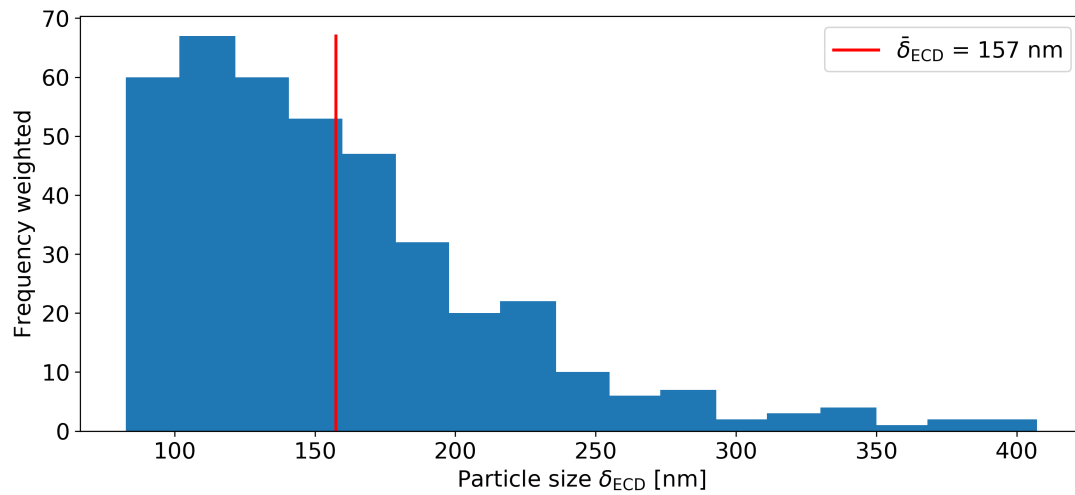
(d)

Figure 3.38: BSE images of the as received AA3005 alloy in (a) sample 1 and (b) sample 2 and their respective particle distribution in (c) and (d) [2].

81
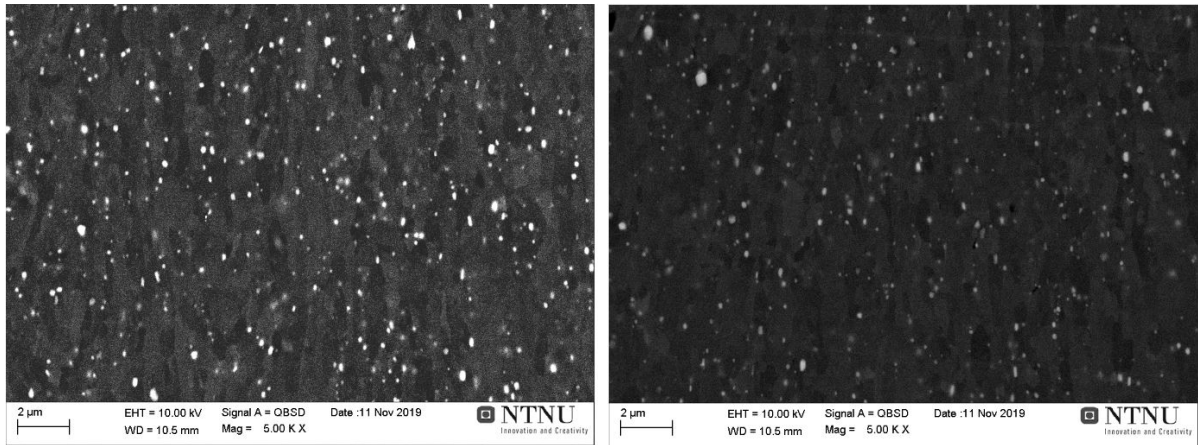
(a)

(b)
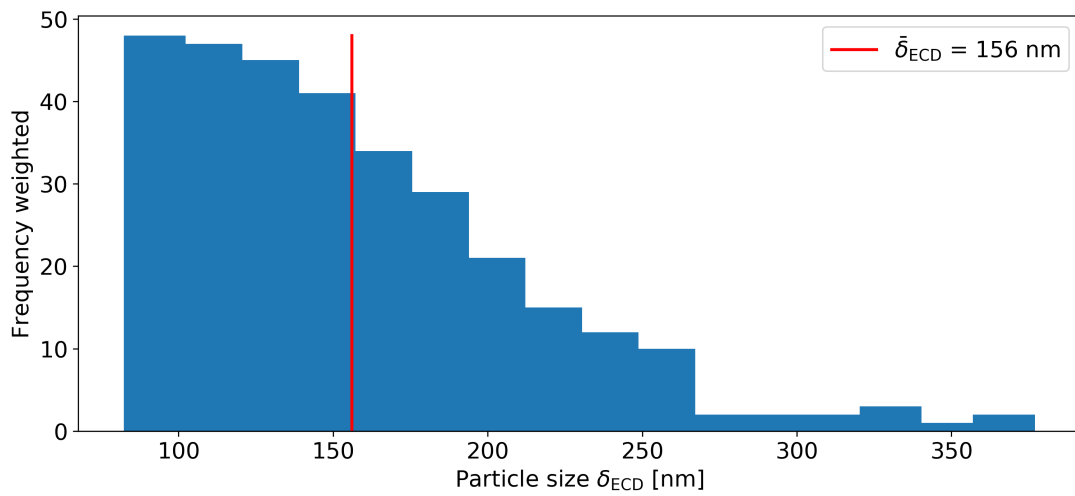
(c)
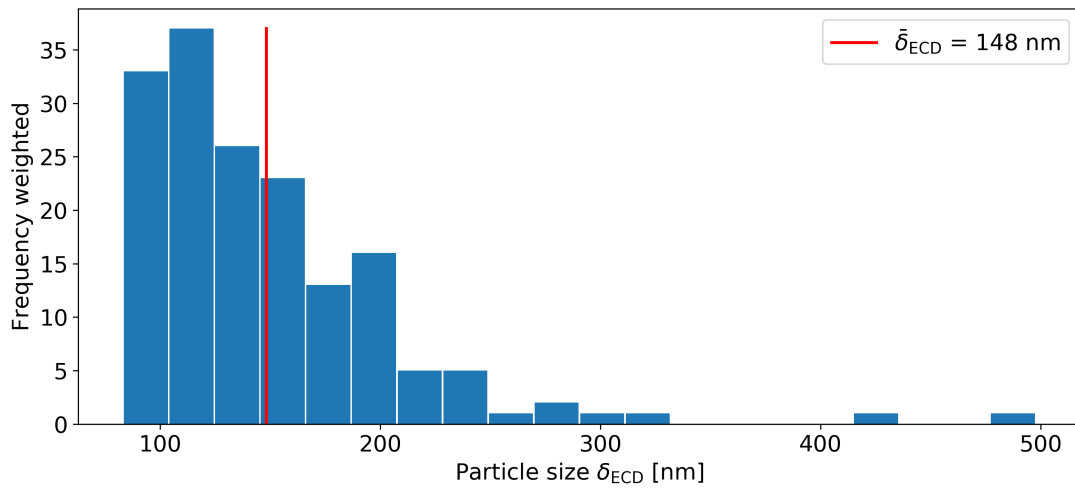
(d)

Figure 3.39: BSE images of the as flash annealed AA3005 alloy in (a) sample 1 and (b) sample 2 and the their respective particle distribution in (c) and (d) [2].

The result from the texture measurements are seen in Figure 3.40 with the calculated volume fractions of the texture components in Figure 3.41 which were calculated by using MTEX in Matlab. A typical cold rolled texture was observed both before and after flash annealing and only minor changes were seen in the recrystallization components. The increase recrystallization components seen in the flash annealed sample was attributed to the variations within the alloy sheet as two samples was used for texture measurements. It was concluded that no recrystallization had occurred.

(a) As received
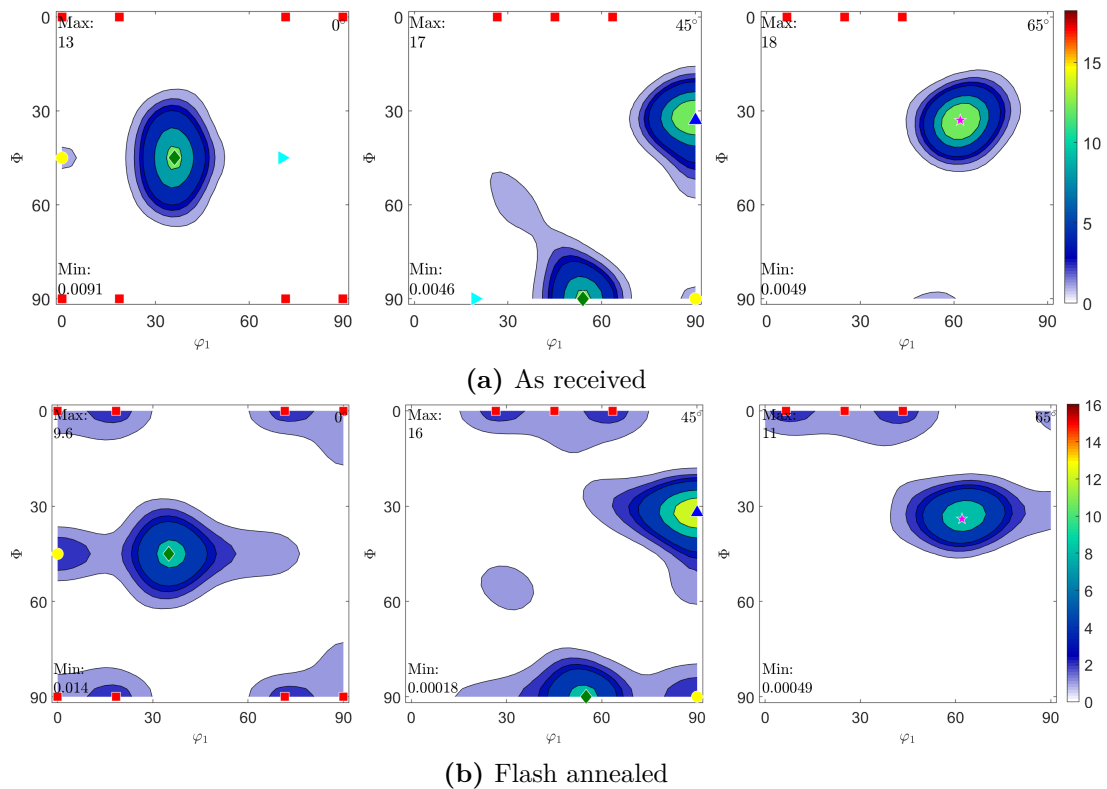
(b) Flash annealed

Figure 3.40: ODF sections 0°, 45°, 65° for the as received and flash annealed sample AA3005 alloy. Cube and ND-rotated Cube components are marked by red squares, Goss by yellow circles, Brass by green squares, Copper by blue triangles, P-texture by light blue triangles and S by pink stars [2].
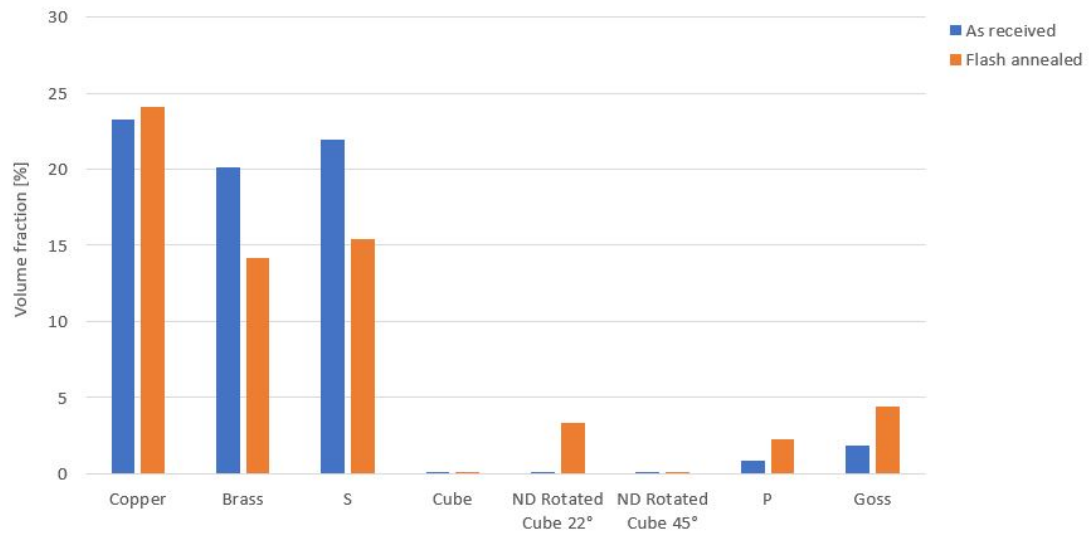
Figure 3.41: Volume fraction of the texture components for the as received and flash annealed AA3005 material [2].

4   Experimental

In the following section, the material and the experimental procedures are presented. First, the composition and prior treatment of the as received AA3005 is described, followed by the methods for tensile testing and electrical conductivity measurements. The last part describes the SEM and sample preparation.

As the access to laboratories were restricted due to COVID-19, only a limited amount of the planned experiments was performed. Initially, a characterization of the material in terms of microstructure, texture and an analysis on the dispersoids combined with further flash annealing experiments were planned but have not been conducted. As the present work is the continuation of the specialization project, the results from the characterisation and flash annealing experiments on a similar AA3005 alloy has been used in this thesis, given in Section 3.7.

4.1   Delivered Material

In the present thesis, an AA3005 alloy has been investigated. The alloy was produced by Hydro Aluminium Rolled Products Holmestrand with a composition as given in Table 4.1.

Table 4.1: Composition.

Material	Mn	Fe	Si	Cu	Mg	Zn	Al
AA3005	1.13	0.57	0.45	0.17	0.31	0.10	Balance

In the present thesis material from one coil was tested, referred to as sample nr 1 in Appendix A. Based on previous mechanical testing conducted by Hydro Aluminium Rolled Products Holmestrand, this sample was chosen for further investigations as is had the largest increase in strength after lacquering as seen in Appendix A, with an increase in yield strength at 15 MPa and increase ultimate tensile strength at 10 MPa.

The as received material was pre-heated, rolled and annealed by Hydro Aluminium Rolled Products Holmestrand. Subsequent to DC-casting, the alloy heating up to 570°C for 12-15 hours followed by hot rolling down to 3.5 mm. Cold rolling was conducted in five steps, reducing the thickness down to approximately 0.3 mm, corresponding to a cold reduction of 92% or logarithmic strain (ϵ) of 2.5. The sheets were further annealed at 216-224°C for 3 hours before cooled down to room temperature, achieving a temper of H27. The H2X indicates that the material has been strain hardened and partial annealed, while the X indicates the final level of cold work. H28 indicate a full hard temper, while H26 is partially annealed to a strain hardening of about 75% [125]. The delivered material therefore has an effective degree of strain hardening above 75%.

The lacquering process include a mechanical application of the coat on the sheet by moving it through the process by the ends of the coil (in the rolling direction). The drying of the lacquer consist of a two step isothermal heating process in ovens, as illustrated in Figure 2.2. The first heating exposure was conducted at approximately 232°C for 19 seconds followed water quenching down to room temperature. The second oven had a temperature of 253°C, where the sample was heated for 19 seconds followed by water quenching down to room temperature. The lacquer was applied on both sides of the sheet, as illustrated by the dark areas in Figure 4.1.

All samples were collected in the centre of the width of the coil to avoid rolling defects during straightening stage of the process. Furthermore, both blank and lacquered samples were collected at the same region of the coil before and after lacquering. The investigated annealed material without lacquer is termed blank in the present thesis while the coated material is termed lacquered.
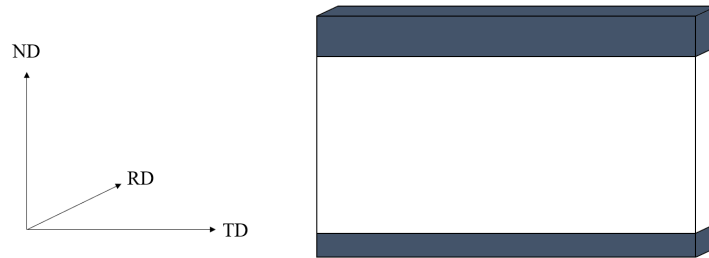
Figure 4.1: Illustration of a sheet with lacquer on both sides in the ND-TD plane.

4.2   Tensile Testing

Tensile tests were performed to characterize the mechanical properties of the blank and lacquered alloy, including yield strength, ultimate tensile strengthening, uniform elongation, E-modulus and anisotropy. In the present thesis, tensile specimens were taken out both in the rolling and transverse direction of the sheets. The lacquered material was tested with the lacquer on. SEM and digital caliper measurements were conducted to determine the metal thickness and lacquer thickness. An average of 3 specimens were tested in each direction. The geometry of the tensile specimens is given in Figure 4.2.
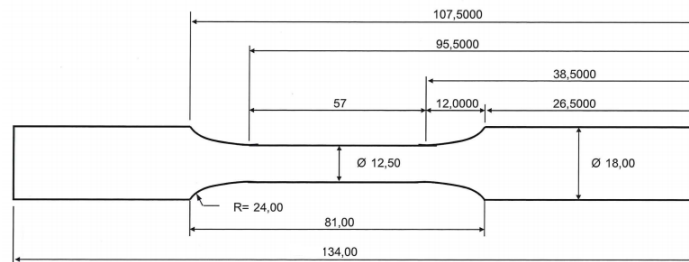
Figure 4.2: Geometry of tensile test.

The tests were conducted on a MTS 810 testing machine at a crosshead speed of 2 min/mm. The elongation was measured with clip-on extensometers both in the longitude and width direction of the tensile specimens. The different strain direction relative to a tensile testing specimens are illustrated in Figure 4.3.
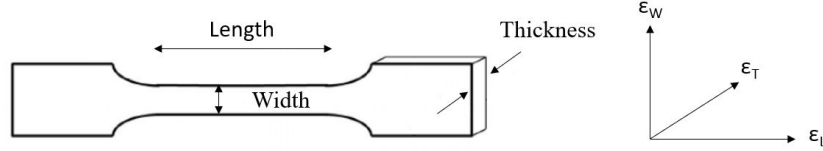
Figure 4.3: Schematic illustration of a tensile specimen with strain directions.

4.2.1   Anisotropy

The anisotropy of the specimens was calculated using the width and longitudinal strain found from the tensile tests. The slope of the plastic ϵ_w-ϵ_l is related to the plastic strain ratio by:

$$r = \frac{q}{1-q} \qquad (4.1)$$

Where q is the slope of ϵ_w-ϵ_l which is found by converting the engineering stress and strain values from the tensile tests into true stress and strain by the relationships given in Equation 2.29 and 2.30. Further, the plastic strains were calculated from Equation 2.33 and 2.34. These values are denoted as r_1. A Poisson's ratio of 0.33 was used to calculate the plastic width strain.

In addition, the plastic strain ratio was found using the change in thickness and width of the tensile specimens according to Equation 2.31. These values are denoted as r_2.

4.3   Electrical Conductivity

The electrical conductivity, σ, indicate a materials capability of conducting an electrical current and is the reciprocal of the resistivity, ρ [72]. The presence of alloying element will distort the lattice and increase the resistivity of a material. Measurements of conductivity are therefore preformed to measure the level of elements in solid solution. An increase or decrease in in conductivity indicate precipitation or dissolution of dispersoids respectively [72, 106, 126].

As described by Altenpohl [127], the relationship between electrical conductivity and the solid solution content of Mn, Si and Fe can be expressed by neglecting the temperature dependent

term in the Matthiessen's rule, given by:

$$\frac{1}{\sigma} = 0.0267 + 0.036\text{Mn}_{ss} + 0.032\text{Fe}_{ss} + 0.0068\text{Si}_{ss} \tag{4.2}$$

Where Mn, Fe and Si are the amount of the alloying element in solid solution in wt% in the alloy. While it is impossible to separate the contribution from the three alloying elements, equation 4.2 can be used to estimate the amount of Mn in solid solution. As seen, the contribution from Si is low compared to those from Mn and Fe, and can be neglected. In addition, the solubility of Fe in aluminium is low and its contribution can therefore be disregarded [102]. The following equation may therefore be used to estimate the amount of Mn in solid solution.

$$\frac{1}{\sigma} = 0.0267 + 0.036\text{Mn}_{ss} \tag{4.3}$$

Upon annealing, Equation 4.3 can used to follow the evolution in Mn in solid solution and indicate precipitation or coarsening of Mn-bearing dispersoids.

In the present investigation, a Foerster Sigmatest 2.069 conductivity meter was used. Measurements were performed by mounting the probe from the conductivity meter on the flat blank surface of the samples on the RD-TD plane. 10 measurements were performed. As described by the operation manual for the conductivity meter, the thickness of the material affects the accuracy of the measurements. The effective penetration depth δ_{eff} can be determined from the frequency and the electrical conductivity as expressed in Equation 4.4:

$$\delta_{\text{eff}} = \frac{503}{\sqrt{\sigma \cdot f}} \tag{4.4}$$

Where the effective penetration depth is given in mm, the electrical conductivity σ is given in MS/m and the frequency f in Hz. The frequency was set to 960 Hz to ensure high accuracy of the measurements. As the conductivity is temperature sensitive, the instrument was re-calibrated with two reference samples between measurement to ensure accurate measurements.

4.4 Scanning Electron Microscope

A SEM produced images using an incident electron beam which scans across the surface of a sample. As the generated primary electrons from the incident beam interacts with the specimen, different signals are emitted and are detected by different detectors in the SEM. Topographical investigations of the surface of the sample are conducted by using secondary electrons. Secondary electrons are the result of inelastic interactions between primary electrons and atoms near the surface in the sample and are detected by the Everhart-Thornley detector [128]. In the following

thesis, secondary electron is used to find the thickness of the lacquer on the sample.

For identifying phases, backscattered electrons are commonly used. Backscattered electrons are electrons originating from the electron beam which have collided with atoms in the sample. The electrons are reflected from the sample by elastic scattering interactions, detected by a solid-state BSE detector. Heavier elements (high atomic number) scatter stronger than lighter elements, creating a stronger signal and appearing brighter in the image, known as Z-contrast. In addition, changes in the crystal lattice orientation causes the primary electrons to be channeled in and out of the sample. With a high atomic density near the surface, primary electrons can interact strongly with the lattice and will be reflected. With a lower atomic density or at a changed angle (from the incident beam), electrons will penetrate deeper into the material and have a lower possibility for contribution to the BSE signal [8]. This phenomenon creates a contrast known as channelling contrast which makes it possible to detect orientation differences between grains and it becomes possible to study the location of precipitation of dispersoids on the deformation structure [10].

Diffraction of backscattered electrons are used for EBSD. EBSD is typically used for acquiring microtexture and crystallography data from materials. As the electron beam hits a tilted sample, electrons are elastically scattered, and a fraction of the reflected electrons becomes diffracted according to Bragg's Law. A phosphor screen collects the scattered BSE, resulting in a Kikuchi pattern. The pattern gives the atomic planes of a crystal at a given position and are detected by a camera behind the phosphor screen.

The sample preparation for SEM is described below.

1. The sample was cut down to 20 x 10 mm and cold mounted in Epofix Cold-setting Resin. The ND-TD plane, as illustrated in black in Figure 4.4, was grinded from a 500 to 4000 mesh size with SiC paper.

2. The sample was further polished on 3 µm and 1 µm polishing cloth with their respective diamond polishing suspension.

3. The final step of the preparation was vibration polishing for 1 hour on a frequency of 70Hz. The vibration polishing was conducted on a Buehler VibroMet 2. The vibration polishing was conducted to remove the top deformed layer induced by mechanical polishing as the sample was initially intended for EBSD scanning.
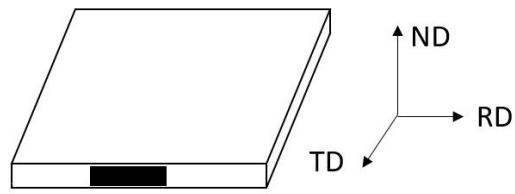
Figure 4.4:   Schematic drawing of rolled sheet with directions.

5   Results

In the following section, the thickness measurements of the lacquered samples are presented followed by results from the tensile tests of the blank and lacquered material. Last, the mean conductivity measurement is presented for the blank material.

5.1   Thickness Measurements of the Lacquered Material

As the lacquered material was tested with the lacquer on, the thickness of the lacquer had to be determined. The thickness profile along the transverse direction of the sheets were measured to ensure correct thickness measurements for the tensile tests and to investigate the thickness range across the sheet. Two sheets were measured, which were from each side of the centre region of the coil.

The total thickness is defined as the thickness of the alloy sheet plus the thickness of the lacquer. The mean thickness were 0.335 mm and 0.334 mm for the sheet 1 and sheet 2, with a range in thickness across the sheet of 0.017 mm and 0.014 mm respectively.
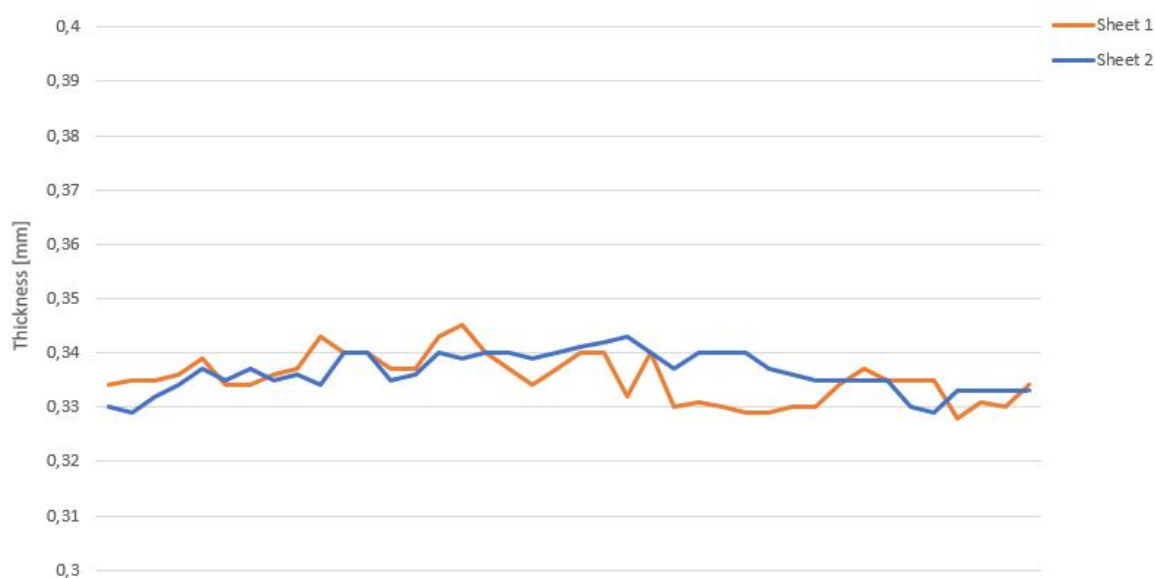
Figure 5.1: The total thickness profile for two sheets of lacquered AA3005 parallel to TD.

5.2 Thickness Measurements of the Lacquer in SEM

As mentioned in Section 4.4, the lacquered material is coated on both sides of the sheet where the layers have different thickness. SEM imaging was utilized to detect and measure the variation in lacquer thickness.

The SEM images of the lacquer on the top side of the sheet are given Figure 5.2 and is seen as the porous layer on top of the alloy. As observed, the thickness does vary across the sample with a range of approximately 1 µm. The mean thickness, based on the measurements from Figure 5.2, is 0.0265 µm. The coat on the bottom of the sample was difficult to distinguish from the epoxy which the material was mounted in. In Figure 5.3, a diffuse layer with thickness of 1 to 2 µm may possible be the lacquer. However, it was not possible to get accurate measurements.

(a)

(b)

(c)

(d)
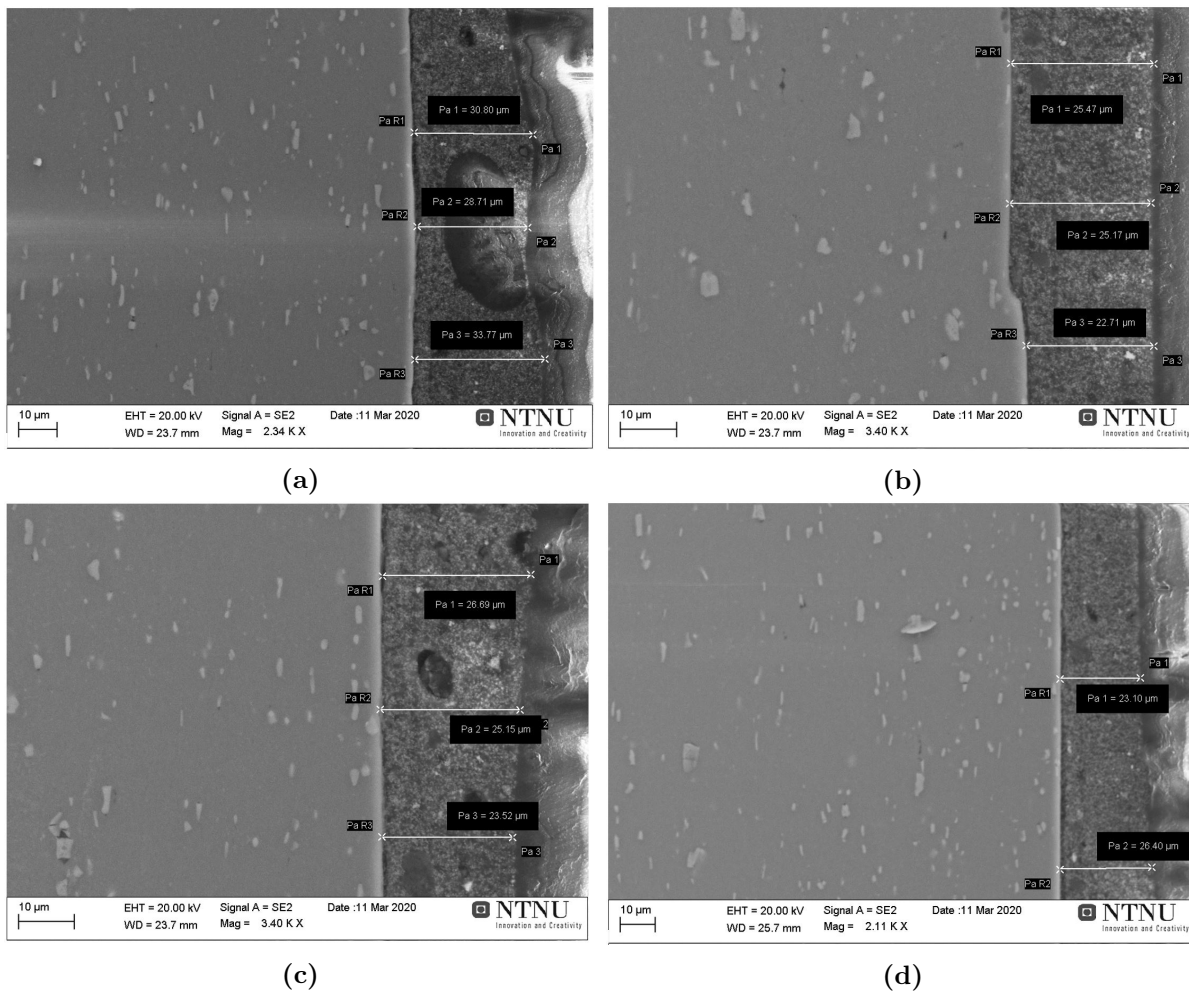
Figure 5.2: SEM images of the lacquer on the top of the sheet.
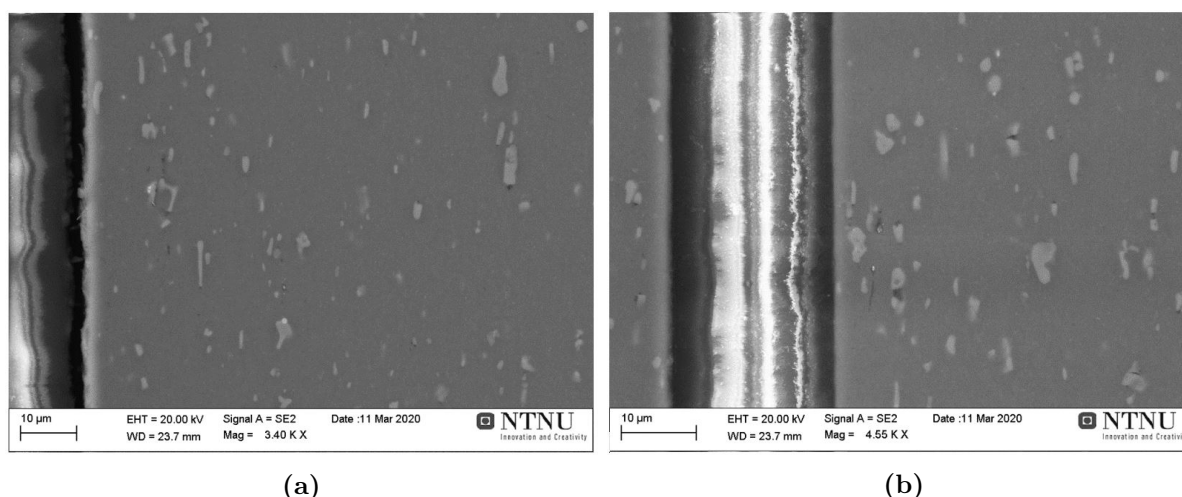
Figure 5.3: SEM images of the lacquer on the bottom of the sheet.

5.3   Tensile Testing

Tensile tests were performed to determine mechanical properties such as the E-modulus, uniform elongation, tensile and yield strength. The values from the tests conducted in RD and TD are given in Table 5.1 and Table 5.2, respectively. The lacquered samples were tested with lacquer on and thickness of the lacquer was subtracted from the total thickness. The thickness of the blank samples was 0.304 mm while the thickness of the lacquered samples were set to 0.307 mm based on the thickness measurements from Section 5.1 and 5.2.

Table 5.1: Results from tensile tests conducted in the rolling direction.

Surface condition	Specimen	E-modulus [GPa]	S_y [MPa]	S_u [MPa]	e_u [mm/mm]
Blank	1	70.2	194	207	0.0247
	2	70.4	202	215	0.0354
	3	70.2	197	209	0.0233
Lacquered	1	70.2	202	211	0.0203
	2	70.1	199	210	0.0221
	3	70.0	195	204	0.0165

From the specimens tested in the rolling direction, it is seen that the mean yield strength before and after lacquering is 198 MPa. There is a similar variation in values for the blank and lacquered material, with a range of 9 and 7 MPa respectively. The mean ultimate tensile strength levels are 210 MPa for the blank specimens and 208 MPa for the lacquered specimens, both with a range in values at 7-8 MPa. The uniform elongation is consistently lower after lacquering, where the minimum reduction in strain between the surface conditions is 0.001 [mm/mm].

Table 5.2: Results from tensile test conducted in the transverse direction.

Surface condition	Specimen	E-modulus [GPa]	S_y [MPa]	S_u [MPa]	e_u [mm/mm]
Blank	1	70.1	204	217	0.0109
	2	67.5	190	203	0.0127
	3	70.1	210	224	0.0092
Lacquered	1	70.1	211	221	0.0071
	2	70.1	212	222	0.0071
	3	70.1	212	223	0.0068

From the specimens tested in the transverse direction, it is seen that the mean yield strength is 201 MPa for the blank material and 212 MPa for the lacquered material. The mean ultimate tensile strength is 214 MPa for the blank material and 222 MPa for the lacquered material. While the lacquered specimens are consistent, the range in measured values for the blank material is at 20 MPa both for the yield and tensile strength. The uniform elongation is consistently lower after lacquering, where the minimum reduction in uniform elongation between the surface conditions is 0.002 [mm/mm].

The engineering stress-strain curves for specimens tested in the rolling direction and transverse direction are given in Figure 5.4 and 5.6. Enlarged sections of the stress-strain curves are given in Figure 5.5 and 5.7.
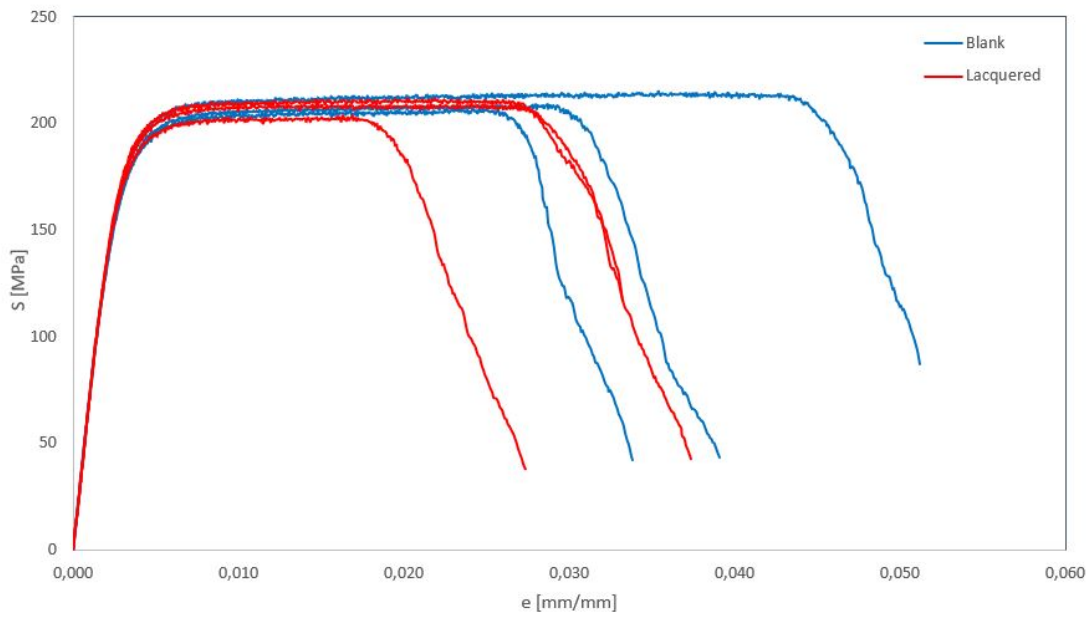
Figure 5.4: Engineering stress-strain curves for blank and lacquered specimens tested in the rolling direction. Blank samples in blue and lacquered in red.
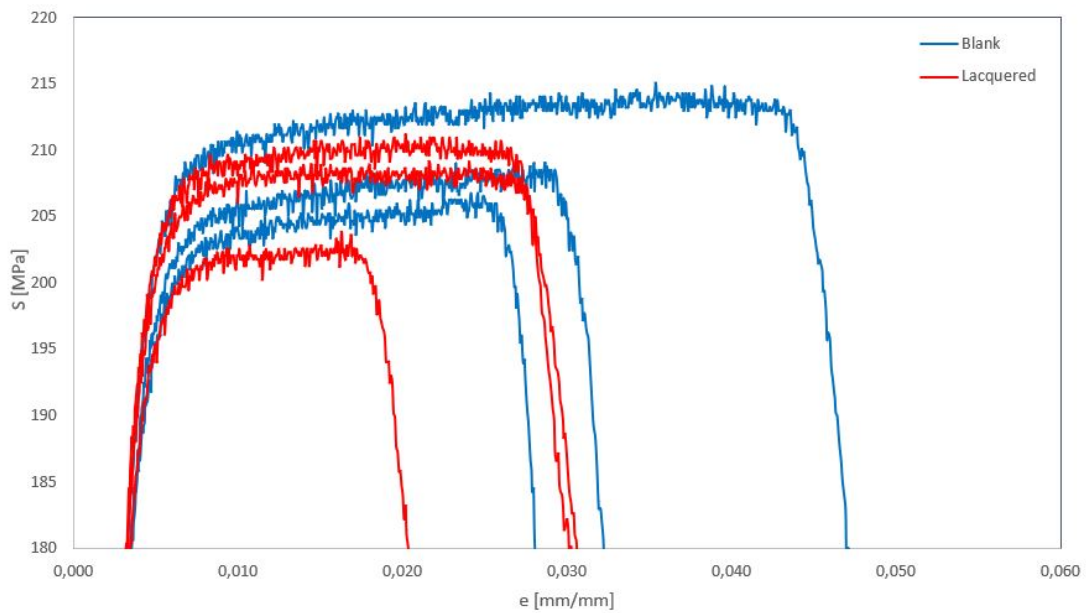
Figure 5.5: Enlarged section of the engineering stress-strain curves for blank and lacquered specimens tested in the rolling direction. Blank samples in blue and lacquered in red.

95
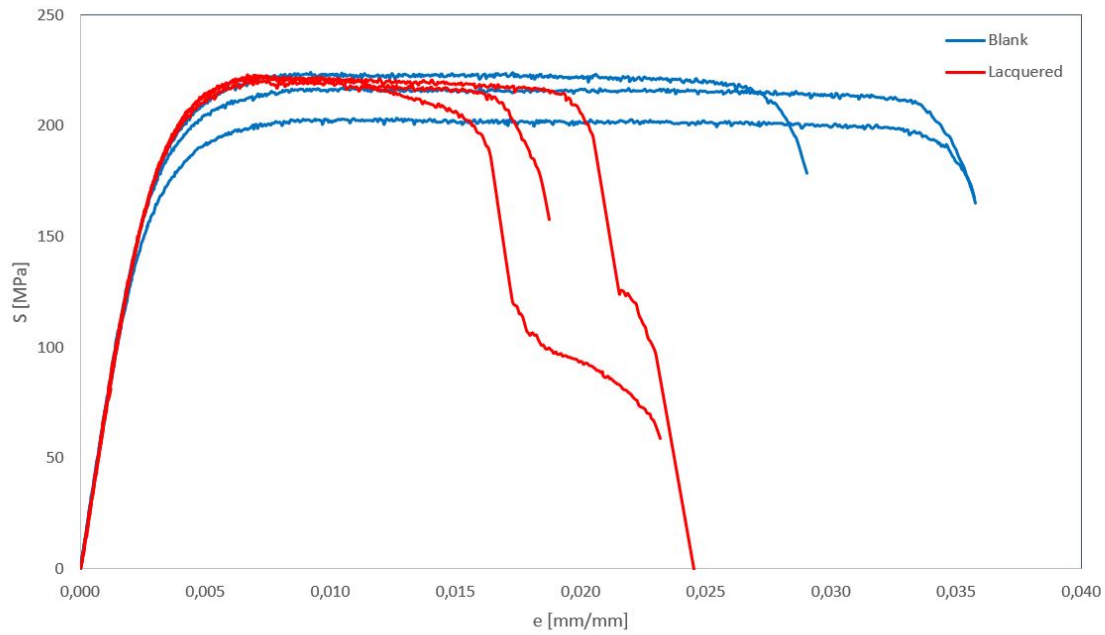
Figure 5.6: Engineering stress-strain curves for blank and lacquered specimens tested in the transverse direction. Blank samples in blue and lacquered in red.
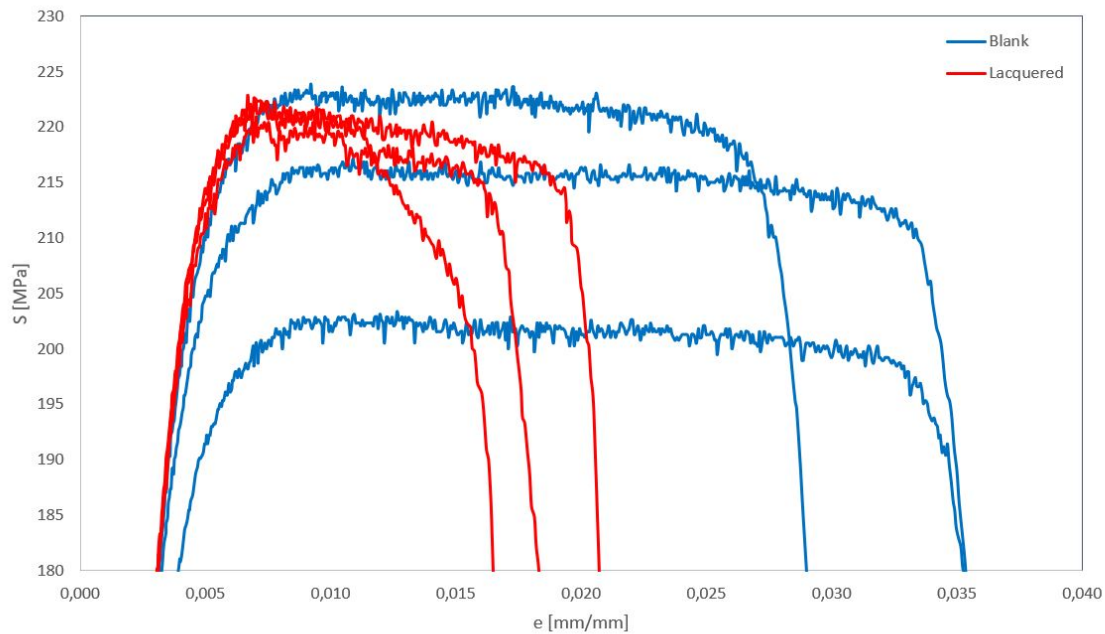
Figure 5.7: Enlarged section of the engineering stress-strain curves for blank and lacquered specimens tested in the transverse direction. Blank samples in blue and lacquered in red.

The tensile specimens after fracture in both testing directions are seen in Figure 5.8 and Figure 5.9. The grey specimens are the blank material, while the white specimens are lacquered. Necking has occurred at a similar position in the specimens within a given testing direction, except for the blank specimen denoted 3 in the transverse direction seen in Figure 5.9.
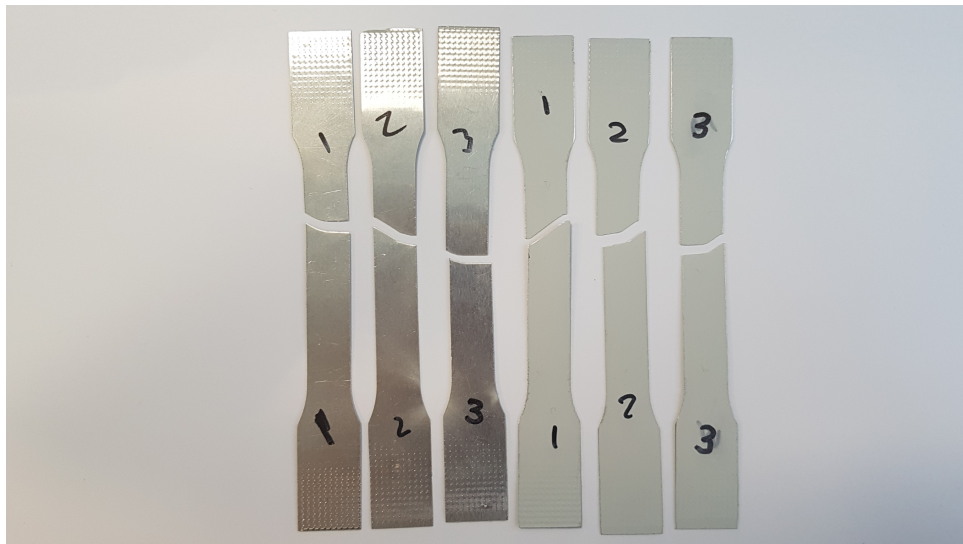
Figure 5.8: Tensile specimen tested in the rolling direction.
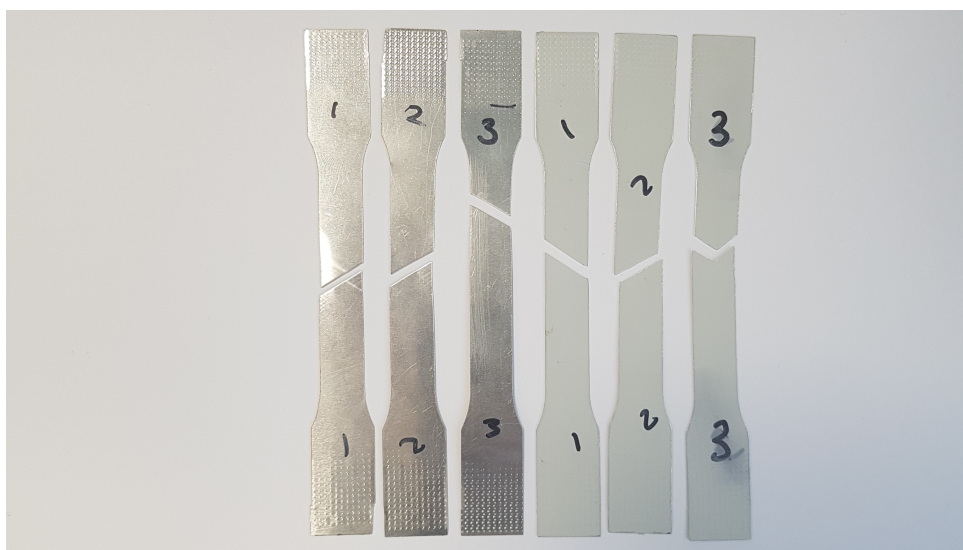
Figure 5.9: Tensile specimens tested in the transverse direction.

5.3.1   Accuracy of Result

As these sheets are thin, some uncertainty in the mechanical values are to be expected. A measuring error of 0.01 mm from the digital caliper corresponds to a 3% change in the initial cross section of the tensile specimen which will result in an increase or lowering of the stress-strain curve with 7 MPa.

5.4 Anisotropy

The plastic strain ratio values for the specimens tested in rolling and transverse direction are given in Table 5.3 and 5.4 respectively. As denoted in Section 4, the r_1-values were calculated from the contraction ratio q from the plastic ϵ_w-ϵ_l curve, while the r_2-values were found measuring the change in width and thickness of the tensile specimens and further calculated according to Equation 2.31. The specimens tested in the transverse direction have r-values above 1 while the blank material have r-values below 1.

Table 5.3: The contraction ratio q and plastic strain ratio r_1 and r_2 for the specimens tested in the the rolling direction.

Surface condition	Specimen	q	r$_1$	r$_2$
Blank	1	0.36	0.57	0.71
	2	0.36	0.57	0.44
	3	0.35	0.53	0.56
Lacquered	1	0.34	0.52	0.57
	2	0.36	0.57	0.75
	3	0.34	0.52	0.56

Table 5.4: The contraction ratio q and plastic strain ratio r_1 and r_2 for the specimens tested in the transverse direction.

Surface condition	Specimen	q	r$_1$	r$_2$
Blank	1	0.58	1.36	1.22
	2	0.59	1.41	1.21
	3	0.56	1.28	1.06
Lacquered	1	0.57	1.34	1.50
	2	0.58	1.28	1.13
	3	0.57	1.32	1.65

5.5   Electrical Conductivity

The conductivity measurements for the blank sample are presented in Table 5.5 together with the estimated amount of Mn in solid solution according to Equation 4.3. Conductivity measurements were not performed on the lacquered material, as the lacquered was not been removed from the material.

Table 5.5: Mean conductivity measurement from the sigmameter with standard deviation and the calculated amount of Mn in solid solution.

Sample	EC [MS/m]	Mn_{ss} [wt%]
Blank	26.24 ± 0.03	0.317 ± 0.001

6   Discussion

In the present thesis, the aim has been to investigate the possible influences from lacquering process on a 3005 aluminium alloy that can contribute to evolution in mechanical behaviour. The primary objective has been to investigate the influence of the additional heat exposure and hardening from strain path changes. In the following section, mechanisms that can influence strength and uniform elongation is discussed in terms of reviewed literature, the results obtained from the specialization project and from the mechanical testing and the electrical conductivity measurements conducted in the present work.

6.1   Coherence with Previous Work on AA3005

As the direction of the thesis was changed midway through, most of the planned characterization for this material have not been conducted. However, a characterization of a material with a similar composition was performed in the specialization project conducted by the author prior to this thesis and will therefore be applied to determine the state of material and amount of stored energy (driving pressure for further softening). The material had the same production history as the present material, with the same rolling reduction of 92%, thickness of 0.3 mm and annealing temper of H27. By comparing the results from the tensile tests for the as received material in Table 3.3 and the blank material in Table 5.1, it is seen that these materials have the same strength level and the stress-strain curves in Figure 3.35 and Figure 5.4 behave in a similar manner. The curves have a longer region of uniform deformation and the material goes to fracture shortly after necking. In addition, the as received material and the blank material have a similar amount of Mn in solid solution, estimated by electrical conductivity measurements. Due to these similarities, it is reasonable to assume that the present blank material has characteristics which resembles those for the as received material from the specialization project. The microstructural and textural investigations conducted on the as received material in Section 3.4 are therefore used to discuss the microstructural state of the material prior to lacquering. Furthermore, the flash annealing experiments in the specialization project simulates the heat exposure experienced during the drying of the lacquer. The results from this heat experiment will be used to discuss the influence from the heat exposure. The minor temperature and duration differences between the simulated flash annealing experiments and the lacquering process is negligible. The analysis of the dispersoids from BSE imaging is less applicable due to inconsistency with the electrical conductivity measurements and large variation in measurements for the flash annealed sample. However, the BSE imaging do confirm the presence of dispersoids in the material.

6.2 State of Material after Annealing and Driving Pressure for Further Softening

As described in Section 4.1, the treatment of the material prior to lacquering involves pre-heating followed by hot and cold rolling and annealing. The treatment conducted before lacquering suggests that the supersaturation of the solid solution has been decomposed and Mn-bearing dispersoids have formed in the material. These dispersoids remain present in the material with further thermomechanical processing. This is supported by the electrical conductivity measurements, where the amount of Mn in solid solution is low, at 0.317 wt%, and by the BSE imaging in Figure 3.38a and 3.38b conducted during the specialisation project.

Furthermore, the rolling reduction of 92% or strain of 2.5 suggests that the material had a relatively high amount stored dislocations resulting in high stored energy prior to annealing. The high stored energy indicates a large driving pressure for softening. However, the short annealing duration of 3 hours at a temperature below 225°C to H27 suggests that the material is still hard. As stated in Section 4.1, H27 indicate an effective degree of strain hardening above 75% after annealing. The result from the OIM-map in Figure 3.36 further suggests that the softening is the result of static recovery rather than recrystallization. The material has a well defined subgrain structure and no larger equiaxed recrystallized grains. The texture measurements from Figure 3.40 confirms this assumption as Copper, Brass and S-texture are the dominating texture components, which are all typical deformation components. It is therefore reasonable to assume that the largest contribution to softening for this material during annealing is static recovery and the material will therefore have a high driving pressure towards further softening after annealing.

For the mechanical behaviour of the material, the results suggest that the material is more strain hardenable in the rolling direction compared to the transverse direction. In the rolling direction, the material has a longer region of uniform deformation before necking occurs, with a uniform elongation ranging from 0.02 to 0.03 [mm/mm]. In the transverse direction, necking occurs shortly after yielding, at a strain around 0.01 [mm/mm]. As the mechanical properties in Appendix A indicate that the increase in strength is less than 10-15 MPa, the variation and range between the measurements within a testing direction must be minor to be able to quantify the increase in strength. However, the variations in the present results make it difficult to determine the exact strength level after annealing. In the rolling direction the material contains a yield strength at approximately 200 MPa and a ultimate tensile strength at approximately 210 MPa, both with a range in values with 8 MPa. The values from the testing in the transverse direction contained a larger variation in results, as the range was at 20 MPa both for the yield and ultimate tensile strength. An additional uncertainty must be taken into account from the error of measurements, where an error of 0.01 mm can lead to a reduction or increase in strength

with 7 MPa. As the uncertainty does not significantly shift the curve towards longer or shorter strains, i.e. the E modulus is not notably altered, the uncertainty does not affect the measured values for uniform elongation.

The calculated r-values are consistent with r-values for rolled aluminium sheets [75, 76], with a low r-value below 1 in the rolling direction and a higher r-value in the transverse direction, above 1. While there is a significant difference between the values based on the method of calculation both have the same trend with either being lower or higher than 1. The difference in values for the r_2 values can be attributed to error of measurements from the digital caliper.

6.3   Evolution in Mechanical Properties after Lacquering

The variation in measurements combined with the magnitude of the expected increase in strength from Appendix A makes it difficult to determine if the material has become stronger after lacquering. The expected increase in strength for the sample denoted 1, is 10 and 15 MPa for the yield and ultimate tensile strength, respectively. However, these results were not reproduced by the tensile testing conducted in the present thesis. In the rolling direction, the lacquered material had the same strength level and range in measured values as the blank material and it is therefore not possible to determine any increase in strength. In the transverse direction, the measurements are consistent for all three lacquered specimens. However, due to the 20 MPa measured variation in strength for the blank specimens, it is not possible to quantify an increase in strength. The same uncertainty as for the blank specimens must be considered as well.

However, from the stress-strain curves, a clear change in behaviour is seen after lacquering. The lacquered material has a more rapid reduction in strength after necking and goes to fracture at a lower strain range than the blank material. The more rapid reduction in strength can not be attributed to the location where necking occurs in the specimen, as necking and fracture has occurred at a similar placement on the tensile specimen within the range of the extensometer, seen from Figure 5.9. It can not be attributed to change in anisotropy either, as it has not been altered by the lacquering process.

The most notable change in mechanical behaviour after lacquering is the reduction in uniform elongation, where it is consistently reduced after lacquering both in the rolling and transverse direction with 0.001-0.002 [mm/mm].

6.4   The Influence of the Heat Exposure from the Lacquering Process

The heat exposure from the drying of the lacquer consist of a two step heating sequence. The first oven has a temperature of 232°C while the second oven has a temperature of 253°C. The

material is exposed to the elevated temperature for 19 seconds in both ovens and the material is quenched down to room temperature after each of the heat exposures. As the temperatures in the lacquering process is higher than the annealing temperature for the material (224°C), it is possible that the material can be influence by the additional exposure. This is confirmed by the evolution in mechanical behaviour observed for the flash annealed material. The change in mechanical properties is consistent with the trends seen for the tensile tests conducted on the lacquered material in the rolling direction and the material tested in Appendix A. A consistent reduction in uniform elongation was measured after flash annealing combined with a possible increase in yield strength.

6.4.1   Softening and Concurrent Precipitation

As the investigated 3xxx aluminium alloy is non-heat treatable, exposure to elevated temperatures typically leads to softening. While the material still has a high amount of stored dislocations prior to lacquering, the short duration and the low temperature in the ovens suggests that the amount of softening that can occur during the lacquering process is limited. From the investigations on softening behaviour conducted by Sjølstad [9] and Tangen et al. [65], an annealing temperature below 300°C results in a slow softening for an extended amount of time, independent of strain level. Furthermore, the Zener drag which retards softening must be considered as well. Based on the findings from Huang et al. [96] and Tangen [10], pre-existing dispersoids can contribute to strong Zener drag, independent on whether the distribution of dispersoids are homogeneous or if the dispersoids are mainly located on the subgrains and grain boundaries. While it is not possible to determine the magnitude of the Zener drag from the the dispersoids in the present material, it is reasonable to assume that they do contribute to a slower softening in some extent. A possible Zener drag from concurrent precipitation is, however, negligible as the material have a low amount of Mn in solid solution prior to lacquering. From the TTT-diagrams in Figure 3.4, it is evident that the combination of a low annealing temperature and a short annealing time reduces the possibility for concurrent precipitation to occur. Furthermore, from the flash annealing experiments, no increase in conductivity were measured either and it is therefore reasonable to conclude that concurrent precipitation has not occurred.

Based on a possible Zener drag from dispersoids combined with the low temperatures in the ovens and the short duration of the heat exposure, the amount of softening that could possibly occur is negligible. This is confirmed by the tensile testing on the lacquered and flash annealed material. No increase in elongation or reduced strength level was detected from the tensile testing. Furthermore, no recrystallization or recovery were seen from the OIM-maps or XRD measurement. The differences in fraction recrystallized, subgrain size and recrystallization

texture components can be attributed to local variations within the sheet, as two different samples were utilized both for EBSD and XRD. One can therefore concluded that recrystallization has not occur during the lacquering process. While recovery activities might occur, the contribution to softening is negligible.

6.4.2 Strengthening Contribution from Evolution in Mn-bearing Dispersoids

Small dispersoids do contribute to strength through the Orowan bowing mechanism of non shearable particles and has been correctly estimated by the Orowan-Ashby equation as shown by both Li et al. [97] and Zhao et al. [15]. However, if an increase in strengthening is caused by dispersoids, then this must be the result of a higher density of small dispersoids after lacquering. It follows from the discussion in the previous section, that concurrent precipitation is unlikely due to the short duration of exposure combined with the low temperature and low supersaturation of Mn in solid solution. Furthermore, the strengthening is unlikely caused by any growth or dissolution of pre-existing dispersoids, as these are found to be thermally stable at temperatures below 375°C by Li et al. [97] and the total duration of the heating is less than 1 minute. Pre-existing dispersoids are observed throughout longer annealing experiments as seen by Tangen [10] and Huang et al. [96].

6.4.3 Precipitation of Metastable Mg$_2$Si Precipitates

While precipitation of metastable Mg$_2$Si dispersoids have been observed to occur in 3xxx aluminium alloys, these have only been observed during homogenization or pre-heating of 3xxx aluminium alloys in as-cast variants. In the as cast state, the amount of Si in solid solution is high and during continuous heating or heating at low temperatures, these metastable precipitates form due to decomposition of the supersaturated alloy. However, as found by Li et al. [104] these precipitates will dissolve at temperatures above 350°C leaving Si rich zones for Mn-bearing dispersoids to form on. As the Mn-bearing dispersoids in 3xxx aluminium alloys contain various amount of Si, the level of Si in solid solution will be significantly lower after the formation of dispersoids during pre-heating than in the as cast state. For the investigated 3005 alloy, a pre-heating has been conducted where the material was heated to temperatures above 500°C, which suggests that if any metastable Mg$_2$Si precipitates have precipitated, then they have been dissolved and Mn bearing dispersoids will have precipitate upon these Si-rich zones. With further heating at lower temperatures (during the annealing and in the lacquering process), the potential for forming additional metastable Mg$_2$Si precipitates will therefore be significantly reduced. It is therefore unlikely that precipitation of metastable Mg$_2$Si precipitates have occurred during the lacquering process and have contributed to strength.

6.4.4   Hardening on Annealing

There are several similarities between investigations were hardening on annealing has been observed and the heating that occurs during the lacquering process. The temperatures used during lacquering for the investigated material is between 232-253°C which are within the temperature range of where HOA has been observed in non-heat treatable alloys, which is typically below 300°C. In addition, this is a phenomenon that can be observed within seconds or minutes which are consistent with the duration of the heat exposure during lacquering. From the mechanical testing conducted by Sæter [24], a rapid reduction in fracture elongation were observed after 10 seconds together with an increase in strength. The same trend was found by Govindaraj et al. [106] with both the uniform and fracture elongation. While the increase in strength in the present investigation has been difficult to quantify due the variation in measurements, the reduction in uniform elongation are consistent with previous investigation. Furthermore, the trend in evolution in mechanical behaviour observed in previous investigations corresponds with the changes reported by Hydro Aluminium Rolled Products Holmestrand in Appendix A.

As none of the reviewed literature has been able to conclude on the mechanism causing hardening on annealing, no clear explanation exists. Different explanations have been suggested depending on the result from the investigations. However, the strain dependency has been observed in all of the relevant reviewed literature, where the magnitude of HOA increases with strain. As the deformation strain increases, the material has a high amount of deformation heterogeneities and a larger amount of stored dislocation, leading to the formation of a well developed subgrain structure. During low temperature annealing, the material will soften most likely through recovery and the extent of HOA will therefore be in balance with the magnitude of the softening from recovery activities.

The influence on alloying elements is unclear, where especially the contribution from Mn and Si is debated. However, it is indisputable that alloying elements are crucial for the occurrence of HOA as it is not observed in high purity alloys. Both clustering between Mn and other alloying elements and precipitation of Si have been suggested as possible causes for HOA as they can be introduced at elevated temperatures and they hinder dislocation movement. However, neither have been detectable by electrical conductivity measurements as Si has a minor influence on the conductivity according to Altenpohl (cf. Equation 4.2) while the contribution of small clusters are not distinguishable from the contribution of solutes. Nor have they been detected by TEM, which indicate that they must be very small. In the present material, the level of Mn in solid solution is low compared to many of the investigated alloys in the reviewed literature. From the annealing experiments conducted by Tangen [10], the possibility for HOA is significantly reduced as the level of Mn in solid solution is lowered. While the same solute dependency was not seen by

Govindaraj et al. [106], this could be attributed to the use of significant larger deformation strain levels than by other investigations. It is therefore reasonable to assume that the magnitude of HOA is somewhat dependent on the saturation in the material. Combining the low amount of Mn with the low amount of Si in solid solution, this could suggest that the possibility for HOA in the present material is low. However, the material contains a larger amount of Mg and Cu than the alloys investigated in the reviewed literature, which could possibly contribute. From the proposed models by Starink et al. [120] and Zhao [122] dimers or clusters containing less than 20 atoms can contribute to strength, either by an elastic misfit or by order strengthening depending on their interaction energy and misfit to the matrix. The experimental investigation conducted by Zhao et al. [123] further confirms that both mechanisms may contribute to strength in 3xxx alloys. While the contribution from an elastic misfit were found to play a major role in the strengthening due to the large misfit between the matrix and Mn and Si, the authors did detect a small influence from order strengthening as well. With higher additions of Cu and Mg, at 0.17 wt% and 0.31 wt%, respectively, the contributions from either models could possibly be higher in the investigated material depending on interaction energy between atoms and misfit with the matrix.

As the hardening effect is seen in aluminium alloys that are not severely plastic deformed, dislocation source limitation is not a likely mechanism for the hardening phenomenon. The results reported by Govindaraj et al. [106] confirms this assumption as the introduction of additional strain did not remove the hardening effect which should occur with dislocation source limitation.

As the investigated material is already recovered prior to lacquering, the mechanism leading to HOA has most likely already been introduced during annealing. As the material has become softer, the magnitude of the initial hardening effect from HOA has been overshadowed by the softening from recovery. With the heat exposure from the lacquering process, an additional amount or a reintroduction of possible Si-precipitates or clusters must be introduced to create an additional HOA effect. It is therefore difficult to determine on the plausibility for this to occur as the mechanism behind HOA is unknown. The complexity of the lacquering process and the prior treatment compared to the reviewed literature makes it further difficult to conclude. It is possible that the rapid heating and cooling from the lacquering process could give an enhanced effect. Clustering or precipitation of very small precipitates can therefore not be excluded as a possible reason for the evolution in mechanical behaviour observed with lacquering.

6.5 Hardening from Strain Path Changes

A possible increase in yield strength can be consistent with cross hardening, which is observed after orthogonal strain path changes in aluminium alloys. The transient behaviour on the

yielding of the material and on the work hardening rate has by many investigations been attributed to changes in the dislocation structure, where the structure that develops during prestraining becomes unstable upon a strain path change. As observed by Lloyd and Sang [88], the cell structure that develops in 1xxx and 3xxx alloys have a low resistance towards SPCs due to a inhomogeneous distribution of the dislocation structure. Furthermore, as the cell structure became more developed, larger persistent changes on the stress-strain curve were observed as the strength exceed the monotonic level. In addition, a larger prestrain also reduced the uniform elongation which is consistent with later investigations. As seen from the reviewed literature aluminium alloys do have a high susceptible toward early necking from a prestrain. As the investigated material does not show any permanent softening after lacquering, the magnitude of a possible stress overshoot must exceed the influence of a possible reduction in work hardening rate. This corresponds with the trend from the mechanical properties in Appendix A found for several AA3005 alloys, where neither samples have a reduction in ultimate tensile strength after lacquering. Further, as the increase in yield is not proportional to the increase in ultimate tensile strength, a possible SPC must have resulted in a transient effect on the work hardening curve which is not consistent between the samples (coils). The magnitude and duration of the transient effect on the work hardening rate can be associated the establishing of the final structure as found by Barlat et al. [79]. If the two straining directions have many of the same active slip system, the range of the transient behaviour will be smaller as the final structure establishes through rearrangement rather than superimposition and dissolution. As the increase in ultimate tensile strength is never higher than the increase in yield strength, a significant increase in work hardening rate from superimposition is unlikely.

The effect from the anisotropic behaviour must be considered as well. As observed by both Zandrahimi et al. [81] and Li and Bate [78], anisotropy can amplify the effect from the SPC on the work hardening rate and on the stress overshoot. This was especially observed by Li and Bate when the prestraining was conducted in a direction with higher strength. Independent of the angle between the straining directions, the stress overshoot was higher compared to prestraining conducted at an angle with a lower strength.

On the influence of dispersoids, the findings from Zhao et al. [102] suggests that dispersoids can give a strong Bauschinger effect as they can cause a reversibility of dislocation loops. The reversibility may occur for orthogonal SPCs as well, as slip systems can be reversed with a Schmitt angle less than -1 [124]. This would suggest that any effect from the dispersoids on a SPC would lead to a weakening of the stress overshoot. The effect from dispersoids on further work hardening is minor as the influence from the dispersoids is diminished with increasing strain. However, based on the work of Qin et al. [124], a strong stress overshoot is still plausible for a dispersoid containing 3xxx alloy. This suggests that the investigated material can experience a

cross hardening by an orthogonal SPC.

In the present investigation, the material already have a well-developed dislocation structure prior to lacquering as seen from the OIM-map in Figure 3.36. For this structure to become unstable, the SPC must occur at an angle from the rolling direction. Furthermore, from the tensile tests conducted on the material, it is seen that lacquering has affected the material in both the rolling and transverse direction in the same manner, in terms of uniform elongation and strength. It is therefore reasonable to assume that the the direction of the SPC must result in a new unstable dislocation structure to both the rolling and the transverse direction.

While the anisotropy can influence the effects of a SPC, it is difficult to determine the magnitude, as no testing was conducted on the strength in the material at an angle less than 90° to the rolling direction. However, the present material has a lower strength level in the rolling direction compared to the transverse direction suggesting that a prestraining could have an extended effect. Due to the complexity of the mechanical properties combined with the lack of testing, it is difficult to determine how an orthogonal SPC would affect the evolution in mechanical behaviour. It should be noted that during the lacquering process, the material is moved forward by the ends of the coil (in the rolling direction) and it is therefore no obvious stage in the process where such an abrupt SPC could take place. Furthermore, all samples were collected in the same manner and in the same region of the coil and has therefore not influenced the evolution in mechanical properties. While a cross hardening effect could possible occur from a SPC, it is unlikely the reason for the observed evolution in mechanical behaviour, as there is nothing indicated from the lacquering process that such a change in straining direction can occur.

7   Conclusion

In this work, mechanical testing of AA3005 sheets were performed to determine the evolution in mechanical properties after lacquering. A literature review was conducted to give an overview on previous investigations and proposed mechanisms relevant for the observed changes in mechanical behaviour during lacquering. The aim was to investigate the influence of the exposure to elevated temperatures during the drying of the lacquer and possible strain path changes. In addition, results obtained from the specialization project was utilized as well.

The obtained results can be summarized as follows:

- Mechanical testing have detected an evolution in mechanical behaviour after lacquering for the investigated AA3005 alloy, however the extent of the change in strength is difficult to quantify due to the variation between the tensile specimens. The most persistent change is the reduction in uniform elongation after lacquering detected both in the rolling and transverse direction. No change in anisotropy was detected after lacquering.

- It is reasonable to assume that the heat exposure have influenced the mechanical behaviour based on the similarities between the change in mechanical properties for the flash annealed material tested in the specialisation project and the lacquered material tested.

- As no reduction in strength or longer uniform elongation was detected by the tensile testing, no recrystallization has occurred. This is confirmed by the obtained results from the microstructure and texture investigations from the specialization project. Any softening contributions from recovery activities are negligible.

- It is unlikely that the evolution in mechanical behaviour is caused by concurrent precipitation as the amount of Mn in solid solution is low combined with the low temperature in the ovens during lacquering and the short duration of the heat exposure. Prior flash annealing experiments on a similar AA3005 alloy confirms that concurrent precipitation has not occurred, as no change in conductivity was detected.

- The pre-existing dispersoids in 3xxx alloys are thermally stable at temperatures below 375°C and it is therefore reasonable to assume that growth or dissolution of pre-existing dispersoids have not occurred after short heat exposures at low temperatures.

- The possibility for precipitation of metastable Mg_2Si is unlikely, as the amount of Si in solid solution is low prior to lacquering.

- Clusters of Mn and other alloying elements or precipitation of very small Si precipitates could be a possible cause for the evolution in mechanical behaviour. The observed changes are consistent with a phenomenon known as hardening on annealing, seen during early stages of low temperature annealing in 3xxx alloys. While both clusters and Si precipitates have been suggested as possible mechanisms, previous investigations have not been able to conclude on the mechanism leading to the hardening effect. It is therefore difficult to

determine if clustering or precipitation of Si has occurred during lacquering process.

- A possibility for hardening after a strain path change has been established by considering anisotropy and the formation of unstable dislocation structure upon an SPC. Hardening may possible be achieved by straining the alloy at an angle between the rolling and transverse direction. As there is nothing indicated from the lacquering process that such a change in straining direction can occur, strain path change is as an unlikely cause for the observed changes in mechanical behaviour.

8   Further Work

- In the present work, the influence of the lacquer itself has not been investigated. It could therefore by useful to conduct mechanical testing on the lacquered material after removing the lacquer.

- It would be interesting to characterize the hardening effect in terms how it is affected by longer heat exposures and different temperatures.

- It could be useful to investigate the influence of Mg, Cu and other alloying elements on the hardening effect by comparing the observed changes in mechanical behaviour in the investigated material with 3xxx alloys without these alloying elements.

- Atom probe measurements and atomistic simulations could provide additional insight on the influence from clusters.

- Microstructural investigations in TEM can provide information on possible changes dislocation structure in the alloy before and after the lacquering process.

9 References

1. Polmear IJ. Light alloys: from traditional alloys to nanocrystals. 4th ed. Oxford ; Burlington, MA: Elsevier/Butterworth-Heinemann, 2006.

2. Underhaug KM. Mechanical properties and microstructural evolution in cold rolled AA3xxx. Unpublished specialization project. 2019.

3. Lyle JP, Granger DA and Sanders RE. Aluminum Alloys. In: *Ullmann's Encyclopedia of Industrial Chemistry.* Ed. by Wiley-VCH Verlag GmbH & Co. KGaA. Weinheim, Germany: Wiley-VCH Verlag GmbH & Co. KGaA, 2000.

4. Solberg J. Teknologiske metaller og legeringer. Trondheim: Norges teknisk-naturvitenskapelige universitet, 2014.

5. Kammer C, ed. Aluminium Handbook. 1st ed. Dusseldörf: Aluminium-Verlag, 1999.

6. Zolotorevskiĭ VS, Belov NA and Glazoff MV. Casting aluminum alloys. 1st ed. Oxford: Elsevier Science, 2007.

7. Humphreys FJ, Rohrer GS and Rollett AD. Recrystallization and related annealing phenomena. Third edition. Amsterdam Oxford Cambridge, MA: Elsevier, 2017.

8. Wang N. Softening behaviour of Al-Mn-Fe-Si alloys during isothermal annealing. PhD thesis. Trondheim: Norges teknisk- naturvitenskapelige universitet, Institutt for materialteknologi, 2013.

9. Sjølstad K. Deformation and softening behaviour of commercial AlMn-alloys: experiments and modelling. PhD thesis. Trondheim: Norges teknisk- naturvitenskapelige universitet, Institutt for materialteknologi, 2003.

10. Tangen S. Deformation and annealing behavior of commerical non-heat treatable aluminium alloys: An experimental investigation. PhD thesis. Trondheim: Norges teknisk- naturvitenskapelige universitet, Institutt for materialteknologi, 2004.

11. De Haan P, Van Rijkom J and Söntgerath J. *The Precipitation Behaviour of High-Purity Al-Mn Alloys.* Materials Science Forum 1996;217-222:765–70.

12. Hausch G, Furrer P and Warlimont H. Z. Metallkunde 1978;69:174–80.

13. Li YJ and Arnberg L. *Quantitative study on the precipitation behavior of dispersoids in DC-cast AA3003 alloy during heating and homogenization.* Acta Materialia 2003;51:3415–28.

14. Alexander DTL and Greer † AL. *Nucleation of the Al $_6$ (Fe, Mn)-to-α-Al–(Fe, Mn)–Si transformation in 3XXX aluminium alloys. I. Roll-bonded diffusion couples.* Philosophical Magazine 2004;84:3051–70.

15. Zhao Q. The influence of Mn, Fe and Si on the work hardening of aluminium alloys. PhD thesis. Trondheim: NTNU, 2013.

16. Muggerud AMF, Li YJ and Holmestad R. Orientation Studies of &α&-Al(Fe,Mn)Si Dispersoids in 3xxx Al Alloys. In: *Materials Science Forum.* Vol. 794-796. Trans Tech Publications, 2014:39–44.

17. Furrer P and Hausch G. *Recrystallization behaviour of commerical Al-1%Mn alloy.* Metal Science 1979;13:155–62.

18. Li YJ and Arnberg L. *Evolution of eutectic intermetallic particles in DC-cast AA3003 alloy during heating and homogenization.* Materials Science & Engineering A 2003;347:130–5.

19. Dowling NE, Siva Prasad K and Narayanasamy R. Mechanical behavior of materials: engineering methods for deformation, fracture, and fatigue. 4. ed., internat. ed. Boston, Mass.: Pearson, 2013.

20. Ryen Ø. Work hardening and mechanical anisotropy of aluminium sheets and profiles. PhD thesis. Trondheim: Norges teknisk-naturvitenskapelige universitet, Institutt for materialteknologi, 2003.

21. Furu T, Ørsund R and Nes E. *Subgrain growth in heavily deformed aluminium—experimental investigation and modelling treatment.* Acta Metallurgica et Materialia 1995;43:2209–32.

22. Gil Sevillano J, Houtte P van and Aernoudt E. *Large strain work hardening and textures.* Progress in Materials Science 1980;25:69–134.

23. Gil Sevillano J, Houtte P van and Aernoudt E. *The deformed state of metals (II): Structure.* Progress in Materials Science 1980;25:135–271.

24. Sæter JA. Substructure evolution and strengthening in cold rolled and annealed aluminium alloys: Experiments and modelling. PhD thesis. Trondheim: Norges teknisk-naturvitenskapelige universitet, Institutt for materialteknologi, 1997.

25. Nord-Varhaug K, Forbord B, Benestad J et al. *Substructure Strengthening in Aluminium Alloys.* Materials Science Forum 2000;331-337:1387–92.

26. Vatne H, Furu T, Ørsund R and Nes E. *Modelling recrystallization after hot deformation of aluminium.* Acta Materialia 1996;44:4463–73.

27. Hughes D and Hansen N. *High angle boundaries formed by grain subdivision mechanisms.* Acta Materialia 1997;45:3871–86.

28. Bunkholt S. Subgrain Growth, Recovery Kinetics and Nucleation of Recrystallization of Cold Deformed Aluminium Alloys. PhD thesis. Trondheim: NTNU, 2013.

29.   Doherty R, Hughes D, Humphreys F et al. *Current issues in recrystallization: a review.* Materials Science and Engineering: A 1997;238:219–74.

30.   Verlinden B, Driver J, Samajdar I and Doherty RD. Thermo-Mechanical Processing of Metallic Materials. Kidlington: Elsevier Science, 2014.

31.   Humphreys FJ and Hatherly M. Recrystallization and related annealing phenomena. 2nd ed. Amsterdam ; Boston: Elsevier, 2004.

32.   Leffers T. Proc 2th Int. Risø Symposium on Metallurgy and Materials (ed. Hansen et al.) 1981.

33.   Raabe D. Recovery and Recrystallization: Phenomena, Physics, Models, Simulation. In: *Physical Metallurgy.* Elsevier, 2014:2291–397.

34.   Porter DA, Easterling KE and Sherif MY. Phase transformations in metals and alloys. 3rd ed. Boca Raton, FL: CRC Press, 2009.

35.   Gottstein G and Shvindlerman LS. Grain boundary migration in metals: thermodynamics, kinetics, applications. 2nd ed. CRC series in materials science and technology. Boca Raton: Taylor & Francis, 2010.

36.   Hu H. *Direct observation on the annealing of Si-Fe crystals in the electron microscope.* Trans. Metall. Soc. AIME 224 1962;1:75–84.

37.   Avrami M. *Kinetics of Phase Change. I General Theory.* The Journal of Chemical Physics 1939;7:1103–12.

38.   Johnson W and Mehl R. *Reaction Kinetics in Processes of Nucleation and Growth.* AIME 1939;135:416–42.

39.   Kolmogorov AN. *On the Statistical Theory of Crystallization of Metals.* Izv. Akad. Nauk., USSR Ser. Matemat. 1937;1:355–9.

40.   Huang Y and Humphreys F. *Measurements of grain boundary mobility during recrystallization of a single-phase aluminium alloy.* Acta Materialia 1999;47:2259–68.

41.   Huang Y and Humphreys F. *Subgrain growth and low angle boundary mobility in aluminium crystals of orientation {110}001.* Acta Materialia 2000;48:2017–30.

42.   Gottstein G. Physical foundations of materials science. Berlin: Springer, 2010.

43.   Nes E and Hutchinson W. *Proc. 10th Int. Risø Symp. on Metallurgy and Materials (eds. Sørensen et al.)* Risø National Laboratory, Roskilde 1989:233.

44.   Hjelen J, Ørsund R and Nes E. *On the origin of recrystallization textures in aluminium.* Acta Metallurgica et Materialia 1991;39:1377–404.

45.   Duggan BJ, Hatherly M, Hutchinson WB and Wakefield PT. *Deformation structures and textures in cold-rolled 70:30 brass.* Metal Science 1978;12:343–51.

46. Dillamore IL, Morris PL, Smith CJE and Hutchinson WB. *Transition Bands and Recrystallization in Metals*. Proceedings of the Royal Society of London. Series A, Mathematical and Physical Sciences 1972;329:405–20.

47. Somerday M and Humphreys FJ. *Recrystallisation behaviour of supersaturated Al–Mn alloys Part 1 – Al–1.3 wt-%Mn*. Materials Science and Technology 2003;19:20–9.

48. Bellier S and Doherty R. *The structure of deformed aluminium and its recrystallization—investigations with transmission Kossel diffraction*. Acta Metallurgica 1977;25:521–38.

49. Hutchinson WB, Oscarsson A and Karlsson Å. *Control of microstructure and earing behaviour in aluminium alloy AA 3004 hot bands*. Materials Science and Technology 1989;5:1118–27.

50. Humphreys F. *The nucleation of recrystallization at second phase particles in deformed aluminium*. Acta Metallurgica 1977;25:1323–44.

51. Cao G. Nanostructures and nanomaterials: synthesis, properties, and applications. 2nd ed. Vol. 2. World Scientific series in nanoscience and nanotechnology. New Jersey: World Scientific, 2011.

52. Humphreys FJ and Hatherly M. Recrystallization and related annealing phenomena. 1st ed. Oxford, OX, UK ; Tarrytown, N.Y., U.S.A: Pergamon, 1995.

53. Nes E, Ryum N and Hunderi O. *On the Zener drag*. Acta Metallurgica 1985;33:11–22.

54. Huang K, Marthinsen K, Zhao Q and Logé RE. *The double-edge effect of second-phase particles on the recrystallization behaviour and associated mechanical properties of metallic materials*. Progress in Materials Science 2018;92:284–359.

55. Hornbogen E and Köstner U. Recrystallization of Metallic Materials, (ed. Haeßner F.) Stuttgart: Dr. Riedrer-Verlag, 1978.

56. Randle V and Engler O. Introduction to texture analysis: macrotexture, microtexture and orientation mapping. Amsterdam, The Netherlands: Gordon & Breach, 2000.

57. Dieter GE and Bacon D. Mechanical metallurgy. SI metric ed. McGraw-Hill series in materials science and engineering. London: McGraw-Hill, 1988.

58. Bunge HJ. Texture analysis in materials science: mathematical methods. English ed. London ; Boston: Butterworths, 1982.

59. Hirsch JR. *Correlation of deformation texture and microstructure*. Materials Science and Technology 1990;6:1048–57.

60. Dillamore IL and Katoh H. *The Mechanisms of Recrystallization in Cubic Metals with Particular Reference to Their Orientation-Dependence*. Metal Science 1974;8:73–83.

61. Daaland O, Dronen PE, Vatne HE, Naess S and Nes E. *On the Growth Rate of Cube-, Rotated Cube- and Rotated Goss-Grains in Commercial Aluminium Alloys.* Materials Science Forum 1993;113-115:115–20.

62. Vatne H and Nes E. *The origin of recrystallisation texture and the concept of micro-growth selection.* 1994;30:309–12.

63. Samajdar I and Doherty RD. *Role of S[(123)634] orientations in the preferred nucleation of cube grains in recrystallization of FCC metals.* Scripta Metallurgica et Materialia 1995;32:845–50.

64. Vatne H, Furu T and Nes E. *Nucleation of recrystallised grains from cube bands in hot deformed commercial purity aluminium.* Materials Science and Technology 1996;12:201–10.

65. Tangen S, Sjølstad K, Furu T and Nes E. *Effect of Concurrent Precipitation on Recrystallization and Evolution of the P-Texture Component in a Commercial Al-Mn Alloy.* Metallurgical and Materials Transactions A 2010;41:2970–83.

66. Vatne HE, Engler O and Nes E. *Influence of particles on recrystallisation textures and microstructures of aluminium alloy 3103.* Materials Science and Technology 1997;13:93–102.

67. Nes E. *Modelling of work hardening and stress saturation in FCC metals.* Progress in Materials Science 1997;41:129–93.

68. Kocks U and Mecking H. *Physics and phenomenology of strain hardening: the FCC case.* Progress in Materials Science 2003;48:171–273.

69. Haasen P. Mechanical properties of solid solutions in: in: *R.W. Cahn, P. Haasen (Eds.) Physical Metallurgy.* 4th. North-Holland: Elsevier Science, 1996:2009–73.

70. Butt MZ and Feltham P. *Solid-solution hardening.* Journal of Materials Science 1993;28:2557–76.

71. Muggerud AMF, Mørtsell EA, Li Y and Holmestad R. *Dispersoid strengthening in AA3xxx alloys with varying Mn and Si content during annealing at low temperatures.* Materials Science and Engineering: A 2013;567:21–8.

72. Callister WD and Rethwisch DG. Materials science and engineering. 9. ed., SI version. Hoboken, NJ: Wiley, 2015.

73. Lankford W, Snyder S and Bauscher J. *New criteria for predicting the press performance of deep drawing sheets.* Trans. ASM 1950;42:1197–205.

74. Wenk H. Preferred Orientation in Deformed Metal and Rocks. Orlando: Academic Press, 1985.

75.   Zhang K, Holmedal B, Hopperstad OS and Dumoulin S. *Modelling the plastic anisotropy of aluminum alloy 3103 sheets by polycrystal plasticity.* Modelling and Simulation in Materials Science and Engineering 2014;22:075015.

76.   Engler O. *Texture and anisotropy in cold rolled and recovery annealed AA 5182 sheets.* Materials Science and Technology 2015;31:1058–65.

77.   Hosford WF and Caddell RM. Metal Forming: mechanics and metallurgy. 4th edition. Cambridge ; New York: Cambridge University Press, 2011.

78.   Li F and Bate P. *Strain path change effects in cube textured aluminium sheet.* Acta Metallurgica et Materialia 1991;39:2639–50.

79.   Barlat F, Ferreira Duarte J, Gracio J, Lopes A and Rauch E. *Plastic flow for non-monotonic loading conditions of an aluminum alloy sheet sample.* International Journal of Plasticity 2003;19:1215–44.

80.   Hutchinson W, Arthey R and Malmström P. *On anomalously low work-hardening in pre-strained metals.* Scripta Metallurgica 1976;10:673–5.

81.   Zandrahimi M, Platias S, Frice D, Barrett D, Bate PS and Roberts WT. *Effects of changes in strain path on work hardening in cubic metals.* Metallurgical Transactions A 1989;20:2471–82.

82.   Schmitt J, Aernoudt E and Baudelet B. *Yield loci for polycrystalline metals without texture.* Materials Science and Engineering 1985;75:13–20.

83.   Holmedal B, Houtte PV and An Y. *A crystal plasticity model for strain-path changes in metals.* International Journal of Plasticity 2008;24:1360–79.

84.   Juul Jensen D and Hansen N. *Flow stress anisotropy in aluminium.* Acta Metallurgica et Materialia 1990;38:1369–80.

85.   Li Z, Winther G and Hansen N. *Anisotropy of plastic deformation in rolled aluminum.* Materials Science and Engineering: A 2004;387-389:199–202.

86.   Wilson D and Bate P. *Influences of cell walls and grain boundaries on transient responses of an if steel to changes in strain path.* Acta Metallurgica et Materialia 1994;42:1099–111.

87.   Gracio J, Lopes A and Rauch E. *Analysis of plastic instability in commercially pure Al alloys.* Journal of Materials Processing Technology 2000;103:160–4.

88.   Lloyd DJ and Sang H. *The influence of strain path on subsequent mechanical properties—Orthogonal tensile paths.* Metallurgical Transactions A 1979;10:1767–72.

89.   Wagoner RH and Laukonis JV. *Plastic behavior of aluminum-killed steel following plane-strain deformation.* Metallurgical Transactions A 1983;14:1487–95.

90.   Rauch E and Schmitt JH. *Dislocation substructures in mild steel deformed in simple shear.* Materials Science and Engineering: A 1989;113:441–8.

91. Rauch E and Thuillier S. *Rheological behaviour of mild steel under monotonic loading conditions and cross-loading.* Materials Science and Engineering: A 1993;164:255–9.

92. Lewandowska M. *Dependence of the deformation microstructure of aluminium alloys on the strain path.* Materials Chemistry and Physics 2003;81:555–7.

93. Gaspérini M, Pinna C and Swiatnicki W. *Microstructure evolution and strain localization during shear deformation of an aluminium alloy.* Acta Materialia 1996;44:4195–208.

94. Orowan E. Causes and Effects of Internal Stresses. In: *Internal Stresses and Fatigue in Metals.* New York: Elsevier Publishing Company, 1959.

95. Vincze G, Rauch E, Gracio J, Barlat F and Lopes A. *A comparison of the mechanical behaviour of an AA1050 and a low carbon steel deformed upon strain reversal.* Acta Materialia 2005;53:1005–13.

96. Huang K, Li Y and Marthinsen K. *Effect of heterogeneously distributed pre-existing dispersoids on the recrystallization behavior of a cold-rolled Al–Mn–Fe–Si alloy.* Materials Characterization 2015;102:92–7.

97. Li YJ, Muggerud AMF, Olsen A and Furu T. *Precipitation of partially coherent α-Al(Mn,Fe)Si dispersoids and their strengthening effect in AA 3003 alloy.* Acta Materialia 2012;60:1004–14.

98. Ashby MF. *Work hardening of dispersion-hardened crystals.* Philosophical Magazine 1966;14:1157–78.

99. Hirsch P and Humphreys FJ. *The deformation of single crystals of copper and copper-zinc alloys containing alumina particles - I. Macroscopic properties and workhardening theory.* Proceedings of the Royal Society of London. A. Mathematical and Physical Sciences 1970;318:45–72.

100. Humphreys FJ and Hirsch P. *The deformation of single crystals of copper and copper-zinc alloys containing alumina particles - II. Microstructure and dislocation-particle interactions.* Proceedings of the Royal Society of London. A. Mathematical and Physical Sciences 1970;318:73–92.

101. Forbord B, Marthinsen K and Nes E. *Modelling the Work Hardening in Cold Rolled and Annealed Aluminium Sheet.* Materials Science Forum 2000;331-337:557–64.

102. Zhao Q, Holmedal B and Li Y. *Influence of dispersoids on microstructure evolution and work hardening of aluminium alloys during tension and cold rolling.* Philosophical Magazine 2013;93:2995–3011.

103. Lodgaard L and Ryum N. *Precipitation of dispersoids containing Mn and/or Cr in Al–Mg–Si alloys.* Materials Science and Engineering: A 2000;283:144–52.

104.   Li Z, Zhang Z and Chen XG. *Effect of Metastable Mg2Si and Dislocations on α-Al(MnFe)Si Dispersoid Formation in Al-Mn-Mg 3xxx Alloys*. Metallurgical and Materials Transactions A 2018;49:5799–814.

105.   Huang X, Hansen N and Tsuji N. *Hardening by Annealing and Softening by Deformation in Nanostructured Metals*. Science 2006;312:249–51.

106.   Govindaraj N, Bjørge R and Holmedal B. *Characterizing Hardening on Annealing of Cold-Rolled Aluminum AA3103 Strips*. Metallurgical and Materials Transactions A 2014;45:1597–608.

107.   Birol Y. *Recrystallization of a supersaturated Al–Mn alloy*. Scripta Materialia 2008;59:611–4.

108.   Wang N, Li Y and Marthinsen K. Article I: The softening behaviour of cold-rolled Al-Mn-Fe-Si-alloys influenced by concurrent precipitation. In: *Softening behaviour of Al-Mn-Fe-Si alloys during isothermal annealing (Doctoral thesis)*. 2013:153–91.

109.   Huang K, Zhao Q, Li Y and Marthinsen K. *Two-stage annealing of a cold-rolled Al–Mn–Fe–Si alloy with different microchemistry states*. Journal of Materials Processing Technology 2015;221:87–99.

110.   Kahl S, Ekström HE and Mendoza J. *Tensile, Fatigue, and Creep Properties of Aluminum Heat Exchanger Tube Alloys for Temperatures from 293 K to 573 K (20 °C to 300 °C)*. Metallurgical and Materials Transactions A 2014;45:663–81.

111.   Ryen Ø, Holmedal B, Nijs O, Nes E, Sjölander E and Ekström HE. *Strengthening mechanisms in solid solution aluminum alloys*. Metallurgical and Materials Transactions A 2006;37:1999–2006.

112.   Lee N, Kao P, Tseng T and Su J. *Effect of manganese addition on the tensile properties of cold-rolled and recovery-annealed aluminum alloy sheets*. Materials Science and Engineering: A 2012;535:297–305.

113.   Ringer S and Hono K. *Microstructural Evolution and Age Hardening in Aluminium Alloys*. Materials Characterization 2000;44:101–31.

114.   Edwards G, Stiller K, Dunlop G and Couper M. *The precipitation sequence in Al–Mg–Si alloys*. Acta Materialia 1998;46:3893–904.

115.   Ringer S, Sakurai T and Polmear I. *Origins of Hardening in Aged Al-Cu-Mg-(Ag) Alloys*. Acta Materialia 1997:3731–44.

116.   Hasting HS, Walmsley J, Marioara CD et al. *Characterisation of early precipitation stages in 6xxx series aluminium alloys*. Journal of Physics: Conference Series 2006;26:99–102.

117. Marceau R, Sha G, Ferragut R, Dupasquier A and Ringer S. *Solute clustering in Al–Cu–Mg alloys during the early stages of elevated temperature ageing.* Acta Materialia 2010;58:4923–39.

118. Marceau R, Vaucorbeil A de, Sha G, Ringer S and Poole W. *Analysis of strengthening in AA6111 during the early stages of aging: Atom probe tomography and yield stress modelling.* Acta Materialia 2013;61:7285–303.

119. Vaucorbeil A de, Sinclair C and Poole W. *Atomistic insights into cluster strengthening in aluminum alloys.* Materialia 2018;4:566–74.

120. Starink M and Wang S. *The thermodynamics of and strengthening due to co-clusters: General theory and application to the case of Al–Cu–Mg alloys.* Acta Materialia 2009;57:2376–89.

121. Starink M, Cao L and Rometsch P. *A model for the thermodynamics of and strengthening due to co-clusters in Al–Mg–Si-based alloys.* Acta Materialia 2012;60:4194–207.

122. Zhao Q. *Cluster strengthening in aluminium alloys.* Scripta Materialia 2014;84-85:43–6.

123. Zhao Q, Holmedal B, Li Y, Sagvolden E and Løvvik OM. *Multi-component solid solution and cluster hardening of Al–Mn–Si alloys.* Materials Science and Engineering: A 2015;625:153–7.

124. Qin J, Holmedal B and Hopperstad OS. *Experimental characterization and modeling of aluminum alloy AA3103 for complex single and double strain-path changes.* International Journal of Plasticity 2019;112:158–71.

125. Kaufman JG. Introduction to aluminum alloys and tempers. Materials Park, OH: ASM International, 2000.

126. Pettersen T, Li YJ, Furu T and Marthinsen K. *Effect of Changing Homogenization Treatment on the Particle Structure in Mn-Containing Aluminium Alloys.* Materials Science Forum 2007;558-559:301–6.

127. Altenpohl D. Aluminium und Aluminiumlegierungen. Berlin: Springer-Verlag, 1965.

128. Hjelen J. Scanning elektron-mikroskopi. SINTEF, Avdeling for metallurgi Metallisk institutt,NTH, 1986.

Appendix A

Data on the 9 different coils provided by Hydro Aluminium Rolled Products Holmestrand, including composition, mechanical properties, thickness measurements and process parameter of the lacquering process. The samples are ordered after the magnitude of the change in strength, where sample 1 had the highest increases in yield and ultimate tensile strength.

Table A.1: Composition.

Sample nr	Mn	Fe	Si	Cu	Mg	Zn
1	1.13	0.57	0.45	0.17	0.31	0.10
2	1.13	0.57	0.45	0.17	0.31	0.10
3	1.25	0.55	0.45	0.17	0.32	0.09
4	1.11	0.59	0.47	0.17	0.30	0.13
5	1.20	0.61	0.50	0.18	0.29	0.09
6	1.13	0.57	0.45	0.17	0.31	0.10
7	1.14	0.55	0.46	0.16	0.34	0.11
8	1.13	0.57	0.45	0.17	0.31	0.10
9	1.13	0.57	0.45	0.17	0.31	0.10

Table A.2: Mechanical properties tested in the transverse direction.

Sample nr	S_y blank [MPa]	S_y lacquered [MPa]	S_u blank [MPa]	S_u lacquered [MPa]	Total elongation blank [%]	Total elongation lacquered [%]
1	216	231	233	243	6	3
2	214	228	230	239	5	3
3	223	235	238	247	4	2
4	212	223	227	234	6	3
5	219	229	234	240	4	2
6	215	225	232	238	5	3
7	215	222	229	232	6	3
8	220	227	237	238	5	3
9	220	226	236	236	5	2

Table A.3: Metal thickness and lacquer thickness.

Sample nr	Thickness blank [mm]	Thickness lacquered [mm]	Total lacquer thickness [μm]
1	0.298	0.300	28.3
2	0.299	0.299	29.3
3	0.299	0.299	28.3
4	0.301	0.307	31.3
5	0.302	0.307	31.3
6	0.299	0.299	30.3
7	0.298	0.306	28.0
8	0.300	0.310	32.3
9	0.306	0.304	31.3

Table A.4: Process parameters for the ovens, including duration of the heat exposure in each oven and the temperature in oven 1 and oven 2. The duration of the heat exposure is the same in both ovens.

Sample nr	Duration of heat exposure [s]	Temperature oven 1 [°C]	Temperature oven 2 [°C]
1	19	232	253
2	22	227	253
3	22	227	255
4	19	229	258
5	19	230	257
6	22	227	252
7	20	233	267
8	19	229	258
9	19	230	257

Kristine Meling Underhaug

Evolution in Mechanical Behaviour in a Rolled 3xxx Aluminium Alloy during Lacquering

NTNU
Norwegian University of
Science and Technology